ISTANBUL TECHNICAL UNIVERSITY ★ GRADUATE SCHOOL OF SCIENCE ENGINEERING AND TECHNOLOGY

SYNTHESIS, DEVELOPMENT AND CHARACTERIZATION OF W-BASED COMPOUNDS, COMPOSITES AND HYBRID MATERIALS

Ph.D. THESIS

Selim COŞKUN

Department of Advanced Technologies in Engineering

Materials Science and Engineering Programme

DECEMBER 2011

ISTANBUL TECHNICAL UNIVERSITY ★ GRADUATE SCHOOL OF SCIENCE ENGINEERING AND TECHNOLOGY

SYNTHESIS, DEVELOPMENT AND CHARACTERIZATION OF W-BASED COMPOUNDS, COMPOSITES AND HYBRID MATERIALS

Ph.D. THESIS

Selim COŞKUN
(521062009)

Department of Advanced Technologies in Engineering

Materials Science and Engineering Programme

Thesis Advisor: Prof. Dr. M. Lütfi ÖVEÇOĞLU

DECEMBER 2011

İSTANBUL TEKNİK ÜNİVERSİTESİ ★ FEN BİLİMLERİ ENSTİTÜSÜ

VOLFRAM ESASLI BİLEŞİKLERİN, KOMPOZİTLERİN VE DE HİBRİT MALZEMELERİN ÜRETİLMESİ, GELİŞTİRİLMESİ VE KARAKTERİZASYONU

DOKTORA TEZİ

Selim COŞKUN
(521062009)

Mühendislikte İleri Teknolojiler Anabilim Dalı

Malzeme Bilimi ve Mühendisliği Programı

Tez Danışmanı: Prof. Dr. M. Lütfi ÖVEÇOĞLU

ARALIK 2011

Selim Coşkun, **a Ph.D.** student of ITU **Graduate School of Science, Engineering and Technology** student ID **521062009**, successfully defended the **dissertation** entitled "**SYNTHESIS, DEVELOPMENT AND CHARACTERIZATION OF W-BASED COMPOUNDS, COMPOSITES AND HYBRID MATERIALS**", which he prepared after fulfilling the requirements specified in the associated legislations, before the jury whose signatures are below.

Thesis Advisor :	**Prof. Dr. M. Lütfi ÖVEÇOĞLU** İstanbul Technical University	.....
Jury Members :	**Prof. Dr. Süheyla AYDIN** İstanbul Technical University	.....
	Assoc. Prof. Dr. Oğuzhan GÜRLÜ İstanbul Technical University	.....
	Assoc. Prof. Dr. Gökhan ORHAN İstanbul University	.....
	Assoc. Prof. Dr. Deniz UZUNSOY Yıldız Technical Universty	.....

Date of Submission : 04 November 2011
Date of Defense : 26 December 2011

To my beloved wife,

FOREWORD

There are special people associated with this Ph.D. thesis deserving appreciation. Among these, my supervisor Prof. Dr. M. Lütfi Öveçoglu is especially merited for his priceless mentorship, knowledge and support throughout this dissertation work and my whole academic life. I am also thankful to my examining committee members, Prof. Dr. Süheyla Aydın, Assoc. Prof. Dr. Oğuzhan Gürlü, Assoc. Prof. Dr. Gökhan Orhand and Assoc. Prof. Dr. Deniz Uzunsoy for their counseling and motivation.

I would also like to thank all the precious members of the Particulate Materials Laboratories, particularly Assoc. Prof. Dr. Burak Özkal, Hasan Gökçe, Umut Söyler and Aziz Genç for their support and assistance.

I am especially thankful to Dr. Krzystof Koziol from the Macromolecular Materials Laboratory at the University of Cambridge whose support, guidance and knowledge helped me to open up new frontiers for my career and academic life. I am also thankful to all the members of the Macromolecular Materials Laboratory, in particular to Prof. Dr. Alan Windle, Dr. Ahu Gümrah Dumanlı, Mudrika Khandelwal, Matthew James, Nagore Ibarra-Gonzalez, and Fiona Smail for their support and help during my visit to the University of Cambridge.

I would like to thank my colleagues Berk Alkan, Onur Meydanoğlu, Duygu Ağaoğulları, Erçin Ersundu and Önder Güney, whose support made this work and last five years in ITU more bearable and relatively easier.

I would also like to express my thanks to the Scientific and Research Council of Turkey (TÜBİTAK) for their financial support during my graduate education in ITU and during my visit at the University of Cambridge.

I am also thankful to ITU Graduate School of Science, Engineering and Technology who supported this work.

I am especially grateful to my parents Deniz and Vedat for their support and motivation.

Finally, I would like to express my deep appreciation and thanks for my beloved wife DOĞA, who was always there for me with her immeasurable understanding, support and guidance.

January 2012

Selim Coşkun

Metallurgical&Materials
Engineer, M.Sc.

TABLE OF CONTENTS

Page

FOREWORD ..... **ix**
TABLE OF CONTENTS ..... **xi**
ABBREVERATIONS ..... **xiii**
LIST OF TABLES ..... **xv**
LIST OF FIGURES ..... **xvii**
SUMMARY ..... **xxi**
ÖZET ..... **xxv**
1. INTRODUCTION **1**
2. LITERATURE REVIEW **7**
2.1 Tungsten Boride System 7
2.1.1 Tungsten borides 9
2.1.2 Mechanical alloying (MA) 14
2.1.3 Transition metal borides produced by mechanical alloying (MA) 18
2.2 Tungsten Oxide System 21
2.2.1 Tungsten oxides and their nanostructures 21
2.2.2 Carbon nanotubes (CNTs) 27
2.2.3 Tungsten oxide-CNT hybrid systems 32
2.3 W - Mn Matrix Composite System 36
2.3.1 Tungsten, its alloys and composites 36
2.3.2 Production of tungsten, its alloys and composites 43
3. EXPERIMENTAL PROCEDURE **47**
3.1 Tungsten Boride System 47
3.1.1 Production of tungsten borides 47
3.1.2 Characterization studies on tungsten borides 49
3.2 Tungsten Oxide System 50
3.2.1 Production of tungsten oxide nanoparticles 50
3.2.2 Production of tungsten oxide nanorods and nanowires 51
3.2.3 Production of carbon nanotubes 51
3.2.4 Coating of CNTs with tungsten oxide nanoparticles 52
3.2.5 Characterization studies on tungsten oxide nanostructures and CNTs 53
3.3 W - Mn Matrix Composite System 53
3.3.1 Production of W - Mn matrix composites 53
3.3.2 Characterization studies on W - Mn matrix composites 54
4. RESULTS AND DISCUSSION **57**
4.1 Tungsten Boride System 57
4.1.1 Characterization of WB + W_2B powder mixtures 58
4.1.2 Characterization of W_2B_5 powders 64
4.2 Tungsten Oxide System 75
4.2.1 Characterization of tungsten oxide nanoparticles 76
4.2.2 Characterization of tungsten oxide nanostructures after annealing 80

4.2.3 Characterization of CNTs and CNT-tungsten oxide hybrid materials 91
4.2.3.1 Characterization of as-prepared pristine and functionalized CNTs 91
4.2.3.2 Coating of CNTs with tungsten oxide nanoparticles for hybrid synthesis 94
4.3 W - Mn Matrix Composite System 99
4.3.1 Microstructural characterization of powders 99
4.3.2 Microstructural characterization of the sintered samples 103
4.3.3 Physical properties of sintered composites 110
5. CONCLUSIONS AND SUGGESTIONS FOR FUTURE WORK 117
5.1 Conclusions 117
5.2 Suggestions For Future Work 119
REFERENCES 121
CURRICULUM VITAE 137

ABBREVERATIONS

AAS	**:** Atomic Absorption Spectroscopy
BA	**:** Benzyl Alcohol
BCC	**:** Body-Centered Cubic
BEI	**:** Back-Scattered Electron Imaging
BF	**:** Bright-Field
BPR	**:** Ball-to-Powder Ratio
CNT	**:** Carbon Nanotube
CTE	**:** Coefficient of Thermal Expansion
CVD	**:** Chemical Vapor Deposition
DF	**:** Dark-Field
DSC	**:** Differential Scanning Calorimetry
DTA	**:** Differential Thermal Analysis
EDS	**:** Energy-Dispersive X-Ray Spectroscopy
FCC	**:** Face-Centered Cubic
fCNT	**:** Functionalized Carbon Nanotube
FEG-SEM	**:** Field Emission Gun - SEM
HRTEM	**:** High Resolution TEM
LPS	**:** Liquid-Phase Sintering
MA	**:** Mechanical Alloying
MA'd	**:** Mechanically Alloyed
MMC	**:** Metal Matrix Composite
MWNT	**:** Multiwall Nanotube
PCA	**:** Process Control Agent
P/M	**:** Powder Metallurgy
SAED	**:** Selected Area Electron Diffraction
SEI	**:** Secondary Electron Imaging
SEM	**:** Scanning Electron Microscope
SWNT	**:** Single-wall Nanotube
TEM	**:** Transmission Electron Microscope
WHA	**:** Tungsten Heavy Alloy
XRD	**:** X-Ray Diffraction

LIST OF TABLES

Page

Table 2.1 : Crystal structures and lattice parameters of tungsten boride phases... 11
Table 2.2 : Some physical properties of selected tungsten borides ..…….....12
Table 2.3 : Crystallographic data for oxide phases in the W-O system. 23
Table 2.4 : Physical properties of CNTs. 29
Table 2.5 : Properties of different CNT synthesis techniques. 31
Table 2.6 : Inorganic compounds used in CNT hybrid materials, their synthesis techniques and applications. 34
Table 2.7 : Some properties of tungsten. 36
Table 4.1 : Atomic absorption spectroscopy (AAS) analyses of the filtered leaching solutions from the WBM samples MA'd for 15 h, 20 h and 30 h. 61
Table 4.2 : AAS analyses of the filtered leaching solutions from the samples MA'd for 20 h and 30 h. 67
Table 4.3 : Atomic absorption spectroscopy (AAS) analyses of the filtered leaching solutions from the 2W5BM samples MA'd for 30 h after leaching with 5 M HCl and after second leaching of the sample leached with 5 M HCl 73
Table 4.4 : Comparison between W3Mn2VC and W3Mn2ZrC composite samples both MA'd for 6 h and 24 h. 114
Table 4.5 : Friction coefficients of the W3Mn2VC and W3Mn2ZrC samples. 115

LIST OF FIGURES

Page

Figure 2.1 : Hypothetical phase diagram of tungsten-boron system 10
Figure 2.2 : W-B binary phase diagram.....10
Figure 2.3 : Refinement of particle and grain sizes with milling time 17
Figure 2.4 : Schematic view of a ball-powder-ball collision 18
Figure 2.5 : a) W-O Phase diagram and b) detail of W-O Phase diagram.....22
Figure 2.6 : Schematic of a graphene sheet with unit vectors a_1 and a_2 28
Figure 2.7 : Schematic representation of the folding of a graphene sheet into a) zigzag, b) armchair and c) chiral nanotubes.....29
Figure 2.8 : Schematic representation of chemical oxidation 32
Figure 2.9 : Tungsten activation; the position of the activator in the Periodic Table affects the densification of tungsten 44
Figure 3.1 : The schematic of the WO_2 nanoparticle production route and a representative TEM picture showing WO_2 nanoparticles.....50
Figure 3.2 : Schematic of the CNT growth set-up.....52
Figure 4.1 : XRD patterns of; a) as-blended powders and b) powder blend MA'd for 7 h.....58
Figure 4.2 : XRD patterns of loose powders in the WBM sample MA'd for; a) 15 h, b) 20 h and c) 30 h. 59
Figure 4.3 : XRD patterns of the crust formations in the WBM samples MA'd for; a) 15 h, b) 20 h and c) 30 h.....60
Figure 4.4 : XRD patterns of the WBM samples MA'd for; a) 15 h, b) 20 h and c) 30 h after leaching with 3.6 M HCl solution. 61
Figure 4.5 : XRD patterns of the WBM sample MA'd for 20 h; a) before leaching, b) after leaching with 3.6 M HCl and c) after leaching with 5 M HCl..62
Figure 4.6 : XRD patterns of the WBM sample MA'd for 30 h; a) before leaching, b) after leaching with 3.6 M HCl and c) after leaching with 5 M HCl..63
Figure 4.7 : XRD patterns of the WBM samples MA'd for 30 h; a) with 100% of excess B_2O_3, b) 50% of excess B_2O_3, c) 30% of excess B_2O_3 and d) with stoichiometric B_2O_3.....63
Figure 4.8 : XRD patterns of loose powders in the 2W5BM samples MA'd for; a) 30 h and b) 20 h. 65
Figure 4.9 : XRD patterns of crust formations in the 2W5BM samples MA'd for; a) 30 h and b) 20 h. 66
Figure 4.10 : XRD patterns of the 2W5BM samples MA'd for; a) 30 h and b) 20 h, both after leaching with 5 M HCl. 67
Figure 4.11 : XRD patterns of the crust formations in the 2W5BM samples MA'd for 30 h; a) with 100% of excess B_2O_3, b) 50% of excess B_2O_3 and c) with stoichiometric B_2O_3.....68

Figure 4.12 : XRD patterns of the crust formations in the 2W5BM samples MA'd for 30 h; a) with 100% of excess B_2O_3 and b) 50% of excess B_2O_3 after leaching with 5 M HCl. 69
Figure 4.13 : XRD patterns of loose powders in the 2W5BM samples MA'd for 30 h; a) with 100% excess of B_2O_3, b) 50% excess of B_2O_3 and c) with stoichiometric B_2O_3. 70
Figure 4.14 : XRD pattern of the 2W5BM sample MA'd for 30 h with 50% excess of B_2O_3 after leaching with 5 M HCl. 70
Figure 4.15 : DTA curves of; a) the unleached 2W5BM sample, b) the 2W5BM sample leached with 5 M HCl and c) the 2W5BM sample leached with 7 M HCl under Ar atmosphere (100 mL/min) at a heating rate of 10 ^oC/min. 71
Figure 4.16 : XRD patterns of the 2W5BM sample MA'd for 30 h with 50% excess of B_2O_3; a) before leaching and b) after leaching with 5 M HCl, both after DTA analyses. 72
Figure 4.17 : XRD patterns taken from the 2W5BM samples MA'd for 30 h with 50% excess of B_2O_3 after leaching a) with 7 M HCl and b) with 5 M HCl. 73
Figure 4.18 : a) SEM-BEI micrograph of as-blended 2W5BM sample with 50% excess of B_2O_3, b) SEM-SEI micrograph of the 2W5BM sample MA'd for 30 h with 50% excess of B_2O_3 before leaching and c) SEM-SEI micrograph of the pure W_2B_5 sample obtained after leaching with 7 M HCl. 74
Figure 4.19 : Particle size distributions of B_2O_3, $WO_{2.72}$ and MgO in as-blended 2W5BM sample as well as the samples MA'd for 30 h with 50% excess of B_2O_3 before leaching and after leaching with 7 M. 75
Figure 4.20 : XRD pattern of the as-prepared nanoparticles. 76
Figure 4.21 : A BF-TEM micrograph taken from a general area exhibiting as-prepared nanopowders. 77
Figure 4.22 : High-resolution FEG-SEM micrographs of the as-prepared sample... 77
Figure 4.23 : a) and b) BF-TEM micrographs of different powder particles, c) and d) their corresponding DF-TEM micrographs with SAED patterns inset. 78
Figure 4.24 : DSC thermogram of the as-prepared powders scanned under Ar atmosphere (30 mL/min) at a heating rate of 20 ^oC/min. 79
Figure 4.25 : XRD patterns of the as-prepared nanoparticles annealed at 500 ^oC for 2 h. 79
Figure 4.26 : High-resolution FEG-SEM micrograph of as-prepared nanoparticles annealed at 500 ^oC for 2 h. 80
Figure 4.27 : XRD patterns of the as-prepared WO_2 nanoparticles annealed at; a) 800 ^oC, b) 700 ^oC and c) 600 ^oC for 6 h. 81
Figure 4.28 : FEG-SEM micrographs of the WO_2 nanoparticles annealed at 600 ^oC for 6 h. 82
Figure 4.29 : FEG-SEM micrograph of the WO_2 nanoparticles annealed at 700 ^oC for 6 h with higher magnification inset. 82
Figure 4.30 : Representative FEG-SEM micrograph of the WO_2 nanoparticles annealed at 800 ^oC for 6 h with higher magnification inset. 83
Figure 4.31 : FEG-SEM micrograph of the WO_2 nanoparticles annealed at 800 ^oC for 6 h showing the roots of the nanorods in the parent structure. 84

Figure 4.32 : a) BF-TEM micrograph and b) the SAED pattern taken from an individual nanorod 85
Figure 4.33 : HRTEM micrograph of a nanorod. 85
Figure 4.34 : a) BF-TEM micrograph and b) the SAED pattern taken from nanopowders, which were present beside the nanorods.....86
Figure 4.35 : HRTEM micrograph of WO_2 nanopowders. 86
Figure 4.36 : XRD patterns of the samples annealed; a) at 800 ^oC for only 5 min and b) at 700 ^oC for 2 h. 87
Figure 4.37 : FEG-SEM micrographs of the sample annealed at 700 ^oC for 2 h with; a) regular shapes and b) some nanorod formations on or near the island-like structures.....88
Figure 4.38 : SEM micrograph of the sample annealed at 800 ^oC for 5 min with higher magnification inset. 89
Figure 4.39 : FEG-SEM micrograph of the sample annealed at 900 ^oC for 6 h with higher magnifications inset.....89
Figure 4.40 : FEG-SEM micrographs of the sample annealed at 1000 ^oC for 6 h with higher magnifications inset.....90
Figure 4.41 : Low magnification FEG-SEM micrographs of carpet growth pristine CNTs. 91
Figure 4.42 : FEG-SEM micrograph of randomly oriented and entangled CNTs with high magnification SEM micrograph of an individual CNT. 92
Figure 4.43 : BF-TEM micrograph of a pristine MWCNT.....92
Figure 4.44 : FEG-SEM micrograph of functionalized CNTs with higher magnification inset. 93
Figure 4.45 : BF-TEM micrograph of fCNTs. 93
Figure 4.46 : XRD patterns of; a) pristine and b) functionalized CNTs. 94
Figure 4.47 : FEG-SEM micrographs of CNTs without any coating when only water was used. 95
Figure 4.48 : FEG-SEM micrograph a CNT with a continuous coating via fCNT route.....96
Figure 4.49 : BF-TEM micrograph a CNT with a continuous coating via fCNT route with higher magnification inset. 96
Figure 4.50 : FEG-SEM micrograph of a CNT with non-continuous coating via BA route. 97
Figure 4.51 : FEG-SEM micrograph of a CNT with a continuous coating via BA route.....98
Figure 4.52 : BF-TEM micrograph of a CNT with a continuous coating via BA route with higher magnification inset. 98
Figure 4.53 : Typical XRD pattern of a coated CNT.....99
Figure 4.54 : XRD patterns of W1Mn2VC composite powders MA'd for; a) 24 h, b) 12 h, c) 6 h, d) 3 h and e) of W1Mn matrix alloy powders MA'd for 6 h… 100
Figure 4.55 : XRD patterns of W3Mn2VC composite powders MA'd for; a) 24 h, b) 12 h, c) 6 h, d) 3 h and e) of W3Mn matrix alloy powders MA'd for 6 h. 100
Figure 4.56 : Particle size distributions of MA'd powders of; a) 6 h MA'd W1Mn matrix alloy powder with W1Mn2VC composite powders MA'd for 3 h, 6 h, 12 h and 24 h and b) 6 h MA'd W3Mn matrix alloy powder with W3Mn2VC composite powders MA'd for 3 h, 6 h, 12 h and 24 h.....101

Figure 4.57 : Evolution of the grain size of W as a function of the MA time in as-blended W1Mn and W3Mn powders (no milling), in W1Mn and W3Mn matrix alloy powders MA'd for 6 h (MA'd for 6 h in total) as well as in W1Mn2VC and W3Mn2VC powders MA'd for 3 h (MA'd for 9h in total), 6 h (MA'd for 12 h in total), 12 h (MA'd for 18h in total) and 24 h (MA'd for 30h in total). 102
Figure 4.58 : FEG-SEM micrographs of a) as-blended powders, b) W1Mn2VC composite powders MA'd for 24 h and c) W3Mn2VC composite powders MA'd for 24 h. 103
Figure 4.59 : XRD patterns of sintered W1Mn2VC composites MA'd for; a) 24 h, b) 12 h, c) 6 h and d) 3 h. 104
Figure 4.60 : XRD patterns of sintered W3Mn2VC composites MA'd for; a) 24 h, b) 12 h, c) 6 h and d) 3 h. 104
Figure 4.61 : SEM-SEI micrographs taken from sintered W1Mn2VC composite samples MA'd for; a) 3 h, b) 6 h, c) 12 h and d) 24 h. 105
Figure 4.62 : Vickers Microhardness marks on the W1Mn2VC composite sample MA'd for 24 h. 106
Figure 4.63 : SEM-SEI micrographs taken from sintered W3Mn2VC composite samples MA'd for; a) 3 h, b) 6 h, c) 12 h and d) 24 h. 107
Figure 4.64 : SEM-SEI micrographs of fracture surfaces taken from sintered W3Mn2VC composite samples MA'd for; a) 3 h, b) 6 h, c) 12 h and d) 24 h. 108
Figure 4.65 : SEM-BEI micrographs of fracture surfaces taken from sintered W3Mn2VC composite samples MA'd for; a) 3 h, b) 6 h, c) 12 h and d) 24 h. 109
Figure 4.66 : SEM-SEI micrographs of fracture surfaces taken from sintered W3Mn2ZrC composite samples MA'd for; a) 6 h and b) 24 h. 110
Figure 4.67 : Relative density and Vickers microhardness results vs. total MA duration of the sintered W1Mn matrix alloy sample MA'd for 6 h (MA'd for 6 h in total) with the sintered W1Mn2VC composite samples MA'd for 3 h (MA'd for 9 h in total), 6 h (MA'd for 12 h in total), 12 h (MA'd for 18 h in total) and 24 h (MA'd for 30 h in total). 110
Figure 4.68 : Relative density and Vickers microhardness results vs. total MA duration of the sintered W3Mn matrix alloy sample MA'd for 6 h (MA'd for 6 h in total) with the sintered W3Mn2VC composite samples MA'd for 3 h (MA'd for 9 h in total), 6 h (MA'd for 12 h in total), 12 h (MA'd for 18 h in total) and 24 h (MA'd for 30 h in total). 111
Figure 4.69 : Wear amounts of W3Mn2VC and W3Mn2ZrC composite samples. 115

SYNTHESIS, DEVELOPMENT AND CHARACTERIZATION OF SOME W-BASED COMPOUNDS, COMPOSITES AND HYBRID MATERIALS

SUMMARY

Conventional metal alloys, ceramics, and polymeric materials mostly cannot possess the unusual combinations of properties that many of our modern technologies require. Since conventional materials could not fulfill the rising requirements in the last 20 years, an increasing interest in developing new materials, such as high technological ceramics, composites or alloys and the combinations of these new materials has been urged to serve the need for new materials having unique properties for special applications. As a result, non-equilibrium processing of materials has attracted the attention of a number of scientists and engineers due to the possibility of producing better and improved materials than it is possible by conventional methods. Mechanical alloying (MA) is such a processing method holding the greatest advantage of the synthesis of novel alloys and composites by alloying of normally immiscible elements that are not possible by another technique.

Among all refractory metals, tungsten possesses excellent characteristics like good high temperature strength and stiffness, high elastic modulus, good corrosion resistance, high resistance of thermal shock and low coefficient of thermal expansion (CTE). These properties make tungsten an appropriate and interesting matrix material for advanced alloys and composites suitable for numerous applications, especially for which a high-density material is required. Generally, oxides or carbides have been used as reinforcement materials in W-based composites and alloys. In addition to these alloys and composites, tungsten borides and tungsten oxides are two groups of W compounds, which possess interesting mechanical and physical properties among all others. Although data about tungsten borides are very limited in the literature, it is well known that they exhibit promising characteristics like high melting point, high hardness values (>9Mohs), high abrasion and thermal shock resistance, chemical inertness, magnetic properties, metal-like electronic conductivity and good thermal conductivity. These great properties make them ideal for many industrial applications as abrasive, corrosion-resistant and electrode materials, which are exposed to exceptional environmental conditions. However, their production, to date, is difficult due to the need of high temperature equipment. Most importantly, Turkey has a huge share of ~72% of boron and ~2% of tungsten world reserves. Considering that today the commercial prices for 100 g of tungsten borides goes up to ~160€, possession of these huge B and W reserves explicitly actualize the strategic and industrial significance of tungsten boride synthesis. On the other hand, tungsten oxide nanostructures have lately received a lot of attention because of their interesting electrochromic, photochromic and gasochromic properties, which make them potential candidates for optic, electronic, optoelectronic and sensor applications. They have been used in flat panel displays, photo–electro–chromic ‘smart’ windows, storage devices, humidity and temperature sensors, catalysts, optical modulation devices, electron emitters, and gas sensors for NO_2, CO,

CH_4, H_2, NH_3, H_2S and ozone. Nevertheless, synthesis processes for tungsten oxide nanostructures are generally carried out at high temperatures and require technically complex and expensive experimental setup or include several steps and addition of directing agents, which creates other requirements like removal of these agents or other by-products. Lately, tungsten oxides have been used in carbon nanotube (CNT) hybrid materials/composites, which combine the different features of organic and inorganic components in one material. CNTs are ideal constituents for hybrids with their high aspect ratios as well as excellent mechanical, electrical, and optical properties. To produce these hybrids, CNTs are either coated by tungsten oxide or mixed with tungsten oxide nanopowders by various methods. WO_x/CNT hybrids have exhibited their great potential in heterogeneous catalysis and gas sensor applications.

In the light of these, this dissertation work concentrated on three different W-based material systems, their production and characterization. These systems were determined with regard to their uniquity, in the sense of their production method or element combinations used in.

First, tungsten borides (W_xB_y) were produced via mechanical alloying of tungsten oxide ($WO_{2.72}$) and boron oxide (B_2O_3) powders for the first time in the literature. Magnesium (Mg) was used as the reducing agent. In these studies, mixtures of different tungsten boride powders (W_2B, WB and W_2B_5) and, most importantly, pure ditungsten pentaboride (W_2B_5) powders were successfully synthesized and, for characterization, a comprehensive X-ray diffraction study was carried out. In this study, it was appeared that beside the MA duration, the most important issue was to use stoichiometric excess amount of B_2O_3 powders to produce the desired tungsten boride compounds.

Second, tungsten oxide (WO_2) nanoparticles with an average diameter of ~40 nm were produced by a novel water assisted method developed by the present researcher (author) for the first time. Following this, nanorods with an average diameter of 60-70 nm were developed from these nanoparticles via annealing at different temperatures. With increasing temperature, the lengths of these nanorods increased form several hundreds of nanometers up to several tens of micrometers, although the diameters remained unchanged. Another originality of this system was that self-prepared CNTs were used to produce tungsten oxide/CNT hybrid materials/composites.

Finally, a vanadium carbide (VC) reinforced tungsten-manganese (W-Mn) matrix composite system was investigated in this work for the first time. For comparison, zirconium carbide (ZrC) was also used as reinforcement in some samples. W-Mn matrix composites reinforced with 2 wt.% of 24 h pre-milled VC (ZrC) particles were mechanically alloyed (MA'd) for different durations. The effects of the manganese amount and the MA duration on the microstructural and mechanical properties were investigated. Considering that conventional consolidation methods and relatively low sintering temperatures were employed, remarkable Vickers microhardness and relative density values were achieved. When all the wear amounts, the microhardness results, relative densities and microstructures of the composites were taken into account, it was evident that increasing MA and Mn amounts improve the mechanical as well as the microstructural properties of W-Mn matrix composites.

In conclusion, this work revealed the first scientific data on the production of different tungsten borides (W_2B, WB and W_2B_5) and their mixtures via mechanical alloying, tungsten oxide (WO_2) nanostructures with CNT hybrid materials via a water assisted method and W-Mn matrix composites via mechanical alloying and conventional sintering.

VOLFRAM ESASLI BİLEŞİKLERİN, KOMPOZİTLERİN VE DE HİBRİD MALZEMELERİN ÜRETİMİ, GELİŞTİRİLMESİ VE KARAKTERİZASYONU

ÖZET

Geleneksel metal alaşımları ile seramik ve polimer malzemeler günümüz modern teknolojisinin gereksinim duyduğu alışılmamış özellik kombinasyonlarına sahip değildir. Geleneksel malzemelerin bu artan ihtiyaçları karşılayamaması, son 20 senedir ileri teknoloji seramikler, alaşımlar ve de kompozit malzemeler ya da bu malzemelerin çeşitli kombinasyonlarını içeren eşsiz özellikli yeni malzemelerin geliştirilmesine yönelik artan bir ilgi oluşturmuştur. Bunun bir sonucu olarak, denge dışı şartlarda üretilen malzemelerin, geleneksel yöntemlerle üretilen malzemelere göre daha iyi ve gelişmiş özelliklere sahip olabilecek olması, birçok bilim adamı ve mühendisin ilgisini çekmiş ve de hala çekmektedir. Mekanik alaşımlama yöntemi, toz partiküllerinin yüksek enerjili bir öğütücüde tekrarlanan soğuk kaynama, kopma ve yeniden kaynama işlemleri sonucunda ufalanarak homojen bir mikroyapıya sahip kompozit tozların denge dışı şartlarda üretilebilmesini sağlayan bir üretim yöntemidir. Bu yöntemin en önemli avantajı, normal şartlarda birbirleriyle karışamayan elementlerin karışmasını sağlayarak çok çeşitli özelliklere sahip yepyeni alaşımların ve kompozit malzemelerin üretimine imkân sağlamasıdır.

Bütün refrakter metallerin içinde volfram, yüksek ergime sıcaklığı ve elastik modülü, korozyona ve de termal şoka karşı dayanımı, düşük termal genleşme katsayısı ve yüksek sıcaklıklarda gösterdiği mukavemet ve de direngenlikten dolayı, özellikle yüksek yoğunluk gerektiren sayısız uygulamada kullanılan birçok gelişmiş alaşım ve de kompozit malzeme için uygun bir matris malzemesi olarak öne çıkmakta ve de tercih edilmektedir. Bu tarz alaşım ve kompozitlerde takviye malzemesi olarak genellikle çeşitli oksitler, karbürler ve de nitrürler tercih edilmektedir. En çok tercih edilen takviye elemanları TiC, ZrC, HfC, TiN, Y_2O_3, La_2O_3, Sm_2O_3, ThO_2 ve ZrO_2 olarak sıralanabilir. Bütün bu kompozit ve alaşımlara ek olarak, volfram borür ve de volfram oksitler oldukça enteresan mekanik ve fiziksel özelliklere sahip olan iki tip volfram bileşiği olarak ön plana çıkmaktadırlar. Volfram borürler hakkındaki literatür bilgisi çok sınırlı olmakla birlikte, bu bileşiklerin yüksek ergime sıcaklığı, yüksek sertlik (>9 Mohs), yüksek aşınma ve termal şok direnci, kimyasal kararlılık, manyetiklik, metal benzeri elektrik iletkenliği ve de iyi ısı iletkenliği gibi etkileyici özelliklere sahip oldukları bilinmektedir. Bütün bu özellikler volfram borürleri, sıra dışı şartlarda hizmet gören aşındırıcı, korozyona dayanıklı ve de elektrot malzemelerinin gereksinim duyulduğu endüstriyel uygulamalar için ideal bir hale getirmektedir. Ancak günümüze kadarki süreçte, bu bileşiklerin üretimlerinde yüksek sıcaklık ekipmanlarına gereksinim duyulması birçok zorluğu da beraberinde getirmiştir. Bununla birlikte en önemlisi, Türkiye'nin bor ve volfram madenlerince çok zengin olduğu gerçeğidir. Özellikle dünya bor rezervlerinin yaklaşık %72'lik dev bir bölümü ile volfram rezervlerinin %2'lik bir kısmı ülkemizde bulunmaktadır.

Günümüzde ticari olarak satılan volfram borür tozlarının 100 gramının fiyatının yaklaşık olarak 160€ 'ya kadar çıktığı düşünüldüğünde, böylesine zengin bor ve volfram rezervlerine sahip olmanın, volfram borür bileşiklerinin üretimini endüstriyel olarak ne kadar stratejik ve de önemli bir hale getirdiği gerçeği bir kez daha tüm açıklığıyla ortaya çıkmaktadır. Diğer bir taraftan, son zamanlarda volfram oksit nanoyapılar da sahip oldukları enteresan elektrokromik, fotokromik ve gazokromik özellikler sayesinde ilgi çekmektedirler. Bu özellikler, volfram oksit nanoyapıları özellikle optik, elektronik, optoelektronik ve sensör uygulamaları için potansiyel birer aday haline getirmektedir. Günümüzde ise bu malzemeler, flat ekran görüntüleme sistemlerinde, foto-elektro-kromik akıllı pencerelerde, hafıza depolama cihazlarında, nem ve sıcaklık sensörlerinde, katalizörlerde, optik modülatörlerde, elektron yayınımında ve NO_2, CO, CH_4, H_2, NH_3, H_2S ve ozon gazları için kullanılan gaz sensörlerinde sıkça kullanılmaktadırlar. Fakat volfram oksit nanoyapıların üretimi genellikle ya yüksek sıcaklık ile teknolojik olarak karmaşık ve de pahalı ekipmanlar gerektirmekte ya da birbirinden farklı kademeler ve çeşitli katkı maddelerinin kullanımını içermektedir ki, bu da oluşacak yan ürünlerin ya da kullanılan bu katkı maddelerinin uzaklaştırılması için fazladan işlem yapmayı mecbur kılmaktadır. Son zamanlarda, volfram oksit malzemeler karbon nanotüpler (KNTler) ile birlikte çeşitli hibrit malzemeleri/kompozitleri oluşturmak için kullanılmaktadırlar. Hibrit malzemelerin en önemli avantajı çeşitli organik ve de organik olmayan bileşenlerin farklı özelliklerini bir malzemede birleştirebilmeleridir. Hibrit malzemelerin geleneksel kompozit malzemelerden farkları ise, malzeme bileşenlerinin nanometre ve hatta moleküller düzeyde birbirleriyle karışmasıdır. KNTler sahip oldukları yüksek en-boy oranları ve de muazzam mekanik, elektronik ve de optik özellikleri sayesinde bu tarzda hibrit malzemeler için eşsiz birer bileşen haline gelmişlerdir. Bu hibritlerin üretimi için, KNTler çeşitli yöntemlerle ya volfram oksit ile kaplanmakta ya da volfram oksit nanotozları ile karıştırılmaktadırlar. Volfram oksit/KNT hibritleri, sahip oldukları büyük potansiyeli heterojen katalizör ve gaz sensörü uygulamalarında başarıyla sergilemektedirler.

Bütün bilgilerin bu ışığında, bu doktora çalışması üç farklı volfram esaslı malzeme sistemi üzerine odaklanmıştır. Bu sistemler gerek üretim yöntemleri gerekse kullanılan element kombinasyonlarının özgünlüğüne göre seçilmiştir.

İlk olarak farklı volfram borürler (W_xB_y), volfram oksit ($WO_{2.72}$), bor oksit (B_2O_3) ve de redükleyici eleman olarak magnezyum (Mg) tozlarının kullanılması ile literatürde ilk defa mekanik alaşımlama yöntemiyle üretilmiştir. Bu çalışmalarda, farklı volfram borürlerin karışımları (W_2B, WB ve W_2B_5) ve de en önemlisi saf halde volfram pentaborür (W_2B_5) tozları başarıyla üretilmiş ve de karakterizasyonları için kapsamlı bir X-ışınları çalışması gerçekleştirilmiştir. Bu çalışmada istenen volfram borür bileşiklerinin üretilmesinde, mekanik alaşımlama süresiyle birlikte en önemli noktanın stokiyometrik olarak hesaplanandan daha fazla B_2O_3 tozu kullanmak olduğu görülmüştür.

İkinci olarak, ortalama ~40 nm çaplı volfram oksit (WO_2) nanotozları ilk defa araştırmacı tarafından geliştirilmiş yeni bir sulu çözelti yöntemiyle üretilmiştir. Bunu takiben, üretilmiş olan nanotozlar farklı sıcaklıklarda tavlanarak ortalama 60-70 nm çaplı nanoçubuklar geliştirilmiştir. Artan tavlama sıcaklığı ile bu çubukların çapları değişmezken, boylarının birkaç yüz nanometreden birkaç on mikrometreye kadar uzadıkları gözlemlenmiştir. Bunların yanında sistemin bir diğer orijinalliği de yine bu çalışmada üretilen KNTler kullanılarak çeşitli volfram oksit/KNT hibrit

malzemelerin üretilmiş olmasıdır. Bu hibritlerin üretimi için hem saf hem de fonksiyonlaştırılmış KNTler nano boyuttaki volfram oksit partikülleriyle kaplanmıştır. Saf KNTler kullanıldığında oksit partikülleriyle KNTler arasındaki etkileşimin daha zayıf olduğu gözlemlenmiştir.

Son olarak, vanadyum karbür (VC) takviyeli volfram-mangan (W-Mn) matrisli kompozit sistemi yine bu çalışmada ilk defa incelenmiştir. Karşılaştırma yapabilmek için bazı numunelerde VC yerine zirkonyum karbür de (ZrC) kullanılmıştır. Önceden 24 saat öğütülmüş olan ağırlıkça %2 oranında VC (ZrC), W-Mn matrise katılarak farklı sürelerde mekanik alaşımlanmıştır. Bunun sonucunda, mekanik alaşımlama süresi ve de Mn miktarının üretilen kompozitin mikroyapı ve mekanik özelliklerine yaptığı etkiler incelenmiştir. Bu çalışmada geleneksel pekiştirme ve göreceli olarak düşük sinterleme sıcaklıkları kullanılmış olduğu düşünüldüğünde, elde edilmiş olan göreceli yoğunluk ve de Vickers mikrosertlik sonuçları oldukça ilgi çekicidir. Elde edilen bütün aşınma, sertlik, yoğunluk sonuçları ile kompozitlerin mikroyapıları irdelendiğinde, artan Mn miktarı ile mekanik alaşımlama süresinin kompozitlerin mikroyapısal ve fiziksel özelliklerini önemli ölçüde iyileştirdiği görülmüştür.

Sonuç olarak, bu çalışma farklı volfram borür tozlarının mekanik alaşımlamayla, WO_2 nanoyapıların ve KNT hibrit malzemelerinin yeni geliştirilmiş bir sulu çözelti yöntemiyle ve de W-Mn matrisli kompozitlerin mekanik alaşımlama ve de geleneksel sinterleme yöntemleriyle üretilmeleri konularında ilk bilimsel verileri sergilemektedir.

1. INTRODUCTION

It is certainly apparent that the development of the materials and the improvements in the materials technology have always been the keys for the important technology breakthroughs throughout the history of humankind. Today's aerospace era is a new revolution, which has also been initiated by the outbreak of the advanced materials (Schwartz, 1997).

Conventional metal alloys, ceramics, and polymeric materials mostly cannot possess the unusual combinations of properties that many of our modern technologies require. Since conventional materials could not fulfill these rising requirements in the last 20 years, an increasing interest in developing new materials, such as high technological ceramics or composites and the combinations of these new materials has been urged to serve the need for new materials having unique properties for special applications (Song et al, 2003a; Tang et al, 2004). Therefore, in parallel with the development of advanced materials, such material combinations, which fulfill the needs of the modern technology have been, and are yet being, extended. High-technology industries have given an added stimulus to these efforts (Suryanarayana, 2001). As a result, non-equilibrium processing of materials has attracted the attention of a number of scientists and engineers due to the possibility of producing better and improved materials than it is possible by conventional methods (Suryanarayana et al, 2001). Mechanical alloying (MA) is such a processing method by which advanced materials can be fabricated under non-equilibrium conditions (Suryanarayana, 2001) holding the greatest advantage of the synthesis of novel alloys and composites by alloying of normally immiscible elements that are not possible by another technique (Suryanarayana et al, 2001).

With increasing demand for improved efficiency of engines, plants and production processes, ceramics have gained great importance as structural engineering materials in recent years (Zerr and Riedel, 2000; Barsoum, 2003). Within the group of the so-called advanced materials, carbon in form of diamond or diamond-like structures, carbides, nitrides and borides have reached an outstanding position due to their

excellent hardness and thermo-chemical as well as thermo-mechanical properties. The distinct covalent bonding of the aforementioned structures positively influences their hardness and their tribological behavior (Zerr and Riedel, 2000). Most people associate the word ceramics with pottery, sculpture, sanitary ware, tiles, etc. and whereas this view is not incorrect, it is incomplete because it considers only the traditional, or silicate-based, ceramics. Today the field of ceramic science or engineering encompasses much more than silicates and can be divided into traditional and modern ceramics (Barsoum, 2003). There is presently much effort in basic science and applied research to work on novel ceramic hard materials denoted as super- or ultra-hard materials that can compete with the hardness of conventional diamond. Aim and scope of the research in this field is to develop hard materials with superior mechanical and chemical properties and with similar hardness (Zerr and Riedel, 2000).

Composite materials, which are materials produced by combining two or more dissimilar materials into a new material exhibiting a significant proportion of the properties of constituent phases (Schwartz, 1984), are especially attractive for applications in marine, automotive, aviation and aerospace industries because they possess exceptional strength and stiffness-to-density ratios as well as superior physical properties. As a result, using composite materials in these industries has led to improvements in the technology (Coşkun et al, 2004). Furthermore, this great potential has raised the demand for a comprehensive study of the mechanical properties of these materials (Quinta da Fonseca et al, 2001). Among these, metal matrix composites (MMC) combine a metallic base and a reinforcing constituent, which is usually non-metallic and is commonly a ceramic, into a single material. It is also possible to use other materials as reinforcements instead of ceramics, for instance refractory metals or intermetallics (Clyne, 2001). Generally, the main reason to add ceramic particles into a metal base is to increase the hardness and wear resistance of the metal (Miserez et al, 2004). Moreover, MMCs combine metallic properties such as ductility and toughness with the high strength and modulus of ceramics (Tjong and Ma, 2000). The mechanical properties of the MMCs highly depend on the volume fraction and the type of the reinforcement as well as the type of the matrix (Stjernstoft, 2004). On the other hand, while continuous fibre-reinforcement provides the most effective strengthening in a given direction, particle-

reinforcement provides isotropic properties as well as cost-effectiveness to the composite. In addition, the latter one can be processed using similar technology used for monolithic materials (Chawla and Shen, 2001.). Furthermore, MMCs with discontinuous reinforcements are also attractive for their processability into various shapes (Chung, 2001).

As a sub-category of composite materials, hybrid materials/composites are made up of a combination of both organic and inorganic materials (Kickelbick, 2007; Chujo, 2007). However, in order to distinguish them from the conventionally known composites that are mere mixtures, it is necessary to call the materials "hybrid materials" when the level of mixing of the different types of materials is at the nanometer level, or sometimes at the molecular level (Chujo, 2007). The most obvious advantage of hybrids is that they can favorably combine the often-dissimilar properties of organic and inorganic components in one material. Many possible combinations of components provide the opportunity to invent an almost unlimited set of new materials with a large spectrum of known and maybe unknown properties (Kickelbick, 2007).

As interesting and appropriate matrix materials with their high melting point, high modulus, high resistance of thermal shock, low CTE and good high temperature strength and stiffness, in this last decade, tungsten (W) and its alloys have received attention with a view of improving the high temperature mechanical properties (Song et al, 2002a). A large number of tungsten alloys and composites were investigated in the past. However, only some of them achieved technical importance. Tungsten and tungsten alloys dominate the market in applications for which a high-density material (19.3 g/cm^3) is required, such as kinetic energy penetrators, counterweights, flywheels, anti-vibration holders and armor pierces (Öveçoğlu et al, 1996; Lassner and Schubert, 1999). Other applications include radiation shields and x-ray targets (anonymous, 2011c). In wire form, tungsten is used extensively for lighting, electronic devices, and thermocouples (anonymous, 2011a; Lassner and Schubert, 1999). Currently uses of tungsten are mainly used as tungsten carbide (WC) in cemented carbides, such as WC-Co and WC-Co-TiC (anonymous, 2011b; Acchar et al, 2004; Zhang et al, 2003), and as metallic W in alloys, such as Stellites (Co-Cr-W) (anonymous, 2011c), WHAs (Ryu and Hong, 2003; Lassner and Schubert, 1999), tantalum-tungsten, niobium-tungsten (anonymous, 2011c) and rhenium-tungsten

(Park, 1993) alloys for their special properties, like creep resistance, wear resistance and high temperature strength. Beside these alloys, there are tungsten dispersion-strengthened and precipitation hardened composites. Generally, oxides or carbides have been used as reinforcement materials in W matrix (Chen et al, 2000; Mabuchi et al, 1997; Ryu and Hong, 2003; Song et al, 2002a; Song et al, 2003a; Song et al, 2003b). In addition to these alloys and composites, there are also several W compounds with metallic elements (intermetallic compounds) as well as with non-metallic elements (Lassner and Schubert, 1999). Among these compounds, tungsten borides and tungsten oxides are two groups of W compounds, which possess interesting mechanical and physical properties. Actually, one can hardly find any study on producing of tungsten borides, whereas they exhibit promising characteristics like high melting point, high hardness values (>9Mohs), high abrasion and thermal shock resistance, chemical inertness, magnetic properties, metal-like electronic conductivity and good thermal conductivity. (Cai and Nan, 2000; Gorbunov and Bryksin-Lyamin, 1971; Itoh et al, 1987; Lassner and Schubert,1999; Lv et al, 2006; Khor et al, 2005, Kushkhov et al, 1993; Stadler et al, 2000; Usta et al, 2005; Wen et al, 2006b). On the other hand, tungsten oxides have lately received a lot of attention because of their interesting electrochromic, photochromic and gasochromic properties, which make them potential candidates for optic, electronic, optoelectronic and sensor applications (Shah, 2009; Lillard et al, 1998; Mwakikunga et al, 2008; Ma et al, 2006; Boulova et al, 2001; Liu et al, 2005; He and Zhao, 2008).

All things considered, this dissertation work will concentrate on three different W-based material systems, their production and characterization. The common ground of these systems will be their uniquity, in the sense of their production method or element combinations used in. Firstly, tungsten borides, their importance and possible applications will be discussed. The underlying reason of the uniquity of this system will be that this work will reveal first scientific data about the production of pure tungsten borides via mechanical alloying route. Second system will be the tungsten oxide system where tungsten oxide nanoparticles will be produced by a novel water assisted method developed by the present researcher (author) for the first time. Following this, different nanostructures will be developed from these nanoparticles. Another originality of this system will be that self-prepared carbon nanotubes (CNTs) will be used to produce some WO_x/CNT hybrid

materials/composites. Finally, a composite system based on a tungsten-manganese (Mn) matrix will be investigated in this work for the first time, in which vanadium carbide (VC) will be the primary reinforcement agent. Besides, zirconium carbide (ZrC) will be also used for comparison.

In the light of these, this work will emerge as a result of a comprehensive research and will make a good contribution to material science world, where it reveals interesting examples of some tungsten-based compounds, composites and hybrid materials.

2. LITERATURE REVIEW

This chapter will focus on the background, importance, production and applications of the aforementioned W-based material systems. The first section of the chapter is about the tungsten boride system. Some properties and applications of boron compounds and transition metal borides will be introduced, followed by the discussion about the tungsten borides and similar researches. Furthermore, mechanical alloying method, which has been chosen as the production route for the tungsten borides for the first time in the literature, will be mentioned in detail. Additionally, transition metal borides produced via mechanical alloying will be discussed. In the second section, detailed information about tungsten oxides, carbon nanotubes and tungsten oxide-carbon nanotube hybrids will be given, moreover, their properties and applications will be discussed. Finally, the third section will reveal detailed information about tungsten, its alloys and composites.

2.1 Tungsten Boride System

Materials based on boron compounds have been observed for many decades because of their exceptional properties relating to chemical bonding, crystal structure, and phonon and electron conduction (Telle et al, 2000). Especially in the field of energy conversion, electron emission, and neutron absorption, borides occupy many niches of application for which no other material can be employed (Telle et al, 2000; Kushkhov et al, 1993). They are an important class of inorganic compounds with a set of valuable properties, such as high melting point and high hardness (Kushkhov et al, 1993). Although some of the interesting thermal and mechanical properties of borides, which led to applications such as wear-resistant parts or grinding grits, have already been benefited a long time ago, the fundamental understanding of technical ceramics resulted the dramatic increase of the interest in borides. Using of materials with exceptional mechanical, chemical, electrical and thermal properties yielded boron compounds as potential candidates for “high-tech” applications alternative to

the well-developed oxide ceramics, silicon nitride, silicon carbide, and hard metals or cermets (Telle et al, 2000; Kushkhov et al, 1993).

In addition to their relatively high costs, a lack of understanding is the main reason why boride-based materials have not yet been used widespread as the other ceramics materials, although some properties such as extreme hardness make them superior to oxides and nitrides. Thus, some "eras" of the research on borides can be determined; first one was around 1960 supported by the needs of the nuclear energy and weapon industry, while another was between 1970 and 1980 for thermo-electric power generation and coming up again today. Following these, the next was driven by the need for exceptional wear properties between 1980 and 1990, and finally between 1985 and 1992, which was triggered by aerospace and military research (Telle et al, 2000).

> The interest in borides rising from a political and strategic point of view has contributed to the fact that information about borides is still difficult to obtain and even more difficult to interpret since most of the data have been restricted for a long time and their sources and quality cannot be ascertained in all cases. (Telle et al, 2000, p.803)

In specific terms, transition metal borides have various useful physical and chemical characteristics, which make them important materials to study (Usta et al, 2005). Noticeable characteristics include heat resistance, great hardness, wear resistance, and high temperature electrical resistance (Usta et al, 2005; Khor et al, 2005; Stadler et al, 2000). They are an important class of advanced structural ceramic materials and are candidate materials for various applications, i.e. armor materials, aluminum evaporation boat, cathode material for hall-heroult cell, cutting tool, electro discharge machining (EDM) electrode, wear parts, high temperature applications, electrical devices, in rockets nozzles and in foundry or refractory applications (Venkateswaran et al, 2006). Furthermore, cermets based on borides are of interest for applications that require a material of extreme heat and corrosion resistance, such as materials in contact with reactive hot gases or molten metals, because metal borides generally are more refractory than titanium carbide (Ellis and Goetzel, 1990). The diborides of the transition metals hafnium, tantalum, zirconium, and titanium have extremely high melting points, descending in the order given from 3250 to 2800 °C. Molybdenum boride (MoB) and chromium boride (CrB) melt at considerably lower temperatures (2180 and 1550 °C, respectively). The oxidation resistance of the transition metal

diborides above a temperature of 1100 °C is considerably better than that of TiC and roughly follows the descending order of the melting point. Because these metal borides have relatively high thermal conductivity and high-temperature stability, they do not depend on a supportive metallic binder matrix for thermal shock resistance and strength as do the Ni-Cr alloys in TiC cermets (Ellis and Goetzel, 1990; Telle at al, 2000). The boride phases alone in their highly purified state are extremely hard and abrasive; however, their consolidated bodies pose problems in fabrication to useful products, as well as in service, especially in environments involving dynamic gas or liquid metal flow (Ellis and Goetzel, 1990). This shortcoming can be alleviated in some instances by a metallic binder phase. For thermodynamic reasons, this binder phase generally is limited to 2-5 at.% up to a maximum of 10 at.%. The principal candidate metals for cementing the boride grains are iron, nickel, cobalt, chromium, molybdenum, tungsten, and boron, or some of the alloys of these metals (Ellis and Goetzel, 1990; Telle et al, 2000). Low-melting eutectics in the systems boron-iron (1161 °C), boron-cobalt (1102 °C), and especially boron-nickel (990 °C) restrict the amount of the respective binder metals to a small percentage. Additions of up to 5 wt.% B and 10 wt.% Mo or W can be successfully used as a binder (of ZrB_2, for example) without forming low-melting phases (Ellis and Goetzel, 1990).

2.1.1 Tungsten borides

Recent comprehensive study on the W-B binary system was conducted by Nagender and Rama (1991). Currently, various kinds of borides such as W_2B, WB, WB_2, W_2B_5, WB_4 and WB_{12} are known to exist in the W-B system (Peshev et al, 1967; Itoh et al, 1987; Lassner and Schubert, 1999). The WB phase possesses two polymorphs, such as high-temperature (β-WB) and low-temperature (α-WB) (Portnoi et al, 1966). The crystalline structures of the W_2B, α-WB, and W_2B_5 phases were determined by Kiessling (1947), when he conducted the first systematic investigations at temperatures below 1250 ^{o}C using X-ray analysis methods and the structure of the high-temperature polymorph of the tungsten monoboride β-WB was established by Post and Glaser (1952). Furthermore, the boride phases WB_2 and WB_4 were first reported by Chretien and Helgorsky (1961). Portnoi et al (1966) discussed the existence of WB_{12} while Rudy et al (1963) detected the phase and determined its lattice parameters. Moreover, Kuz'ma (1967) reported a low temperature polymorph

of the W_2B_5 phase. Following thorough elaborations on the thermodynamics and crystal structures of tungsten borides, Kieffer and Benesovsky reviewed a hypothetical phase diagram of tungsten-boron system (Portnoi et al, 1966) shown in Figure 2.1.

Rudy published a phase diagram in 1969 and this diagram was modified by Moffatt in 1983 and by Massalski in 1986, which has become today's modern W-B binary phase diagram (Predel, 1992) shown in Figure 2.2.

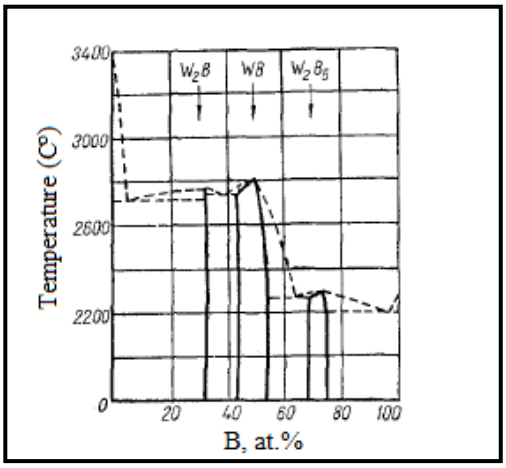

Figure 2.1 : Hypothetical phase diagram of tungsten-boron system, adapted from Portnoi et al (1966).

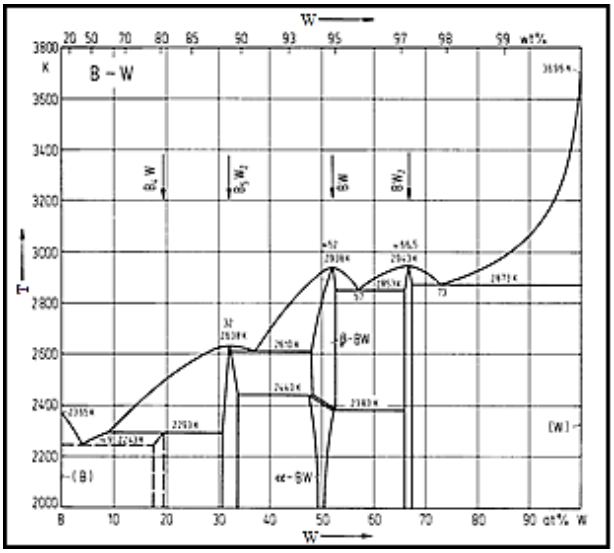

Figure 2.2 : W-B binary phase diagram, adapted from Predel (1992).

Dushanek and Rogl (1995) published a comprehensive study about the thermodynamic calculations of the boron-tungsten binary system and revealed very detailed data on the crystallographic structures, lattice parameters and thermodynamic parameters of tungsten borides. In this study, they (Dushanek and

Rogl, 1995) have exhibited a review about crystallographic and thermodynamic properties of almost all existing tungsten boride phases by comparing archival literature to their experimental and theoretical results. Table 2.1 shows detailed information about the crystal structures and the lattice parameters of the aforementioned tungsten boride phases.

Table 2.1 : Crystal structures and lattice parameters of tungsten boride phases, adapted from Predel (1992).

Phase	Structure	Type	a (nm)	b (nm)	c (nm)
B_4W	tetragonal		0.6340		0.4500
B_5W_2	hexagonal[1]	Mo_2B_5	0.3011		2.0930
	hexagonal	Mo_2B_6[3]	0.2984[4]		1.3870[4]
	defect structure[2]		0.2984[5]		1.3890[5]
α-BW[6]	tetragonal	MoB	0.3115		1.6930
β-BW[7]	orthorhombic	CrB	0.3190	0.8400	0.3070
BW_2	tetragonal	$CuAL_2$	0.5566[4]		0.4748[4]
			0.5564[5]		0.4845[5]
Further mentioned phases					
$B_{12}W$	hexagonal		0.3004		0.3174
B_9W_2	hexagonal	B_9W_2	0.5206		0.6345
B_4W	hexagonal	B_4W	0.5200		0.6340
B_2W	hexagonal	AlB_2	0.3020		0.3050
	hexagonal	B_2W	0.2983		13.879

[1] Below 1700 K
[2] Above 1700 K
[3] Closely related to Mo2B6
[4] At the W-rich boundary of the homogeneity range
[5] At the B-rich boundary of the homogeneity range
[6] Below 2120 K
[7] Above 2120 K

Tungsten borides have promising characteristics like high melting point, high hardness values (>9 Mohs), high abrasion resistance, chemical inertness, magnetic properties and metal-like electronic conductivity (Lassner and Schubert, 1999). These characteristics have made tungsten borides interesting candidates for industrial applications as abrasive, corrosion-resistant and electrode materials, which are exposed to exceptional environmental conditions (Lassner and Schubert, 1999; Khor et al, 2005, Cai and Nan, 2000; Kushkhov et al, 1993; Itoh et al, 1987; Lv et al, 2006; Wen et al, 2006b; Gorbunov and Bryksin-Lyamin, 1971). Researchers are specifically interested in problems related to tungsten borides, because their production is difficult due to the use of high-temperature equipment and, in some

degree, does not meet the practical needs simultaneously (Gostishchev et al, 2009). Tungsten borides are resistant to thermal shock and are good thermal conductor (Usta et al, 2005). They are used in temperature applications such as crucibles and ingot molds for precision metallurgy (Usta et al, 2005; Stadler et al, 2000). Moreover, tungsten boride powders are used for developing various composite materials, including metal–boride alloys for fillers (borolites) (Gostishchev et al, 2009). W_2B_5 phase has lately been used to improve the thermoelectric properties of B_4C ceramics (Cai and Nan, 2000), to improve the electrical conductivity, wear and oxidation resistance, flexural strength and fracture toughness of carbon composites (Wen et al, 2006a; Wen et al 2006b; Lv et al, 2006). Recently, Lv et al in 2007 have used W_2B_5 to increase the wear resistance of carbon composites against steel bearings. Moreover, WB has been used in WC-WB-Co-Cr and WC-WB-Co mixtures as feedstocks of High Velocity Oxygen Fuel (HVOF) Thermal Spray Process to enhance the abrasion and corrosion resistance of the metal surfaces contacting molten metal (Yazıcı, 2009). Lately, Kayhan et al (2011) reported a superconducting transition temperature above 4 K for WB_2 although it was reported (Hardy and Hulm, 1954) that no superconductivity was present in the W-B system except for W_2B. Table 2.2 lists some physical properties of selected tungsten borides.

Table 2.2 : Some physical properties of selected tungsten borides, adapted from Lassner and Schubert (1999) and Schackelford and Alexander (2001).

Properties	**W_2B**	**WB**		**W_2B_5**
		a	**b**	
Melting Point (^oC)	2780	-	2920	2980
The Regions of Homogeneity (%B)	Limited	49-51.5	48-52	68-69.3
Enthalpy of Formation -ΔH ^{o}298 (kJ/mol)	65.3	63	54.5	192.5
Density (g/cm^3)	17.05	16	16	13.1
Microhardness (kg/mm^3)	2350	-	2600	2700
Electrical Resistivity (μΩ·cm)	-	-	25	19
Modulus of Elasticity (GPa)	-	-	608	755

Tungsten borides have been synthesized by solid-state reaction from elements, reduction of oxides by carbon, borothermal reduction of metal oxide, molten salt electrolysis and chemical vapor deposition (Itoh et al, 1987; Lassner and Schubert, 1999; Gostishchev et al, 2009). Fusion processes, such as metallothermy and self-

propagating high-temperature synthesis are also used for production of borides by reduction of metals (including tungsten and boron) oxides with aluminum, magnesium, or calcium (Gostishchev et al, 2009).

Peshev et al (1967) investigated the formation of W_2B_5 via the reaction of WO_2 with elemental B under vacuum conditions. According to this borothermic reaction, the ideal temperature for the formation of W_2B_5 was found to be as 1600 ^oC. Below this temperature, the formation of W_2B was observed, while WB was formed along W_2B_5 at higher temperatures (Peshev et al, 1967). Similarly, Karasev (1972) prepared W_2B_5 by the boron carbide method using elemental W, boron carbide (B_4C) and boric anhydride (B_2O_3). He produced commercially pure W_2B_5 under both H_2 and converted gas atmospheres (Karasev, 1972). Another study on the production of WB powders via solid-state reaction was carried out by Matsudaira et al (1987), who synthesized WB as a result of a reaction of tungsten and amorphous B. In this study, WB was obtained as a single crystalline phase, where its crystallinity and amount increased with increasing heat treatment duration and temperature (Matsudaira et al, 1987). On the other hand, Bodrova et al (1974) produced WB_4 via the solid-state reaction of elemental crystalline W and B. They sintered the produced WB_4 powders for 2 h under argon (Ar) at 1900 ^oC and measured microhardness values of ~4000 kg/mm^2 for these sintered counterparts (Bodrova et al, 1974). Similarly, Itoh et al (1987) synthesized various kinds of tungsten borides by solid-state reaction between tungsten and amorphous boron powders. The mixed powders with various compositions (B/W = 0.4 to 13.0) were treated at 800 to 1550 °C for 0 to 120 min in a stream of Ar. They produced four kinds of boride phases such as W_2B, WB, W_2B_5 and WB_4. The maximum formation amount and crystallinity of WB and W_2B_5 were achieved when nearly 10 at.% excess amount of boron was used (Itoh et al, 1987). Nikolenko and Gostischev (1997) produced W_2B_5-Al_2O_3 composites via aluminathermic process using sheelite ($CaWO_4$) and B_2O_3/B_4C as precursors. Results that are more satisfying were achieved when B_4C was used as the B source (Nikolenko and Gostischev, 1997). Another method to produce tungsten borides is the electrochemical method. Kushkov et al (1993) worked on the electrochemical synthesis of tungsten borides in a dispersed condition. Conditions for preparing different boride phases were determined. If the anode material is graphite and the voltage in the bath is below 2.5 V the cathode deposits consists mainly of tungsten

metal, while a mixture of phases (W, W_2B, WB, WB_2, W_2B_5) is produced on the cathode with U = 2.5-3.5 V and the higher boride WB_4 with U = 3.5-4.5 V. Overall, different parameters like electrolytic bath composition, voltage in the bath, temperature and duration of electrolysis were investigated (Kushkov et al, 1993). Similar studies on the high temperature electrochemical synthesis of tungsten borides from ionic melts were carried out by different researchers (Hab, 2007; Malyshev et al, 2002; Malyshev, 2002; Gostishchev et al, 2009). In addition to these, tungsten borides can also be produced on the surface of pure W by the boronizing of W metal (Usta et al 2005; Khor et al, 2005). Finally, there is only one attempt about preparing of some tungsten borides via mechanical alloying (Stubicar at al, 1995), which will be discussed in the section "2.1.3. Transition metal borides produced by mechanical alloying (MA)".

Beside all these facts that tungsten borides possess great properties for many industrial applications and their production is difficult due to the need of high-temperature equipment, it is very important to mention about the strategic significance of these materials for our country, Turkey. In terms of total reserve basis, Turkey has a huge share of 72.2%, the other important country is USA with a share amount of only 6.8% and with this share of 72.2%, Turkey has a total boron reserve of 851 million tons on the basis of B_2O_3 content (anonymous, 2011d; DPT, 2001a). Moreover, Turkey has 2% of the total world tungsten reserve, which is equal to an amount of app. 65,000 tons (DPT, 2001b). Considering that today the commercial prices for tungsten borides are 85.5 € for 100 g of WB+W_2B powder mixtures, 110 € for 99% pure WB powders and 162 € for 99.4% pure W_2B_5 powders (anonymous, 2011e), possession of these huge B and W reserves explicitly actualize the strategic and industrial significance of tungsten boride synthesis.

2.1.2 Mechanical alloying (MA)

The transition metal borides are produced as pure crystals by such processes as the solid-state reaction of metal boron, the reaction of the metal or its oxide with boron carbide, the reduction of boron and metal oxides with carbon or reactive metals, or fused-salt electrolysis. Mixtures of these borides and binder metal powder are processed into cermet products by ceramic or P/M techniques, such as hydrostatic pressing or slip casting followed by vacuum sintering, or by hot uniaxial or isostatic

pressing (Matkovic aet al, 1977; Ellis and Goetzel, 1990). The high costs of producing borides and handling brittle products with the necessary care have limited applications to those cases in which the unusual properties of these materials are an essential requirement (Ellis and Goetzel, 1990). Materials scientists have been continuously trying to improve the properties and performance of enginnering materials. Chemistry modifications and conventional thermal, mechanical, and thermo-mechanical processing methods have led to important developments in mechanical, chemical, and physical properties of materials. However, demands for better materials have always being increased which led to the design and development of advanced materials and high-technology industries have given an added stimulus to these efforts (Suryanarayana, 2001). As a result, non-equilibrium processing of materials has attracted the attention of many scientists and engineers because there was a huge potential to produce better and improved materials, which was not possible by conventional methods (Suryanarayana et al, 2001).

The structure and constitution of advanced materials can be better controlled by processing them under non-equilibrium (or far-from equilibrium) conditions and mechanical alloying (MA) is such a processing method by which materials under non-equilibrium conditions can be produced (Suryanarayana, 2001). MA can be defined as a powder metallurgy process for producing composite metal powders with a controlled fine microstructure by repeated cold welding, fracturing and rewelding of powder particles in a high-energy ball mill (Öveçoglu, 1987; Benjamin, 1992; Suryanarayana et al, 2001). It utilizes various types of milling machines in powder blends are exposed to highly energetic compressive forces (Tang et al, 2004).

MA is a simple and versatile technique. Moreover, it is an economically feasible process possessing significant technical advantages. One of the greatest advantages of MA is in the synthesis of novel alloys and composites as well as alloying of normally immiscible elements, which is not possible by any other technique (Öveçoglu, 1987; Benjamin, 1992; Suryanarayana, 2001). The reason for that is that the limitations imposed by phase diagrams do not apply for this process because it is a completely solid-state processing technique (Suryanarayana et al, 2001). In addition to that, MA can produce materials whose internal homogeneity is independent of the initial starting particle size, which is a great advantage over traditional ball milling processes. It is possible to obtain mechanically alloyed

dispersions with less than 1 μm interparticle spacing from initial powder sizes vaying between 50-100 μm (Goff, 2003).

There are different types of high-energy milling equipment with different capacity, efficiency of milling and additional arrangements for cooling, heating, etc, which are used to produce mechanically alloyed powders (Suryanarayana, 2001; Goff, 2003). Spex™ shaker mills are mostly used for laboratory investigations and at a given time they mill about 10±20 g of the powder depending on the density of starting constituents (Goff, 2003). Generally, Spex™ mills have one vial, with the sample and grinding balls inside and this vial is secured in a clamp. These mills shake the milling container in three-mutually perpendicular directions at about 1200 rpm resulting in powder microstructural refinement with time (Suryanarayana, 2001; Goff, 2003). As a result of the ball-to-ball and ball-to-container collisions, the powder constituents are continually trapped and refined with time ultimately leading to an overall homogeneously dispersed microstructure (Goff, 2003).

The material used for the milling container (grinding vessel, vial) and the balls are important because the ball-to-ball and ball-to-container collusions will result small fractions of milling material to fracture off and disperse into the composite powder which leads to contamination of the powder blends (Suryanarayana, 2001; Goff, 2003). Therefore, the most appropriate type of container and milling media for the given system should be chosen (Suryanarayana, 2001).

Another important issue is the ball-to-powder ratio (BPR). Different investigators have used different BPR's varying from a value as low as 1:1 (Bassetti et al, 2005) to as high as 220:1 (Kis-Varga & Beke, 1995). In a small capacity mill, such as Spex™ mill, generally a ratio of 10:1 is used. It is clear that the milling duration gets shorter with increasing BPR (Suryanarayana, 2001).

Milling atmosphere, whose major effect is on the contamination of the powder, is also an important variable for MA process. Therefore, containers have been either vacuumed or filled with an inert gas such as argon or helium before the powders are milled in. Otherwise, the presence of air in the vial causes to produce oxides and nitrides in the powder, especially if the powders are reactive in nature. Because of this, the loading and unloading of the powders into the vial have to be carried out inside an atmosphere-controlled glove box (Suryanarayana, 2001; Fecht, 2002). The

reason that also the unloading is done in a glove box is that most of the powders become reactive as well as explosive with oxygen because their surface areas drastically increase after milling (Suryanarayana, 2001).

Another important issue in MA is the use of process control agents (PCAs). Generally, ductile powder particles are cold-welded to each other, due to the heavy plastic deformation during milling. Because true alloying among powder particles can occur only when there is a balance between cold welding and fracturing of particles, a PCA, generally a surface-active organic compound, is added to the powder mixture during milling to reduce the cold welding and inhibiting the agglomeration (Öveçoğlu, 1987; Suryanarayana, 2001).

The duration of milling is the most significant parameter in the process. In most of the cases, the rate of refinement of the internal structure (particle size, crystallite size, lamellar spacing, etc.) is roughly logarithmic with processing time (Fig.2.3) and therefore the size of the starting particles is relatively unimportant (Suryanarayana, 2001; Fecht, 2002). Generally, the crystallite (or grain) size is refined to nanometer dimensions in a few minutes to an hour. Here, the most important thing is to choose an appropriate milling duration, when there is a steady state between fracturing and cold welding of the powder particles (Suryanarayana, 2001).

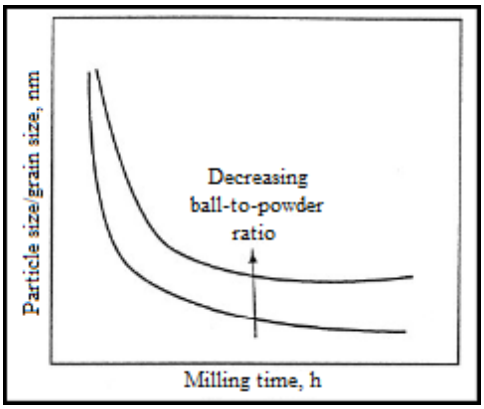

Figure 2.3 : Refinement of particle and grain sizes with milling time, adapted from Suryanarayana (2001).

MA is an advanced fabrication process that can produce ultra-fine and homogenous powders (Ryu et al, 2000). Furthermore, MA which is a well-known process for preparing several amorphous, metal nitrides, metal carbides and alloys, has been considered as a powerful technique even for synthesizing numerous nanostructured materials (with a grain size of few nanometers, usually<100 nm) (El-Eskandarany et

al, 2000). Furthermore, this technique can also be used to induce chemical (displacement) reactions in powder mixtures at room temperature or at much lower temperatures than normally required to synthesize pure metals (Suryanarayana et al, 2001).

In any MA process, firstly initial powder constituents are mixed or blended depending on the desired stoichiometry for a certain composite formulation and are put in an appropriate milling container with the required ball charge. They are milled until a steady state of homogeneous dispersion is achieved (Goff, 2003). The central event of MA is the ball-powder collisions (Fig.2.4) (Fecht, 2002). The force of the impact plastically deforms the powder particles leading to work hardening and fracture (Suryanarayana, 2001; Fecht, 2002), which produces a very fine grain size and substructural strengthening via high dislocation density and fine subgrain size. As a result, MA provides several strengthening mechanisms, such as oxide dispersion strengthening, carbide dispersion strengthening, fine grain size strengthening, substructural strengthening and solid solution strengthening (Öveçoğlu, 1987; Suryanarayana, 2001).

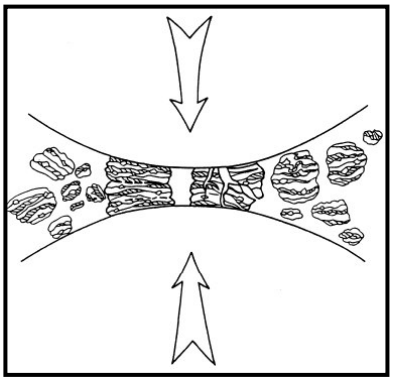

Figure 2.4 : Schematic view of a ball-powder-ball collision, adapted from Suryanarayana (2001).

Considering all scientific points and the foregoing facts, it is clear that research in the area of MA is continuing to develop. There is so much more to learn on the ``science" of MA, and it is assured that the future of MA is wide open for novel discoveries (Coşkun, 2006).

2.1.3 Transition metal borides produced by mechanical alloying (MA)

There are a few studies on transition metal borides produced by mechanical alloying (Welham, 1999; Ricceri and Mateazzi, 2004; Setoudeh and Welham, 2005; Hwang

and Lee, 2002; Tang et al, 2006; Iizumi, 2006; Kudaka et al, 2001; Kim et al, 2008; Colin et al, 2004). Generally, titanium boride (TiB_2) is the most studied transition metal boride produced via mechanical alloying. Welham (1999) and Ricceri and Matteazzi (2004), produced TiB_2 by mechanical alloying through the oxides of Ti and B. In these studies, Mg was used as the reducing agent and both studies used excess (about 10 wt.%) amount of Mg to account for the surface oxidation of the metal and the residual oxygen that could be absorbed onto reactant surfaces and vial-balls surfaces. Furthermore, stainless steel vial and balls were used in both investigations. In the former study (Welham, 1999), milling was performed with a BPR of 43:1 and a rotation speed of 165 rpm. After that, powders were leached for 2 h at room temperature in 1 M HCl solution in order to get rid of MgO, Fe released by the vial and the milling balls and unreacted Mg. In this study, TiB_2 powders were obtained for the milling durations greater than 10 h. On the other hand, Ricceri and Matteazzi (2004) carried out the milling process in a Spex™ mill (1200 rpm) and with a BPR of 18:1. They leached the milled products using 0.5 M HCl for 2 h and claimed to obtain pure TiB_2 powders after 2 h of milling.

Similar to these studies about production of TiB_2, Setoudeh and Welham (2005) produced ZrB_2 through the oxides of Zr and B, where Mg was used as the reducing agent. In this study, milling was performed with stainless steel vials and balls having a BPR of 43:1 and a rotation speed of 165 rpm. After that, powders were leached for 1 h at room temperature in a 0.1 M HCl solution. They obtained pure ZrB_2 powders after 15 h of milling and they also recommended that using a stoichiometric excess of both Mg and B_2O_3 would ensure that all the ZrO_2 is consumed because ZrO_2 is difficult to be removed by dissolution (Setoudeh and Welham, 2005).

On the other hand, Hwang and Lee (2002) and Tang et al (2006) and produced TiB_2 through the elemental Ti and B. Both research groups used stainless steel vial and balls with a BPR of 10:1. Hwang and Lee (2002) used a rotating speed of 80 rpm and could only obtain TiB_2 after 280 h of milling. In this study, very long milling time can probably be attributed to the low rotation speed used in the process, since Tang et al (2006) used a rotation speed of 700 rpm and produced TiB_2 after a milling duration of 60h. On the other hand, Iizumi et al (2006) produced NbB_2 powders by mechanical alloying of metallic Nb and amorphous B powders in a planetary ball

mill (600rpm) after 30 h where they used stainless steel vial and balls with a BPR of 20:1.

Similarly, MoB_2 and Mo_2B_5 were produced by Kudaka et al (2001) from the elemental Mo and B. They carried out the milling process using cemented tungsten carbide vial and balls in planetary ball mill with a rotation speed of 650 rpm and a BPR of 7.5:1. MoB_2 powders were obtained after milling for 40 h and the mixture of MoB_2 and Mo_2B_5 was obtained after annealing the MoB_2 powders milled for 40h (Kudaka et al, 2001).

In addition to these studies, Kim et al (2008) produced TiB_2 and VB_2 through the mechanochemical reactions as;

$$TiCl_3 + 2LiBH_4 + LiH = TiB_2 + 3LiCl_3 + 4{,}5H_2^{\uparrow} \quad \textbf{(2.1)}$$

$$VCl_3 + 2LiBH_4 + LiH = VB_2 + 3LiCl_3 + 4{,}5H_2^{\uparrow} \quad \textbf{(2.2)}$$

They used cemented tungsten carbide vial and balls with a BPR of 30:1. They successfully obtained TiB_2 and VB_2 powders after milling in a planetary ball mill with a rotation speed of 500 rpm for 4 h. They removed $LiCl_3$ by rinsing several times in distilled water, ethanol and acetone (Kim et al, 2008).

Finally, Colin et al (2004) produced HfB_2 from $HfCl_4$, elemental B and Mg. They used stainless steel milling medium and a planetary ball mill with a rotation speed of 710 rpm. The BPR was 20:1 and they decided that the optimum synthesis conditions were 1 h milling with a 50 wt.% excess amount of Mg and B. However, their end product also contained HfO_2, MgO and Fe beside HfB_2 (Colin et al, 2004).

However, in literature, there is no comprehensive study on the production of tungsten borides by mechanical alloying. The only exception is the study of Stubicar at al (1995), who made a X-ray diffraction study of elemental W-B mixtures after high-energy ball milling. They milled different ratios of W-B mixtures in air atmosphere using a planetary ball mill and cemented tungsten carbide milling medium with a BPR of 20:1. They synthesized WB, W_2B and WB_4 after milling up to 5 h using different W:B ratios. However, their end product always contained elemental W, WC and B_2O_3 phases beside tungsten borides. Moreover, they could not detect any W_2B_5. Most importantly, they did not perform any attempts to purify their product and to remove the contamination except some recommendations (Stubicar at al, 1995).

Therewithal, there are some more recent encouraging studies, where Ricceri and Matteazzi in 2003 produced elemental B and elemental W by mechanical alloying from B_2O_3 and WO_3, respectively. They used Mg as the reducing agent and MgO, which was one of the end products beside B and W, was removed by leaching in 2.0 M HCl for 2 h. They used a Spex™ mill with a BPR of 24:1 and stainless steel milling medium. They claimed to obtain reduced W and B after only 8 and 9 min. of milling, respectively (Ricceri and Matteazzi, 2003a; Ricceri and Matteazzi, 2003b).

2.2 Tungsten Oxide System

In this section, detailed information about the properties tungsten oxides, their nanostructures, CNTs and tungsten oxide/CNT hybrid materials will be given and their application areas as well as their production routes will be discussed thoroughly.

2.2.1 Tungsten oxides and their nanostructures

Tungsten oxides have received a lot of attention because of their interesting electrochromic, photochromic and gasochromic properties (Shah, 2009; Nanba et al, 1991; Lillard et al, 1998; Mwakikunga et al, 2008; Ma et al, 2006). Because of this reason, they have been used in flat panel displays, photo-electro-chromic 'smart' windows, storage devices, humidity and temperature sensors, catalysts, optical modulation devices, electron emitters, and gas sensors for NO_2, CO, CH_4, H_2, NH_3, H_2S and ozone (Berger et al, 2004; Shah, 2009; Lillard et al, 1998; Mwakikunga et al, 2008; Ma et al, 2006; Boulova et al, 2001; Liu et al, 2005; He and Zhao, 2008). Several oxide phases exist in the W-O system; the oxide WO_3, the homologous series of monoclinic oxides W_nO_{3n-1}, the homologous series of monoclinic oxides W_nO_{3n-2}, including $WO_{2.92}$ and $WO_{2.90}$, the monoclinic oxide $WO_{2.83}$, the monoclinic oxide $WO_{2.72}$ ($W_{18}O_{49}$) and the monoclinic oxide WO_2 (Fig. 2.5) (Wriedt, 1989).

Tungsten trioxide (WO_3) has a cubic perovskite-like structure based on the corner sharing of WO_6 regular octahedron, with O atoms at the corner and W atoms at the centre of each octahedron. This structure exhibits several transitions in the symmetry of the structure, with the sequence of tetragonal (1170-1700 ^oK), orthorhombic (600-1170 ^oK), monoclinic (290-600 ^oK), triclinic (230-290 ^oK) and monoclinic (0-230

^{o}K) as the temperature is decreased from its melting point (1700 ^{o}K) to absolute zero (Cox, 2005).

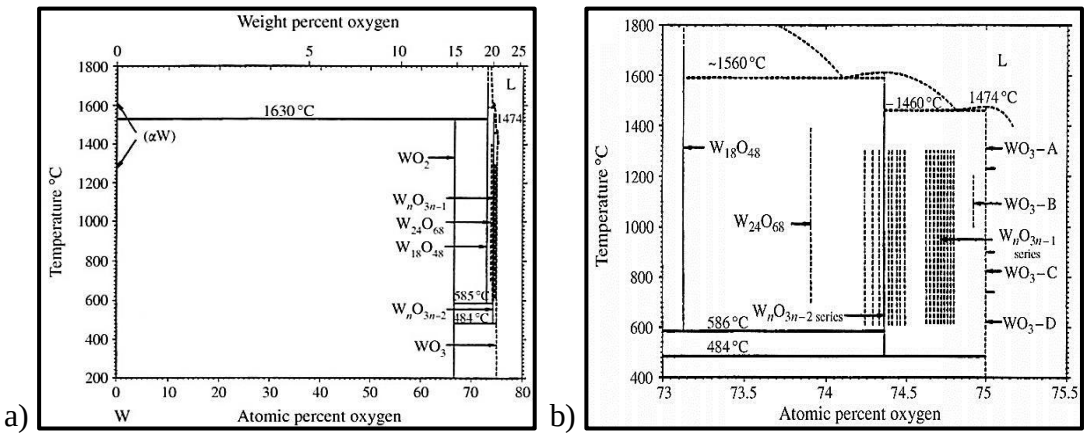

Figure 2.5 : a) W-O Phase diagram and b) detail of W-O Phase diagram, adapted from Berger et al (2004).

In addition, it should be noted that tungsten trioxide structure is likely to include several kinds of defects (Wriedt, 1989). Moreover, in most investigations, the products of tungsten oxides are mixture of WO_3 and its sub-oxides with complex crystallographic defects. It is well-known that various important features of the materials are not governed only by the structure of material itself but by faults or defects in these materials (Zhang et al, 2004). High-purity stoichiometric oxides exhibit intrinsic electronic conduction only at high temperatures. At low temperatures, the electrical conductivity of stoichiometric WO_3 is similar to an extrinsic semiconductor with shallow donor levels resulting from interstitial impurities or defects (Berger et al, 2004). In this system, one of the most observed defects is the lattice oxygen vacancy, where the oxygen atom is absent from a normal lattice site. It causes the formation of WO_{3-x} compounds and influences the electric properties of non-stoichiometric tungsten oxide. As a result, these oxygen vacancies lead donor-like effects for electrons and result in the n-type semiconducting properties of non-stoichiometric tungsten oxide (Xu et al., 1990). The tungsten dioxide (WO_2), which was one of the first oxides recognized in the W-O system (Wriedt, 1989), has a distorted rutile type structure and is characterized by metal-doublet formation by the metal atoms of the edge-sharing WO_6 octahedra. This rutile structure makes the oxide to become metallic through cation-cation and/or cation-anion-cation interactions (Berger et al, 2004). A detailed crystallographic data of different phases belonging to the W-O system is given below in the Table 2.3.

WO_2, which is a sub-stoichiometric tungsten oxide, is commonly used as a catalyst in the isomerization reactions of hydrocarbons (He and Zhou, 2008¸ Katrib et al, 1995) and in the selective oxidation of organic substrates (Davico et al, 1999) because of its intrinsic crystal and electronic structure. Among other transition metal dioxides, the oxygen deficient structure and the strong metal-metal bonds inherent to the crystal structure of WO_2 makes it a good conductor (Ben-Dora and Shimony, 1974; Jones et al, 1997; Jiang and Spence, 2004). Because of this oxygen deficient structure, it could also be employed as optical recording films (Aoki et al, 2006).

Table 2.3 : Crystallographic data for oxide phases in the W-O system, adapted from Berger et al (2001).

Phase	Space group	a (nm)	b (nm)	c (nm)	a (deg)	Unit cell volume (mm^3)	Density (g/cm^3)
WO_3, α-Phase	Monoclinic, P21/n	0.7297	0.7539	0.7688	90.91	0.4229	7.283
$WO_{2.92}$ [$W_{25}O_{73}$]	Monoclinic, 2P/n	1.1930	0.3820	5.9720	98.30	2.263	7.108
$WO_{2.90}$ [$W_{20}O_{58}$]	Monoclinic, 2P/m	1.2050	0.3767	2.3590	94.72	1.0672	7.160
$WO_{2.83}$ [$W_{24}O_{68}$]	Monoclinic	1.9310	0.3781	1.7070	104.40	1.2071	-
$WO_{2.72}$ [$W_{18}O_{49}$], γ-Phase	Monoclinic, 2P/m	1.8280	0.3755	1.3980	115.14	0.8729	7.958
WO_2, δ-Phase	Monoclinic, P21/n	0.5605	0.4892	0.5550	120.42	0.1330	10.82

On the other hand, while the stable monoclinic room-temperature phase has metal like band structure, the high-temperature metastable orthorhombic phase can be identified as a semiconductor with a band gap of about 0.6 eV. It was shown, that oxygen vacancies in the monoclinic phase may transform the metallic compound to indirect band-gap semiconductor with the $WO_{1.75}$ stoichiometry while the semiconducting nature is still preserved for the orthorhombic phase with oxygen vacancies (Shaposhnikov et al, 2011). Moreover, it has been reported that pure H_2 could be produced by contacting particularly WO_2 surface with steam below 700 ^oC (Seitzer, 1975). Lately, the turn-on field for electronic emission of tungsten oxide nanorods ($WO_{2.9}$) could be tuned via controlling the WO_2 content (Liu et al, 2005).

There are different methods, like chemical vapor deposition (Shankar et al, 2007), solvothermal routes (Choi et al, 2005), acid precipitation routes (Nimittrakoolchai and Supothina, 2008; Kida et al, 2009; Balazsi et al, 2008; Balazsi et al, 2009; Supothina et al, 2007), sol-gel approach (Pinna and Niederberger, 2008; Satishkumar et al, 2000; Niederberger et al, 2002) and hydrothermal methods (Huirache-Acuna, 2009; Therese et al, 2005; Ha et al, 2005; Song et al, 2007) which are used to fabricate tungsten oxide nanostructures. Mostly, while methods like chemical vapor deposition (CVD) requires high synthesis temperatures (Shankar et al, 2007), wet-

chemical methods like sol-gel, precipitation, solvo- and hydrothermal routes require either several steps (Nimittrakoolchai and Supothina, 2008; Balazsi et al, 2008; Balazsi et al, 2009; Supothina et al, 2007; Wang et al, 2009; Niederberger et al, 2002; Huirache-Acuna, 2009; Therese et al, 2005; Ha et al, 2005; Song et al, 2007), relatively high temperatures (Choi et al, 2005; Nimittrakoolchai and Supothina, 2008; Balazsi et al, 2009; Supothina et al, 2007; Wang et al, 2009; Niederberger et al, 2002; Huirache-Acuna, 2009; Therese et al, 2005; Ha et al, 2005; Song et al, 2007) or long synthesis times (Kida et al, 2009; Supothina et al, 2007; Wang et al, 2009; Niederberger et al, 2002; Huirache-Acuna, 2009; Therese et al, 2005; Ha et al, 2005; Song et al, 2007; Satishkumar et al, 2000), which are time and energy consuming and sometimes lead to some problems like undesired change in particle morphology (Polleux et al, 2006).

Recently, 1-D nanostructures of tungsten oxide, which are nanorods, nanotubes and nanowires, have been studied (Mwakikunga et al, 2008; Ma et al, 2006; Su and Lin, 2009; Baek et al, 2006; Gu et al, 2006; Shingaya and Takayama, 2008). These one dimensional nanostructures possess different physical and chemical properties compared to those of the bulk materials (Ma et al, 2006). They can also be used for manufacturing new nanodevices because of their unique architecture (Su and Lin, 2009; Baek et al, 2006; Gu et al, 2006). Choi et al (2005) obtained tungsten oxide nanostructures by using the solvothermal treatment of WCl_6 in an ethanol solvent at 200 ^oC for 10 h. The various crystalline phases of tungsten oxide, such as monoclinic $W_{18}O_{49}$ nanorods, hexagonal WO_3 platelets and monoclinic WO_3 nanosheets were synthesized by simply changing the composition of the solvent. The oxygen in water played an important role in the final tungsten oxide phase. Especially, $W_{18}O_{49}$ nanorods grew to nanowires as the concentration of WCl_6 decreased. Using this process, it was possible to control the crystalline phase and morphologies of the nanostructured tungsten oxide system (Choi et al, 2005). WO_3 nanostructures were produced by Song et al (2007) and Gu et al (2006) via a hydrothermal route in the presence of K_2SO_4, which was demonstrated as a structure directing agent. Song et al (2007) dissolved Na_2WO_4 in deionized water to form a transparent solution followed by adding an HCl solution dropwise into the solution under continuous stirring until tungstic acid was precipitated thoroughly. Then K_2SO_4 was added to the system, agitated to form starchiness, and then transferred into Teflon-lined autoclave with a

capacity of 50 ml, where hydrothermal treatments were carried out at 180 °C for 12 h. Finally, WO_3 nanowires were collected (Song et al, 2007). On the other hand, Gu et al (2006) selectively produced some urchin-like and ribbon-like structures of WO_3 by adding Rb_2SO_4 and K_2SO_4, respectively, to the WO_3 solution prepared by adding Na_2WO_4 and $H_2C_2O_4$ to distilled water. In addition to these, 1-D self-assembled WO_3 nanostructures were synthesized by a hydrothermal route using Na_2WO_4 and EDTA salts of sodium or ammonium and Na_2SO_4 (Ha et al, 2009). In that study, the mixed slurry solution was transferred to a 100 mL Teflon-lined stainless steel autoclave and hydrothermal reaction proceeded at 140-180 ◦C for 4-12 h in a preheated electric oven. When sodium based EDTA salts were used, urchin-like structures similar to those in the study of Gu et al (2006) were synthesized instead of nanowires formed with addition of ammonium based EDTA salts (Ha et al, 2009). Differently, WO_{3-x} nanorods and nanowires were prepared on the tips of electrochemically etched tungsten filament by heat treatment of the tips in Ar and H_2 atmosphere (Zhang et al, 2004; Gu et al, 2002). Gu et al (2002) prepared $W_{18}O_{49}$nanowires on metal tungsten tips, where tungsten tips were first prepared with electrochemical etching of tungsten wires by using 1 M KOH and applying 2 V. Afterwards, the tungsten tips were introduced to a tube furnace immediately, which was heated at 700 °C in high purity Ar atmosphere for 10 min. Tungsten oxide nanowires growth resulted from the oxygen leakage of their system (Gu et al, 2002). Similarly, different types of tungsten oxide nanorods were synthesized on the tungsten tips prepared by electrochemical etching of tungsten wires at different temperatures under H_2/Ar or Ar for 10 min (Zhang at al, 2004). On the other hand, a mixture of WO_2-WO_3 nanorods could also be synthesized by the sonochemical approach, where Koltypin et al (2002) ultrasonicated $W(CO)_6$ in diphenylmethane (DPhM) followed by a heat treatment. In this study, the slurry of $W(CO)_6$ in DPhM was sonicated for 3 h at a temperature of 90 ^oC under a gas mixture of 20% O_2 - 80% Ar. Alternatively, carbon nanotubes (CNTs) were also used as templates to obtain WO_3 nanorods (Satishkumar et al, 2000). Satishkumar et al (2000) prepared an aqueous solution of Na_2WO_4 that was passed through a cation exchange column. The resulting tungstic acid (H_2WO_4) was used for coating the acid-treated carbon nanotubes by magnetic stirring for 48 h. Carbon nanotubes were removed by a heat treatment at 700 ^oC in air and WO_3 nanorods were obtained (Satishkumar et al, 2000).

All of the above mentioned methods include several steps and addition of directing agents like M_2SO_4 (M=K, Na, etc.) or CNTs create other requirements like removal of these agents or other by-products. Moreover, solvo-and hydrothermal techniques are generally low yield techniques. To avoid these handicaps, thermal methods were proposed, which are easy and free from any contamination. Various thermal methods were used to prepare WO_2 nanorods (Ma et al, 2006), WO_{3-x} nanostructures (Chi et al, 2006), $W_{18}O_{49}$ nanorod bundles (Su and Lin, 2009), WO_x nanorods (Shingaya and Nakayama, 2008) and $W_{18}O_{49}$ nanowires (Chen and Mori, 2009). Ma et al (2006) synthesized WO_2 nanorods on Si wafers using reactive thermal evaporation with no catalyst. They used two W filaments. The surfaces of these filaments were first reduced by hydrogen at 10 Torr and 2000 ^oC for 10 min and then an argon flow was introduced into the vacuum chamber at a flow rate of 50 scc/min, controlled using a mass flow controller. For synthesizing the large-area 1D WO_2 nanorods, the W filaments were heated to 1500 ^oC for 30 min at a pressure of ~10 Torr. Finally, large-area arrays of 1D WO_2 nanorods grew on clean Si wafers (5x5 mm^2) that were placed on two W filaments (Ma et al, 2006). Similarly, Chi et al (2006) prepared tungsten oxide nanostructures by hot-filament thermal deposition. By controlling the tungsten filament temperature, they synthesized several types of WO_{3-x} nanostructures. They maintained the same oxygen level for each experiment. To produce the nanostructures, they placed the tungsten filaments in a vacuum chamber that was first evacuated down to about 4.0×10^{-2} Torr. Subsequently, high purity argon gas was introduced into the chamber and the pressure in the vacuum chamber was adjusted as 0.6 Torr. Then the filaments were heated up to a temperature of 1300 ^oC for 30 min and nanostructures were synthesized on Si substrates (10x10 mm^2)(Chi et al, 2006). On the other hand, Su and Lin (2009) directly prepared $W_{18}O_{49}$ nano-bundles by a high-temperature physical route without substrates or catalysts. They placed bulk tungsten in a copper crucible and evaporated it with a high-energy plasma arc in an oxygen deficient environment at a pressure of 760 Torr (Ar-O_2 ratio 10:1). After the experiment was done, they collected the final dark blue product from the chamber (Su and Lin, 2009). $W_{18}O_{49}$ nanowires were prepared in another study (Chen and Mori, 2009) by heat treatment of a tungsten filament. The heat treatment was carried out under high vacuum conditions at pressures lower than 10^{-6} Pa. The tungsten filament was first heated up to ~873 K and maintained at this temperature

to enable the gradual formation of tungsten oxide nanowires on its surface (Chen and Mori, 2009). Shingaya and Nakayama (2008) synthesized WO_x nanorods in an ultrahigh-vacuum chamber. A single-crystal tungsten substrate was cleaned by the oxidation method and heated to 1000 K in oxygen atmosphere at a pressure of 1×10^{-5} Torr. Then, after oxidizing the substrate surface, oxides were sublimated by raising the temperature to 1600 K. Another effect of this treatment was the removal of impurities. Preparation of the surface of the single crystal of tungsten used as the substrate for growth of WO_x nanorods was completed by repeating this operation several times. An interesting study (York et al, 1999) is about epitaxial growth of WO_{3-x} needles on $(10\bar{1}0)$ and $(01\bar{1}0)$ WC surfaces produced by controlled oxidation with CO_2. The synthesis was performed inside a controlled environment transmission electron microscope (CETEM), and also in a standard flow reactor; the tungsten oxide needles consisted mainly of distorted γ-$WO_{2.72}$ (York et al, 1999).

As clearly stated above, processes such as vapor deposition and thermal evaporation used in these methods are generally carried out at high temperatures and require technically complex and expensive experimental setup.

2.2.2 Carbon nanotubes (CNTs)

With the observation of the C_{60} fullerene by Smalley et al (1985) a new era in carbon chemistry started (Kroto et al, 1985). C_{60}, which is called a buckyball, is a closed, convex structure of 60 carbon atoms arranged in hexagons and pentagons. 6 years after the discovery of buckyballs, Iijima discovered carbon nanotubes which are an elongated form of C_{60} (Iijima, 1991). A carbon nanotube can be considered as a hollow cylinder formed by rolling a graphite layer (graphene) and joining its edges along the cylinder axis. In the same way as a graphite layer, the tube is composed of carbon atoms each joined to three neighbors by strong sp^2-hybridised σ bonds forming a honeycomb lattice, with hemispherical, half-fullerene endcaps (Dresselhaus et al, 1996; Iijima, 1991).

Depending on their number of layers, the tubes are termed single, double, triple, or multiwall (SWNT, DWNT, TWNT and MWNT, respectively). SWNTs have just one graphene sheet, while MWNT`s consist of many graphene sheets within one another and arranged concentrically, like Russian dolls, and separated by a distance of typically 0.34 nm (Dresselhaus et al, 1996). Typical nanotube diameters range from

0.7 nm to 15 nm for SWNTs and 10 to 100 nm for MWNTs. Recent improvement in nanotube synthesis have led to CNTs with lengths of the order of centimeters (Hata et al, 2004) and, in general, CNTs with aspect ratios of 10 - 10^7 are routinely produced. The structure of a tube can be geometrically related to a graphene sheet by the chiral vector $C_n = na_1 + ma_2$, which defines the direction of rolling a sheet relative to the origin (0,0) to form a specific nanotube (Dresselhaus et al, 1996), as shown in Figure 2.6.

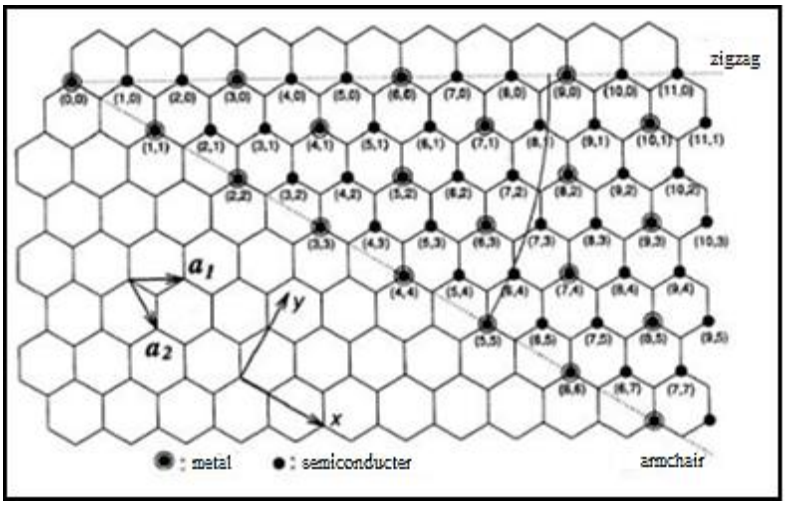

Figure 2.6 : Schematic of a graphene sheet with unit vectors a_1 and a_2, adapted from Dresselhaus et al (1996).

The orientation of the six-membered carbon ring in the honeycomb lattice relative to the tube axis defines the nanotube's chiral angle (θ) and the chiral angle of SWNTs gives rise to three types of tube structures termed armchair, zig-zag and chiral, corresponding to chiral angles of $\pm 30^o$ (when (n,m) =(2p,-p), for p an integer), 0^o((n,m) = (p,0)) and others, respectively (Rao and Nath, 2003). Schematic representation of the folding of a graphene sheet into zigzag, armchair and chiral nanotubes is given in Figure 2.7.

In reality, the structure of CNTs differs from a perfect graphene layer and contains defects in the hexagonal lattice such as vacancies, functionalities and topological defects (Mackay and Terrones, 1991). The presence of structural defects in nanotubes is equivalent to a low degree of graphitization and can be determined experimentally using techniques such as Raman spectroscopy (Capek, 2009).

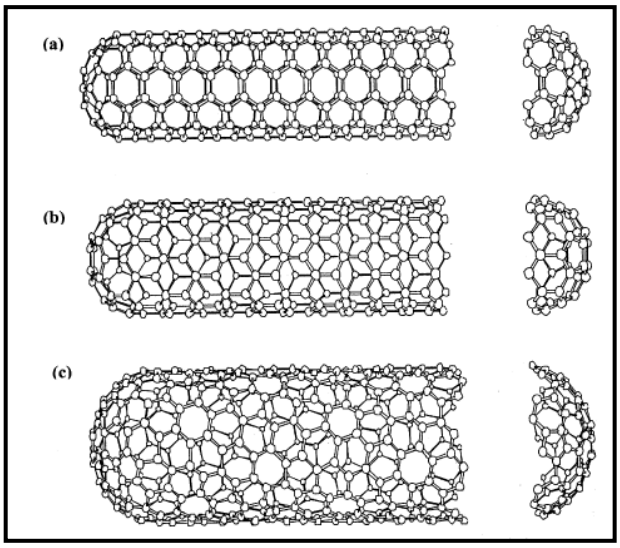

Figure 2.7 : Schematic representation of the folding of a graphene sheet into a) zigzag, b) armchair and c) chiral nanotubes, adapted from Rao and Nath (2003).

Some of the most interesting properties of CNTs are low density, high thermal conductivity (twice that of diamond), thermal stability under vacuum up to 2800 ^{o}C and high electrical conductivity (1000 times the current carrying capacity of copper wires). Moreover, they have very good mechanical properties because of the carbon sp^2 bonds. A summary of the physical properties of CNTs are given in Table 2.4.

Table 2.4 : Physical properties of CNTs, adapted from Eder (2010).

Property	SWCNTs	MWCNTs	Graphite
Specific gravity	0.8 g/cm^3	<1.8 g/cm^3	2.26 g/cm^3
Elastic modulus	~1.4 TPa	~0.3-1 TPa	1 TPa (in plane)
Strength	50-500 GPa	10-60 GPa	
Resistivity	5-50 μΩ cm		50 μΩ cm (in plane)
Thermal Conductivity	3000 W m^{-1} K^{-1}		3000 W m^{-1} K^{-1} (in plane) 6 W m^{-1} K^{-1} (c-axis)
Magnetic susceptibility	22x10^6 EMU/g (perpendicular) 0.5 x 106 EMU/g (parallel)		0.5 x 10^6 EMU/g (parallel)
Thermal expansion	negligible		-1 x 10^{-6} K^{-1} (in plane) 29 x 10^{-6} K^{-1} (c-axis)
Thermal stability	600-800 ^{o}C in air 2800 ^{o}C in vacuum		450-650 ^{o}C in air

In contrast to the purely metallic MWCNTs, a SWNT can be metallic or semiconducting depending on the diameter and chirality. Low-temperature STM and scanning tunneling spectroscopy (STS) studies of SWNTs revealed the atomically resolved micrographs of the graphene cylinders and their size-specific transport properties consistent with theoretical predictions (Quyang et al, 2002). Carbon

nanotubes behave as field effect transistors and have potential application in nanoelectronics. Moreover, they can be used in vacuum microelectronic devices because of their field emission properties. Flat panel displays, lamps, gas discharge tubes providing surge protection and X-rays have been developed using carbon nanotubes as field emission source (Saito, 2003). Carbon nanotubes produced by ferrocene pyrolysis deposited on a tungsten tip exhibits high emission current densities with good performance characteristics (Rao et al, 2001). The high electrochemically accessible surface area of porous nanotube arrays, combined with their high electronic conductivity and useful mechanical properties, makes them attractive as electrodes for devices employing electrochemical double-layer charge injection. Gas and glucose sensors based on carbon nanotubes have been developed (Davis et al, 2003). The high capacitance of SWNTs is being exploited for applications. Early reports that carbon nanotubes can store considerable amounts of hydrogen created high expectations (Dillon et al, 1997; Chambers et al, 1998). Additionally, it has been suggested that CNTs would be ideal for use in energy production and storage (Tasis et al, 2006).

Despite these excellent properties, the problem is that the CNTs vary widely depending on the production method used to grow the CNTs, number of defects in the structure and whether nanotubes are SWNTs or MWNTs. SWNTs have a higher aspect ratio and greater surface area than MWNTs, which allows more interfacial bonding. However, SWNTs are much harder to produce in large quantities and to process compared to MWNTs (Dresselhaus et al, 1996).

In general, there are four main routes in producing CNTs, which are arc discharge, laser ablation, molten salt and chemical vapor deposition (CVD) routes (Mamalis et al, 2004). The arc discharge method was used by Iijima (1991) when he discovered CNTs. Using this method, very pristine CNTs can be synthesized but they are accompanied by many nanoparticles and have a yield of only 2% after purification. Like arc discharge method, laser ablation method and molten salt can also yield to high quality CNTs but the efficiency is still low when compared to CVD method (Dresselhaus et al, 1996; Eder, 2010). In Table 2.5, properties of different CNT synthesis techniques are given.

CVD is the most widely used route in which a great quantity of CNTs can be obtained at low cost (Dresselhaus et al, 1996). It involves the catalytic decomposition of hydrocarbons on nanosized metal particles, such as Fe, Co, Ni, Cu, Mo or Pt. If the temperature of the reaction increases, the degree of graphitization increases and the amount of the defects in the CNT structure decreases. However, while CVD does yield a great quantity of CNTs compared to other methods, the CNTs made using this route have the highest amount of defects, including topological defects, rehybridisation and incomplete bonding (Liu et al, 2001).

Table 2.5 : Properties of different CNT synthesis techniques, adapted from Eder (2010).

Synthesis Technique	Product	Advantages	Disadvantages
DC arc discharge	MWCNTs and SWCNTs (with catalysts)	Easy design, few structural defects	Short tubes and low yield, low purity, random diameters
Laser ablation	Primarily SWCNTs	Few defects, good control over diameter	Most costly method, poor scalability, requires Class 4 lasers
Molten salt	Primarily MWCNTs	Simple process, used for filling CNTs	Low yield and crystallinity, poor controllability
Chemical Vapor Deposition	Both types	High yields, easy scalability, long tubes, alignment and pattern growth	Some defects, medium purity

In CVD method, controlling growth direction of CNTs on a substrate can be achieved and a large quantity of nanotubes can be synthesized. In this process, a mixture of hydrocarbon gas, acetylene, methane or ethylene and nitrogen is introduced into the reaction chamber. During the reaction, nanotubes are formed on the substrate by the decomposition of the hydrocarbon at temperatures of 700–900 °C and atmospheric pressure (Xie et al, 2000). In this route, catalyst particles are deposited onto a substrate, and individual single-walled carbon nanotubes with uniform diameters are grown at elevated temperatures (>600 °C) from the catalyst particles, using for instance methane or an alcohol vapor as the carbon source. A stimulating feature of this route is the possibility to control the diameter of the produced tubes through the size of the catalyst particles (Li et al, 2001). The process has two main advantages; the nanotubes are obtained at much lower temperature, although this is at the cost of lower quality, and the catalyst can be deposited on a substrate, which allows for the formation of novel structures (Mamalis et al, 2004).

To be able to benefit the optimal properties of the CNTs for many applications, they need to be functionalized to improve both their wettability and dispersibility (Dyke and Tour, 2004). There are three main methods for functionalizing, which are covalent functionalization by attaching functional groups to CNT ends, sidewalls and defect sites, noncovalent functionalization by wrapping individual CNTs with various species of polymers, surfactants and biomolecules and endohedral filling using the inner cavity of the CNTs for doping (Hirsh, 2002; Niyogi et al, 2002; Lin et al, 2003; Tasis et al, 2006; Dyke and Tour, 2004).

Chemical oxidation is by far the most common route to functionalize the CNTs, for both enhancing their reactivity and enabling them to disperse better in solvents like water, ethanol etc. HNO_3, H_2SO_4, $KMnO_4$, OsO_4 and RuO_4 are the most common used oxidizers (Hirsh and Vostrowsky, 2005; Hirsh, 2002). This route attaches a various functional groups to the ends and side walls defects (Fig.2.8), like carboxyl (-COOH), carbonyl (-C=O) and hydroxyl (-OH) groups, while also purifying the CNTs, ridding them of any amorphous carbon, nanoparticles and catalyst residues (Zhao et al, 2004; Hirsh and Vostrowsky, 2005). Sonication of the acid/CNT mixture during functionalization can increase the reaction and also create more defects in the CNTs, offering more sites for functional groups to attach (Hirsh and Vostrowsky, 2005).

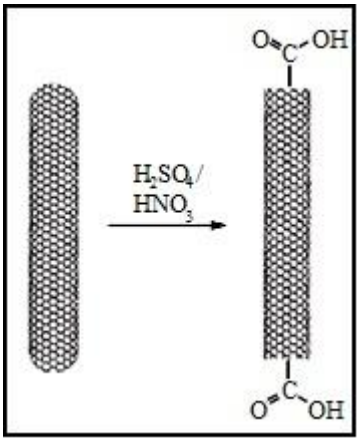

Figure 2.8 : Schematic representation of chemical oxidation, adapted from Hirsh and Vostrowsky (2005).

2.2.3 Tungsten oxide-CNT hybrid systems

The term hybrid materials/composites are used when both the organic and inorganic materials are combined (Kickelbick, 2007; Chujo, 2007). However, it is necessary to

call the materials “hybrid materials” when the level of mixing of the different types of materials is at the nanometer level, or sometimes at the molecular level (Chujo, 2007). The most obvious advantage of hybrids is that they can favorably combine the different features of organic and inorganic components in one material. They provide the opportunity to invent an almost unlimited set of new materials with a large spectrum of properties because of the many possible combinations of components (Kickelbick, 2007).

There are many advantages of using CNTs in hybrid materials including their high aspect ratio (>1000) and tubular geometry that provides ready gas access to a large specific surface area and percolation at very low volume fractions. Moreover, their excellent mechanical, electrical, and optical properties make CNTs an ideal constituent for hybrid materials. The high thermal conductivity of CNTs enable them to behave as a heat sink during calcination and activation treatments, thereby stabilizing small inorganic components that can decorate the sidewalls of the CNTs. As a result, materials with higher specific surface areas that allow the use of less material, reducing cost and toxicity could be produced. Over the past few years, CNTs have been combined with a variety of inorganic compounds, such as oxides, nitrides, carbides, chalcogenides, as well as ceramics and among these compounds, the oxides are by far the most commonly studied inorganic compound (Eder, 2010). A detailed list of inorganic compounds used in CNT hybrid materials, their synthesis techniques and applications are given in Table 2.6.

There are few studies about tungsten oxide-carbon nanotube hybrids/composites. Shankar et al (2006) grown tungsten oxide (WO_x, x = 2.9-3) nanorods on two types of CNT substrates, namely a Si [100] wafer with dispersed multiwalled CNT and a fresh-grown multiwalled CNT film, under typical diamond growing conditions in a hot-filament chemical vapor deposition (CVD) system. The deposition was carried out at a substrate temperature of ~850 °C and at a system pressure of 25 Torr under a H_2/CH_4 atmosphere for 2 h. The morphology of the rods was similar to that seen on the bare Si surface, but they were grown out radially from CNTs and completely covered the surface of the CNTs. In the second case, the density of the CNTs is orders of magnitude larger than the first case and the surface coverage of WO_x nanorods is also noticeably higher. Furthermore, the surface density of the nanorods on the CNT in both cases was much higher than that on the bare Si surface, implying

that CNT may be better nucleators of tungsten oxide than Si. The templated growth on the CNT provided an order of magnitude increase in the surface area covered by tungsten oxide, which may give rise to very interesting functional structures for use as gas sensors, catalysts and electrochromic devices (Shankar et al, 2006).

Table 2.6 : Inorganic compounds used in CNT hybrid materials, their synthesis techniques and applications, adapted from Eder (2010).

Inorganic compound	Synthesis route	Applications
Al_2O_3	ex situ – non-covalent, in situ - hydrothermal, in situ - sol-gel, CVD, PVD	Field emission, oxidation resistance
$BaSrO_2$	PVD	Field emission
CeO_2	in situ - sol-gel, in situ - hydrothermal	Heterogeneous catalysis, gas sensors
Co_3O_4	in situ - sol-gel, CVD	Magnetics, batteries
Cu_2O	in situ - hydrothermal	Photocatalysis
Eu_2O_3	ex situ – non-covalent, in situ - hydrothermal	Diodes, lasers
Fe_xO_y	ex situ - covalent, in situ - hydrothermal	Magnetics, biosensors, heterogeneous catalysis
HfO_2	PVD	Oxidation resistance
MgO	PVD	Field emission, electrocatalysis
MnO_2	in situ - electrochemical, in situ - electrodeposition, in situ - hydrolysis, CVD	Electrocatalysis, heterogeneous, catalysis, supercapacitors, oxidation resistance
MoO_2	in situ - hydrolysis	Electrocatalysis
NiO	in situ - sol-gel, CVD	Supercapacitors
RuO_2	in situ - electrodeposition, in situ - sol-gel, in situ - hydrothermal, PVD, CVD	Supercapacitors, biosensors, heterogeneous catalysis
SiO_2	ex situ - covalent, in situ - sol-gel, PVD	Field emission, oxidation resistance
SnO_2	in situ - sol-gel, in situ - hydrothermal, CVD	Gas sensors, electrocatalysis, nanofluids, batteries
TiO_2	ex situ - covalent, ex situ – non-covalent, in situ - electrodeposition, in situ - micoemulsion, in situ - sol-gel, in situ - hydrothermal, CVD	Photocatalysis, optoelectronics, biosensors, electrocatalysis, batteries, supercapacitors, oxidation resistance
VO_2, V_2O_5	in situ - electrochemical	Batteries, heterogeneous catalysis
WO_3	in situ - electrochemical	Gas sensors, heterogeneous catalysis
ZnO	in situ - electrochemical, in situ - hydrothermal, in situ - micoemulsion, in situ - sol-gel, PVD, CVD	Photocatalysis, optoelectronics, diodes, lasers, field emission
ZrO_2	ex situ – non-covalent, in situ - hydrothermal, CVD, PVD	Oxidation resistance, dielectric devices, heterogeneous catalysis, chemical sensors
Carbides (Fe, W, Ta, Ti)	in situ - electrochemical, in situ - sol-gel, CVD	Heterogeneous catalysis, electrochemistry, field emission
Chalcogenides (Zn, Cd, Hg; X=S, Se, Te)	ex situ - covalent, ex situ – non-covalent, in situ - electrochemical, in situ - hydrothermal, in situ - sol-gel	Optoelectronics
Nitrides (Ti, Fe)	in situ - sol-gel, PVD, CVD	Field emission

Interestingly, WO_3 coated SWCNT bundles were used as templates to synthesize WS_2 nanostructures at 900 ^oC in the presence of a N_2/H_2S flow (Whitby et al, 2002). On the other hand, the growth of WO_x on a MWCNT template may give very interesting functional structures for use as gas sensor, catalyst, and electrochromic devices because MWCNT can be grown easily on patterned substrates to give a variety of forms (Fukunga et al, 1998). Rajesh et al (2002) produced Pt-WO_3 incorporated CNTs in order to maximize the utilization and to increase the stability for methanol oxidation, and these materials have been used as the electrode material for methanol oxidation in comparison with the commercially available electrodes.

On the other hand, Balazsi et al (2008) developed NO_2 gas sensors by embedding a low amount of metal decorated carbon nanotubes into the hex-WO_3 matrix. First, the nanotubes were modified with Au or Ag nanoclusters to improve the NO_2 sensitivity by thermally evaporating gold or silver atoms onto the MWCNTs surface from a gold or silver wire, respectively. Then, MWCNTs decorated with the metallic nanoclusters were dissolved in glycerol and an exact amount of hex-WO_3 nanopowder was added to obtain the desired proportions of CNT/WO_3. Finally, the resulting paste was dropped onto the micro-machined silicon membranes, where the deposited films were dried at 170 ^oC for 1 h and finally annealed at 400 ^oC for 2 h. So, the fabrication of the sensor was completed. The WO_3/MWCNTs hybrid sensors were sensitive to NO_2 gas at room temperature, while the sensitivity of hex-WO_3 to NO_2 was in the temperature range between 150 ^oC and 250 ^oC (Balazsi et al, 2008). Similarly, a CNT-WO_3 hybrid microsensor was prepared by Hashishin and Tamaki (2008) in a a bit more complex way. Firstly, the microgap electrodes made of Au with various gap sizes were fabricated by means of MEMS techniques on a SiO_2 substrate. Second, Ni, catalyst for CNTs growth, was deposited on Au electrode and the Ni-deposited substrate was subsequently set on the electric furnace, where CNTs were grown on the microgap at 700 ^oC for 60 minutes from the nickel growth catalyst under gas mixture of ethanol, argon, and hydrogen. Finally, a microdrop of H_2WO_4 suspension was directly dropped on the surface of CNTs grown between Au electrodes by using microinjection, dried, and calcined at 400 ^oC for 3 h under Ar flow to prevent oxidation of CNTs. As a result, conductivity-type gas sensor based on carbon nanotubes CNTs-WO_3 hybrid showed fairly good sensor response to dilute NO_2, while the sensor fabricated from only CNT exhibited almost no response

(Hashishin and Tamaki, 2008). Lately, WO_3/MWCNT-TiO_2 hybrid composites were prepared using a modified sol-gel method, where the hybrid showed efficient charge separation during UV irradiation for methylene blue decomposition (Lei et al, 2011).

2.3 W - Mn Matrix Composite System

Since W - Mn matrix composite system has not been studied yet in the literature, comprehensive information about tungsten, its alloys as well as composites and their production routes will be discussed in this chapter, which will give the reader a better understanding about the technology and processing of W-based materials. In addition, literature about the investigations on similar W-based systems will provide a better opportunity to analyze and compare the results of this dissertation work with existing systems.

2.3.1 Tungsten, its alloys and composites

Among all the refractory metals, tungsten possesses excellent characteristics like good high temperature strength and stiffness, high elastic modulus, good corrosion resistance, high resistance of thermal shock and low coefficient of thermal expansion (Song et al, 2002a). These great properties have made tungsten an attractive material for many important applications (Song et al, 2003a). Some properties of tungsten are given in Table 2.7.

Table 2.7 : Some properties of tungsten, adapted from Lassner and Schubert (1999).

Period	6
Atomic Number	74
Atomic Mass	183.85 g/mol
Electronegativity	1.7
Space Group	Im3m
Lattice Parameter	3.16524 A^o
Density	19.25 g/cm^3
Melting Point	3422 ^{o}C
Boiling Point	5663 ^{o}C
Specific Heat	0.0317 cal/gK
CTE	4.32-4.68x10^{-6} K^{-1} (25 ^{o}C)
Tensile Strength	172.4 MPa
Young's Modulus	390-410 GPa
Shear Modulus	156-177 GPa
Bulk Modulus	305-310 GPa
Poisson' Ratio	0.28-0.30
Hardness	350-450 kg/mm^2

Until recently, most of the tungsten used in aerospace applications has been in the unalloyed form, because it was much easier and less expensive to produce and fabricate. Moreover, it was found that, particularly at temperatures above 2200 °C, the strengthening effects of many alloying components diminish excessively (Lassner and Schubert, 1999). So, in this last decade, tungsten (W) and its alloys have received attention with a view of improving the high temperature mechanical properties (Song et al, 2002a). Although a large number of tungsten alloys and composites were studied in the past, only some of them achieved commercial significance (Lassner and Schubert, 1999).

Actually, before and around 1920, tungsten was only important as a steel alloying element and as a filament in incandescent lamps. In 1935, the first tungsten heavy metal alloys (WHAs) were produced as a material group of growing importance that would continue for the next four decades and by 1940, tungsten and its alloys and compounds already had widespread application (Lassner and Schubert, 1999). Today, tungsten and tungsten alloys dominate the market in applications where high-density materials are required, such as kinetic energy penetrators, counterweights, flywheels, anti-vibration holders and armor pierces (Öveçoğlu et al, 1996; Lassner and Schubert, 1999). Other applications include radiation shields and x-ray targets. Furthermore, it is used extensively for lighting, electronic devices, and thermocouples in wire form (anonymous, 2011a; Lassner and Schubert, 1999). Moreover, the high melting point of tungsten makes it an obvious choice for structural applications exposed to very high temperatures (Song et al, 2003a). Tungsten is used also at lower temperatures for applications that can use its high elastic modulus, density, or shielding characteristics to benefit (Lassner and Schubert, 1999).

Today, tungsten is mainly used as tungsten carbide (WC) in cemented carbides, such as WC-Co and WC-Co-TiC (anonymous, 2011b; Acchar et al, 2004; Zhang et al, 2003), and as metallic W in alloys, such as in Stellite alloys (Co-Cr-W), in superalloys (anonymous, 2011c), in WHAs (Ryu and Hong, 2003; Lassner and Schubert, 1999), in tantalum-tungsten, niobium-tungsten (anonymous, 2011c) and rhenium-tungsten (Park, 1993) alloys to contribute to their special properties, like creep resistance, wear resistance and high temperature strength.

About 65% of tungsten consumption is in the form of tungsten carbide (Lassner and Schubert, 1999), which is used in cutting and wear applications when combined generally with cobalt as a binder to form the so-called cemented carbides (cermets) because of their high hardness, good wear resistance, good fracture resistance and high temperature strength (Zhang et al, 2003). Cemented carbides such as WC-Co and WC-Co-TiC are the most commonly benefited material in metalworking applications and in order to improve the microstructure and mechanical properties of these materials, a significant amount of research endeavour has been set to develop alternative cemented carbide systems (Acchar et al, 2004). Most of the carbides used in cermets possess high hardness, good electrical and thermal conductivity and high stability. However, the brittleness of these materials resulting from high hardness has limited their solo use in structural applications where they are exposed to high stresses and, so, metal-bonded composites (cemented carbides or cermets) have been developed (anonymous, 2011b).

Other than cemented carbides, tungsten is also consumed with different alloying additions, where Re is one of the most important alloying elements for tungsten. Re additions increase the ductility at low temperatures as well as improve the high temperature strength and plasticity of tungsten metal. In addition to these, additions of Re stabilize the grain structure, increase the recrystallization temperature and improve the welding ability of tungsten (Lassner and Schubert, 1999). It also enhances the corrosion resistance of tungsten (Park, 1993). Furthermore, W-Re alloys strengthened with HfC are the strongest man-made metallic materials at temperatures above 2000 K (Park, 1993; Lassner and Schubert, 1999). On the other hand, tungsten is often used as an additive to tantalum (max. 10 wt.% W) and niobium (max. 15 wt.% W) to increase the high-temperature strength and creep resistance, where the good corrosion resistance and high elasticity of tantalum is combined with the better high temperature strength of tungsten (Taylor et al, 1971; anonymous, 2011c). Furthermore, Stellites, i.e. Co-Cr-W alloys, (Mo, Ni, Fe, C, Si and B can also be contained) are used for applications where high wear resistance is required, such as bearings, valve seats and pistons (anonymous, 2011c). They are employed via hard facing, powder spraying, or as massive forms produced by casting (Lassner and Schubert, 1999). Stellite metal cutting tools exhibit such properties laid in the middle between those of high speed steels and cemented carbides (Lassner and

Schubert, 1999; anonymous, 2011c). In addition, tungsten-titanium alloys are used as sputtering targets in the manufacture of microelectronics devices (Lassner and Schubert, 1999).

Another group of tungsten alloys are Superalloys, which are nickel, cobalt or iron based alloys with high contents of tungsten, molybdenum, tantalum and, more recently, also rhenium (anonymous, 2011c). They have important properties like good oxidation resistance, excellent hot corrosion resistance, high creep strength at high temperature, high thermal fatigue resistance, high-temperature strength, air melting and air/argon remelting capability, good welding properties and ease of casting (Lassner and Schubert, 1999). Use of tungsten causes solid solution strengthening, strengthening by formation of intermetallic compounds such as Co_3W, and formation of carbides. Superalloys are used in aircraft engines, marine vehicles, and stationary power units as turbine blades and vanes, exhaust gas assemblies, burner liners and also as construction material for furnace parts (Donachie and Donachie, 2002).

Tungsten heavy-alloys (WHAs) are probably the most important alloys of tungsten. A typical WHA contains 90 to 98 wt.% W in combination with some mix of nickel, iron, copper, and/or cobalt (Ryu and Hong, 2003). As a result, the tungsten phase contributes to WHAs basic properties providing both high density and high elastic stiffness (Lassner and Schubert, 1999). Ni-Fe or Ni-Cu serves as the ductile binder phase for the brittle W grains. These alloys are characterized by a unique combination of high density (17-19 g/cm^3), high strength and ductility (anonymous, 2011c). Currently, WHAs are used in various applications like radiation shielding, radio isotope containers for cancer therapy devices, damping weights for computer disk drive heads, balancing weights for ailerons in commercial aircraft, helicopter rotors, and for guided missiles, weight distribution adjustment in sailboats and race cars, kinetic energy penetrators for defeating heavy armour, fragmentation warheads (Lassner and Schubert, 1999; Ryu and Hong, 2003; anonymous, 2011c). The choice of alloy composition depends on several parameters. The primary consideration is the density required by the given application. Other factors include mechanical properties, corrosion resistance, magnetic properties and post-sinter heat treatment options (Lassner and Schubert, 1999). The mechanical properties of WHAs can be enhanced through refinement of their microstructures (Ryu et al, 2000), which is

achieved by alloying with Re and Mo, solid state sintering and mechanical alloying (Ryu and Hong, 2003). For instance, Öveçoğlu et al (1996) reported that high-energy ball milling in both planetary ball mill and attritor mill increased the density and improved the sintering characteristics of 90W-7Ni-3Fe heavy alloys even at low sintering temperatures of 1450 ^{o}C.

The first WHA developed was a W-Ni-Cu alloy, which is still used today, particularly for applications in which no magnetism and high electrical conductivity are required (anonymous, 2011f; Lassner and Schubert, 1999). Otherwise, W-Ni-Cu alloys exhibit moderate corrosion resistance and lower mechanical properties than the W-Ni-Fe alloys which are standardly used in industry (Lassner and Schubert, 1999).

Among different WHAs, W-Ni-Fe system satisfies the majority of current uses. Alloys with compositions like 93W-4.9Ni-2.lFe and 95W-4Ni-lFe are used commonly. Moreover, different compositions like 90W-7Ni-3Fe can be also employed via high energy ball milling to benefit relatively low sintering temperatures (Öveçoğlu et al, 1996). The addition of cobalt to a W-Ni-Fe alloy causes slight enhancement of both strength and ductility of the alloy because the presence of cobalt creates solid-solution strengthening of the binder and slightly improves tungsten-binder interfacial strength. Cobalt additions of 5-15 wt.% of the apparent binder phase is most commonly used (Lassner and Schubert, 1999).

For challenging applications, even higher mechanical properties can be obtained from the W-Ni-Co system, where nickel-to-cobalt ratios vary from 2 up to 9%. However, these alloys require quenching because intermetallics (Co_3W and others) form extensively on cool down from sintering (anonymous, 2011c; Lassner and Schubert, 1999). Moreover, W-Ni-Mn heavy alloys have been developed to decrease the sintering temperatures and improve the penetration properties of the WHAs (Bose et al, 1991; Bose et al, 1992; Hong et al, 1997; Zaharee et al 2008).

In addition to these, a few special WHAs are also known. The W-Mo-Ni-Fe quaternary alloys are such special alloys, in which molybdenum restricts tungsten dissolution and spheroid growth resulting in higher strengths (but reduced ductility) in the as-sintered product (Lassner and Schubert, 1999).

Tungsten-copper (W-Cu) and tungsten-silver (W-Ag) composites are widely used in mechanical and electrical engineering. They combine the high hardness, high temperature strength, and wear resistance of tungsten with the outstanding electrical and thermal conductivity of the two high-conductivity metals (Kim et al, 1998; Lassner and Schubert, 1999). Furthermore tungsten increases the resistance of the materials against spark and arc erosion (burn-off) and lowers the sticking and welding tendency. W-Cu and W-Ag systems are neither composites nor real alloys in the strict meaning of the word, because the mutual solubility of the components is practically zero. Therefore, they are also sometimes called pseudoalloys (Lassner and Schubert, 1999). In the recent years, especially W-Cu systems have gained great importance in the automotive, electrical and military industry, because of their high thermal conductivity, low thermal expansions, high wear resistance and excellent electrical conductivity (Roosta et al, in press).

Beside these alloys, there are tungsten dispersion-strengthened and precipitation hardened composites (Chen et al, 2000; Mabuchi et al, 1997; Ryu and Hong, 2003; Song et al, 2003b). As dispersion strengtheners, refractory carbide, nitride and oxide phases, such as TiC, ZrC, HfC, TiN, Y_2O_3, La_2O_3, Sm_2O_3, ThO_2, ZrO_2, etc. have been mainly used to improve the mechanical properties of tungsten and its alloys (Song et al, 2002a; Song et al, 2003a). The most common one is the W-ThO_2 alloy which contains 1 to 2 wt.% thorium. The thorium dispersion improves the starting characteristics of gas tungsten arc welding electrodes by enhancing the thermionic electron emission. It also increases the efficiency of electron discharge tubes and imparts creep strength to wire at temperatures above one-half the absolute melting point of tungsten (Mabuchi et al, 1997; Lassner and Schubert, 1999; Chen et al, 2000). However, it is desirable to replace ThO_2 with non-radioactive activators because of the radioactive contamination of thorium during fabrication, service or handling (Coşkun and Öveçoğlu, 2011). In the last decade, considerable efforts have been directed to develop new materials, especially to explore new activators. It has been found that tungsten electrodes activated with rare-earth metal oxides (such as La_2O_3, Y_2O_3, CeO_2, etc.) exhibit superior arc characteristics compared to pure W and W-ThO_2 electrodes (Chen et al, 2000). Particularly, W-La_2O_3 composites exhibit good mechanical properties and have no radioactive potential (Mabuchi et al, 1997). Furthermore, there are studies about strengthening the WHAs by adding Y_2O_3. As a

result, the strength of WHAs are improved with decreasing particle size which is proportional to the Y_2O_3 content (Ryu and Hong, 2003). Moreover, Itoh and Ishiwata (1996) and Kim et al (2006b) stated that the additions of Y_2O_3 particles improve the densification of W powders and high strength at room and high temperature. Unlike other oxide dispersion strengthened (ODS) composites, W-Y_2O_3 has excellent corrosion resistance against the molten metal (Itoh and Ishiwata, 1996). Recently, Genç et al (2010) used Y_2O_3 particles as doping agents in W-Ni composites, where they achieved a slight particle size reduction and considerably high relative densities and hardness values compared to the literature. On the other hand, hafnium carbide (HfC) is the strongest reinforcement for tungsten at elevated temperatures. The outstanding strength of HfC is coming from its high thermodynamic stability and its comparatively low solubility and diffusivity in tungsten at high temperatures (Park, 1993; Lassner and Schubert, 1999). There are also other carbides, such as TaC, NbC, ZrC and TiC used as dispersoids (Lassner and Schubert, 1999). Recently, mechanical and thermophysical and ablation properties of TiC/W and ZrC/W composites at elevated temperatures were studied. As a result, it is proved that both of them possess excellent high temperature strength and good thermophysical properties, which make them good candidates for high temperature applications (Song et al, 2002a; Song et al, 2003a; Song et al, 2003b). Lately, Coşkun et al (2009) and Coşkun and Öveçoğlu (2011) studied W-SiC-Y_2O_3 and W-SiC composite systems, respectively, where they obtained very promising relative density and microhardness results. Moreover, W-Ni composites reinforced with TiC were investigated and high microhardness as well as relative density values were obtained by different researchers (Coşkun et al, 2009; Genç et al, 2010a; Genç et al, 2010b).

Finally, beside the fact that the amount of publications about the effect of Mn on various properties of W heavy alloys is very limited (Bose et al, 1991; Bose et al, 1992; Hong et al, 1997; Zaharee et al 2008), there is no information in the literature on the effects of Mn addition to the properties of W itself. Even, there is no published phase diagram available for W - Mn binary system. Moreover, there is not any data about W-VC systems in the literature either, although VC, which has excellent high temperature strength, high chemical and thermal stability at high temperatures, high melting temperature (2830 ^{o}C) and high hardness (Pierson, 1996), is mainly used in WC-Co hard metals as a grain growth inhibitor (Choi et al, 2000;

Luyckx et al, 1996; Lin et al, 2004; Lee et al, 2003). So, one of the aims of the present dissertation work will be to fulfill these two gaps by investigating W - Mn matrix composite system.

2.3.2 Production of tungsten, its alloys and composites

Several processing routes can be used in the production of W-based alloys and composites, which are as swaging, hot explosive consolidation, arc casting, electron beam melting, chemical vapor deposition, hot extrusion and powder metallurgy (P/M) techniques (Chattopadhyay, 2003; Lassner and Schubert, 1999)

However, it is very difficult to fabricate tungsten because of its high melting point and low ductility (Li and German, 1983; Lassner and Schubert, 1999). Fabrication of bulk W requires very high sintering temperatures up to 2400-2800 ^{o}C to achieve a nearly fully dense structure (Li and German, 1983). In order to reduce the sintering temperature, W with various additions produced via different production techniques, such as liquid-phase sintering (Kemp and German, 1991; Yoon et al, 2002; Ryu and Hong, 2003; Chan and Lin, 1998; Ryu et al 1997; German et al, 2009), solid-state sintering (Song et al, 2002a; Song et al, 2002b; Song et al, 2003a; Song et al, 2003b; Avettand-Fenoel et al, 2003; Ryu et al, 2000) and activated sintering (Li and German, 1983; German and Munir, 1976; Vacek, 1959; Hayden and Brophy, 1963; Samsonov and Yakolev, 1967; Toth and Lockington, 1967; Corti, 1986; Samsonov and Yokolev, 1969; German and Munir, 1982; Panichkina, 1967) have been the subject of several reported investigations.

In recent years, utilizing powder metallurgy and advanced sintering techniques such as hot isostatic pressing (HIP), fabrication of fully dense W composites has become possible at much lower temperatures (~1350 ^{o}C) than the melting point of W (Ishijima et al, 2005; Kurishita et al, 2008; Kurishita et al, 2009). On the other hand, activated sintering, which is carried out below the melting point activating agent, involves small additions of some transition metals such as Pd, Pt, Ni, Co and Fe and provides considerable reductions in the sintering temperature of W even when the conventional sintering techniques are used (Li and German, 1983; Vacek, 1959; Hayden and Brophy, 1963; Toth and Lockington, 1967; Samsonov and Yakovlec, 1967; German and Munir, 1976; Samsonov and Yakovlev, 1969; German and Munir,

1982; Panichkina, 1967; Corti, 1986). In Figure 2.9, effects of different activators to tungsten activation is shown.

As clearly seen in the Figure 2.9, the best activators for tungsten metal are Pd and Ni. The reason for the platinum group metals being such effective activators for the sintering of tungsten is considered to be linked to their relatively high solubility for tungsten and their low solubility in tungsten (Corti, 1986). For instance, Ni dissolves up to 38 wt% W in its solid solution and the solubility of W into Ni is only about 0.1 wt% which is negligible (Genç et al, 2010c). Moreover, the volume diffusion of W into Ni is rather more rapid than that of Ni into W (Panichkina, 1967).

There are several reported models that explain the mechanism of activated sintering. Hayden and Brophy (1963) described a supporting phase idea, in which activating agent forms a layer on the tungsten particle surface followed by the diffusion of tungsten atoms through the supporting phase-W particle interface. Subsequently, Toth and Lockington (1967) tried to explain the mechanism of activated sintering by the dissolution of tungsten at the activator-tungsten interface, which enhances the volume diffusion and surface diffusion through the activator layer. Later, German and Munir (1982) reported that the activator layer improves the grain boundary diffusion by wetting the inter-particle grain boundary. On the other hand, Samsonov and Yakovlev (1967) related the activated sintering with the electron structure of the activators and tungsten, where W acts as an electron donor and increased number of the stable d-bonds in the system lowers the free energy and activates the sintering process.

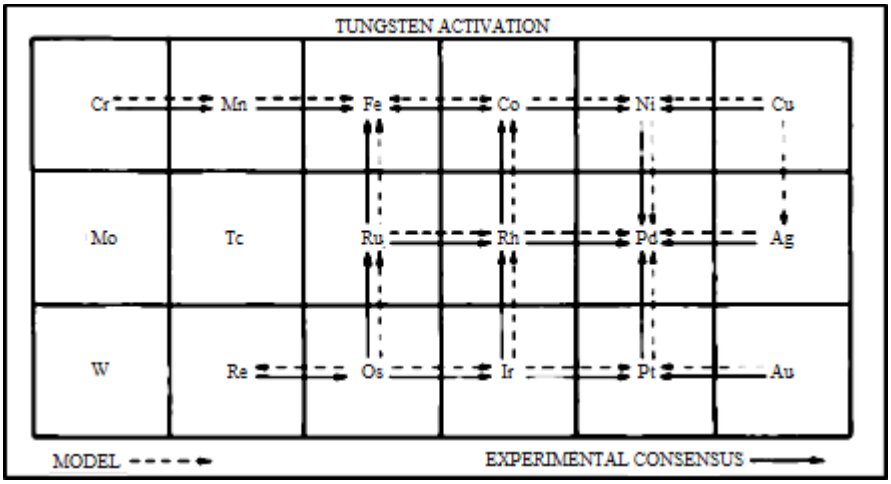

Figure 2.9 : Tungsten activation; the position of the activator in the Periodic Table affects the densification of tungsten, adapted from Corti (1986).

All these physical models concerning to activating layers remained as a phenomenon for a long time due to the lack of observation to understand their morphology, structure, and chemistry (Luo et al, 1999). Finally, Luo et al (2005) revealed the existence of nanometer-thick, Ni-enriched, liquid-like (disordered) grain boundary layers in W-Ni binary metallic system at a temperature of 1400 ^{o}C which is well below the eutectic temperature (1495 ^{o}C) of W-Ni. So, the mechanism of solid-state activated sintering is explained by the enhanced diffusion in nanoscale impurity-based, quasi-liquid, interfacial films through experiments and thermodynamic modeling studies (Luo et al, 2005; Shi and Luo, 2009).

Different than activated sintering, liquid phase sintering (LPS) is a process in fabricating high performance, multiple-phase components from powders which involve sintering under conditions where solid grains coexist with a wetting liquid (German et al, 2009). Microstructural changes quickly occur in LPS because of fast material transport through liquid. When a liquid phase forms during heating, it flows into the fine vacancies between the particles because of the capillary effect and the solid particles may be redistributed with this liquid flow, which is referred to as particle rearrangement (Kang, 2005; German et al, 2009). There are two types of LPS, namely persistent LPS and transient LPS. In persistent LPS, the liquid phase persists throughout high-temperature portion of the sintering cycle, while the liquid phase in transient LPS disappears during sintering cycle due to the dissolution into the solid or formation of new phase (German et al, 2009).

Tungsten heavy alloys (WHAs) are manufactured by a powder metallurgical process employing a liquid-phase sintering at a temperature above 1450 ^{o}C(German et al, 2009; Ryu and Hong, 2003; Bose et al, 1991). Similarly, tungsten-copper (W-Cu) composite materials are produced via LPS at temperatures between 1250 ^{o}C and 1400 ^{o}C, where powder mixtures contain min. 10-15 wt.% Cu (Kim et al, 1998; Johnson and German, 1994; Dore et al, 2004; Ibrahim et al, 2009). Moreover, in systems such as W-Cu which have low mutual solubility, there is little sintering due to chemical gradients prior to liquid formation. So, usually about 30 vol.% liquid is sufficient to give complete densification by rearrangement (German et al, 2009). In addition to these, W-Ni-Mn heavy alloys can be manufactured via LPS at sintering temperatures between 1100 ^{o}C-1500 ^{o}C (Bose et al, 1991; Bose et al, 1992; Hong et al, 1997; Zaharee et al 2008). On the other hand, activated sintering of tungsten and

its alloys and composites is generally carried out at temperatures around 1400 ^{o}C depending on the activating agent used (Li and German, 1983; German and Munir, 1976; Vacek, 1959; Hayden and Brophy, 1963; Samsonov and Yakolev, 1967; Toth and Lockington, 1967; Corti, 1986; Samsonov and Yokolev, 1969; German and Munir, 1982; Panichkina, 1967). Finally, Coşkun et al (2009) and Coşkun and Öveçoğlu (2011) sintered W-SiC and W-SiC-Y_2O_3 composites via conventional solid-state sintering at a relatively low temperature of 1680 ^{o}C without using any liquid phase or activating agent.

3. EXPERIMENTAL PROCEDURE

The experimental procedure section of this dissertation work provides useful information and insight regarding the synthesis routes of three tungsten-based systems and their characterization.

First part will deal with the production of tungsten borides and their purification and characterization studies. Secondly, the production route of tungsten oxide nanoparticles, nanorods, nanowires and preparation of carbon nanotubes (CNTs) will be explained as well as the coating of CNTs with tungsten oxide nanoparticles and pertaining characterization investigations will be detailed. Thirdly, the production method and characterization of W-Mn alloy and W-Mn-X composite powders and their sintered counterparts will be explained.

3.1 Tungsten Boride System

3.1.1 Production of tungsten borides

In this study, $WO_{2.72}$ (99.99% purity, Alfa Aesar™), B_2O_3 (99.999% purity, Alfa Aesar™) and Mg (+99% purity, Alfa Aesar™) powders were used. These powders were mixed to form powder batches according to the metallothermic reduction of $WO_{2.72}$ and B_2O_3 with Mg to constitute W_2B_5 + MgO and WB + MgO as final products as shown in reactions (3.1) and (3.2). For mechanical alloying experiments, 10 g of samples were prepared.

$$2WO_{2.72}(s) + 2.5B_2O_3(s) + 12.94Mg(s) = W_2B_5(s) + 12.94MgO(s) \quad \textbf{(3.1)}$$

$$2WO_{2.72}(s) + B_2O_3(s) + 8.44Mg(s) = 2WB(s) + 8.44MgO(s) \quad \textbf{(3.2)}$$

In all experiments, stoichiometric excess (about 10 wt.%) amount of reducing agent Mg was used to account for the surface oxidation of the metal and the residual oxygen that could be absorbed onto reactant surfaces and milling medium. Moreover, for synthesis of WB powders, 30 wt.%, 50 wt.% and 100 wt.% excess of B_2O_3 powders were used, while 50 wt.% and 100 wt.% excess of B_2O_3 were used in W_2B_5

production along with stoichiometric amounts. Furthermore, in any process for the formation of W_xB_y, it would be necessary to ensure that all of the tungsten oxide is consumed by reaction because tungsten oxide is difficult to remove by dissolution in HCl. This could be achieved by using a stoichiometric excess of both Mg and B_2O_3 in any process and any excess of these phases would remain once the tungsten oxide had been consumed and be dissolved along with the MgO product.

The prepared powder blends were mechanically alloyed (MA'd) in a stainless steel vial using a 8000D Spex™ mill with a speed of 1200 rpm. Stainless steel balls with a diameter of 6.25 mm (1/4 inches) were used as milling media and the ball-to-powder weight ratio was 10:1. Milling durations of the powders varied up to max. 30 h. High-purity argon was chosen as the milling atmosphere to prevent oxidation and contamination of the powder because the presence of air in the vial causes to produce oxides and nitrides in the powder, especially if the powders are reactive in nature. Thus, the loading and unloading of the powders into the vial was carried out inside a Plas-Labs™ atmosphere-controlled glove box. After mechanical alloying of the powders, leaching experiments were carried out to remove MgO and all other contamination from the milling medium and impurities under continuous ultrasonication. 3.6 M, 5 M and 7 M HCl were used as the leaching solution. Leaching duration and solid-to-liquid ratio of the leaching solution were set to 15 min and 1:10, respectively. Concentration of the leaching solutions was determined as shown below;

HCl solution contains 37 wt% HCl in water and HCl has a molecular weight of 36.46 g/mol.

$$\text{Molarity of HCl solution} = \frac{1\,\text{mol}}{36.46\,\text{g}} \cdot \frac{37\,\text{g}}{100\,\text{g}} \cdot \frac{1.19\,\text{g}}{1\,\text{ml}} \cdot \frac{1000\,\text{ml}}{1\,\text{L}} = 12.076\,\text{mol/L} \qquad \textbf{(3.4)}$$

According to this calculation, 1/12.076 = 0.083 L = 83 ml of HCl was mixed with 917 ml of distilled water in order to prepare 1L of 1M HCl (Bilgi, 2007).

After that, solutions were centrifuged in a Hettich™ Zentrifugen Rotofix 32 A device for 15 min with a rotation speed of 3500 rpm, diluted and again centrifuged for another 15 min. Finally, the solution was vacuum filtered, washed in ethanol as well as in distilled water for several times and obtained powders were dried in air at 80 ^{o}C for 12 h. All leaching experiments were carried out at room temperature.

Following the leaching of the products, molar yield of produced W_xB_y was calculated according to equation given below:

$$\text{Molar Yield} = \frac{\text{Weight of the leached sample}}{\text{Weight of the unleached sample} \cdot \text{weight fraction of } W_x B_y} \cdot 100 \qquad \textbf{(3.5)}$$

The weight fractions of W_2B_5 and WB were calculated as 0.422 and 0.503, respectively, in the unleached sample with the stoichiometry of equations (3.1) and (3.2).

3.1.2 Characterization studies on tungsten borides

Microstructural characterization of the leached and unleached powders were carried out in a Jeol™-JSM-T330 scanning electron microscope (SEM) coupled with Energy Dispersive X-Ray Spectrometer (EDS) and in a Bruker™ X-Ray Diffractometer (XRD) (CuK_α radiation, 40 kV and 40 mA, $\lambda = 0.154$ nm). TOPAS 3 (Bruker AXS) software was used to estimate crystallite sizes by the modified Scherrer's formula (Suryanarayana and Norton, 1998) based on the broadening of XRD diffraction peaks:

$$B_r = \frac{k\lambda}{L \cdot \cos\theta} + \eta \qquad \textbf{(3.6)}$$

where B_r is the total broadening due to reduction in crystallite size and lattice strains, λ the X-ray wavelength, L the crystallite size, η the strain in the material, k a constant and θ the diffraction angle. A Malvern™ Mastersizer Laser particle size analyzer was used to carry out the powder particle size measurements. DSC experiments of the powders were carried out in a TA™ SDT Q600 DTA-DSC-TG device under Ar with a heating rate of 10 ^oC/min at 1000 ^oC. Moreover, atomic absorption spectroscopy (AAS) experiments were carried out in a Perkin Elmer™ AAnalyst 800 device to determine the presence of Fe, W and Mg metals in the leach solution after the leaching process to understand whether the leaching process succeeded or not.

3.2 Tungsten Oxide System

3.2.1 Production of tungsten oxide nanoparticles

For the typical production route, ~200 mg of tungsten (VI) chloride (WCl_6) (+99.9% purity, Fisher™ Scientific) powders were added to distilled water to prepare a 0.01 M aqueous solution. After some amount of sonication, an excess amount (~100 mg) of sodium borohydride ($NaBH_4$) powders (+98% purity, Fischer™ Scientific) were added to the solution under continuous sonication in a Decon™ FS 200B Ultrasonic bath (240 V, 3 A, 50 Hz). As soon as $NaBH_4$ was added, the color of the solution was suddenly changed to black/dark brown and vigorous evolution of gas was observed. The synthesis is based on the following chemical reaction:

$$WCl_6(s) + 1.5NaBH_4(s) + 2\,H_2O(l) = WO_2(s) + 1.5NaCl(aq) + 1.5BCl_3(g) + 5H_2(g) \quad \textbf{(3.7)}$$

After 3 h of sonication, the solution was vacuum filtered and obtained powders were washed in ethanol and distilled water for several times then dried in air at room temperature. Since sodium chloride (NaCl), which is the by-product of the reaction, was already dissolved in water, there was not any additional treatment needed to remove it. The yield of the process is around 90%. The schematic of the production route is given in Figure 3.1. Finally, to obtain fully crystallized nanopowders, the sample was annealed at 500 ^{o}C for 2 h. The details of the annealing process is given in the next section.

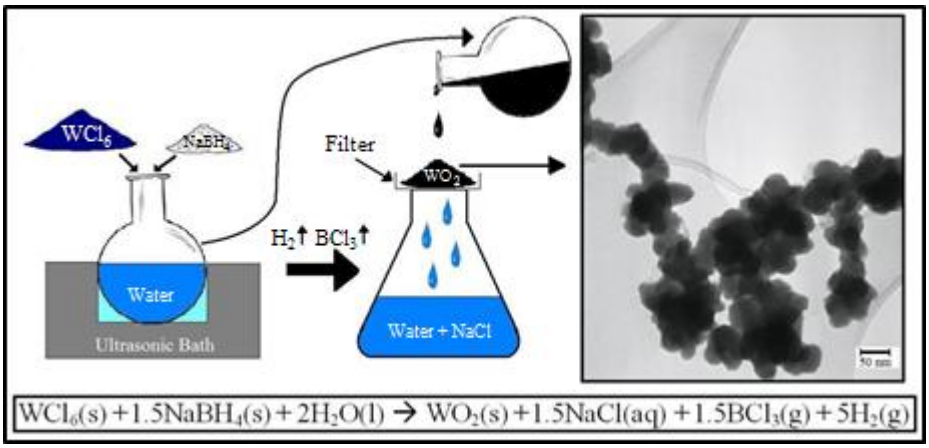

Figure 3.1 : The schematic of the WO_2 nanoparticle production route and a representative TEM picture showing WO_2 nanoparticles.

For the knowledge of the prospective researchers, it is significant to mention that several other experiments by changing the parameters of the process were also

carried out. These included experiments with different WCl_6 concentrations or $NaBH_4$ amounts, process temperatures other than room temperature (0 ^oC and 50 ^oC), and various type and amount of solutions (ethanol, acetone or mixture of them). Stirring instead of sonication were also employed. In addition to these, some of the products were also heat-treated in an autoclave. However, these changes in process parameters mostly led to different end products with either different morphologies or different crystal structures. Thus, the details of these additional attempts, which were out of the scope of the present dissertation work, were not further discussed.

3.2.2 Production of tungsten oxide nanorods and nanowires

Tungsten oxide nanorods and nanowires were produced by annealing the nanopowders. The annealing process was performed on an alumina (Al_2O_3) boat placed in a quartz reaction tube within a horizontal tube furnace under Ar atmosphere. The flow rate of Ar gas in the furnace was adjusted to be at 1 L/min. An oxygen (O_2) filter was used to avoid the contamination from traces of O_2 present in Ar gas. The O_2 filter contained small copper (Cu) beads and magnesium (Mg) shots in a small quartz tube, which was held at 450 ^oC to make sure that the shots got oxidized during the Ar flow. The annealing temperature was changed between 500 ^oC and 1000 ^oC to observe the effect of temperature on the microstructure and the morphology of the samples. The annealing duration was fixed at 6 h for each temperature; however, some experiments were carried out for shorter times to compare the effect of annealing.

3.2.3 Production of carbon nanotubes

CNTs used in this research were grown by CVD method. Ferrocene (98% purity, Sigma-Aldrich™) was used as the source of iron catalyst and toluene (+99.5% purity, Sigma- Aldrich™) as the primary carbon source. A solution of 4% ferrocene in toluene was prepared and sonicated for 15 min. After that, it was injected with a syringe into the furnace for the CNT growth. The CNTs were grown directly on a quartz reaction tube in a two zone horizontal tube furnace under Ar atmosphere (Fig. 3.2).

The ferrocene/toluene solution was injected at a rate of 5.6 mL/h for 4 h into the first zone of the furnace, which was maintained at a temperature of 180 ^oC. The vaporized

reactants were then purged with Ar gas at a flow rate of 2.4 L/min into the second zone of the furnace, which was maintained at 760 ^{o}C, where ferrocene decomposed to form iron catalyst and subsequent CNT growth occurred. Upon completion of the CNT synthesis, the quartz tube was allowed to cool down. The CNTs were then scraped off from the inside of the tube in a glove box. Yields per batch were ~5-7 g. If there was also a substrate in the tube, directional growth of the CNTs occurred. Generally, in one hour 100 μm of CNTs were growing. To clean the quartz tube, it was heated up to 800 ^{o}C and held for several hours under airflow to burn out the remaining CNTs.

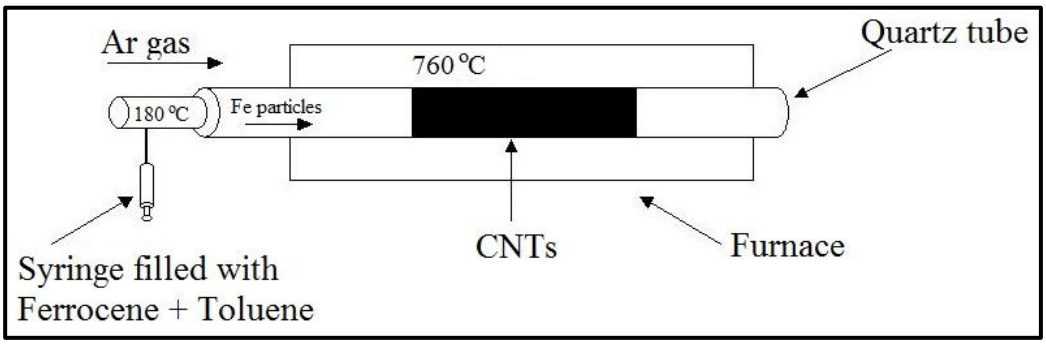

Figure 3.2 : Schematic of the CNT growth set-up.

To functionalize the CNTs, they were placed in a solution of sulphuric acid (H_2SO_4) and nitric acid (HNO_3) with a volume ratio of 3:1. For each batch, 1 g of CNTs and 500 ml acid solution were used and the mixture was sonicated in a round-bottomed glass flask for 12 h at 50 ^{o}C. After functionalization, the solution was vacuum filtered using PTFE filter paper with a pore size of 200 nm and distilled water was added to the CNTs till the solution became neutral. Following filtration, the functionalized CNTs (fCNTs) were dried in a vacuum oven. The simplest way to understand whether the CNTs got functionalized or not is to place them inside a beaker of distilled water and sonicate for several seconds. If the functionalization process were successful, the fCNTs disperse in water the color of the water would become black immediately.

3.2.4 Coating of CNTs with tungsten oxide nanoparticles

Two different routes were used to coat the CNTs. In both routes, 50 mg of CNT were added to the solutions. In the first route, functionalized CNTs were added to different solutions (water or water/ethanol) under continuous sonication. After fCNTs were

dispersed in the solution, WCl_6 and $NaBH_4$ were added under continuous stirring. After several hours of stirring, the solution was vacuum filtered and obtained products were dried in air at room temperature. In the second route, pristine CNTs were used. This time, benzyl alcohol (BA) was used as a surfactant with a final molar ratio of 1:5 (W^{6+}:BA). First, CNTs were mixed with BA. Then, this mixture was added to different solutions (water or water/ethanol) under continuous sonication. After pristine CNTs were dispersed in the solution, WCl_6 and $NaBH_4$ were added under continuous stirring. After several hours of stirring, the solution was vacuum filtered and obtained products were dried in air at room temperature.

3.2.5 Characterization studies on tungsten oxide nanostructures and CNTs

The crystal structures of the tungsten oxide nanostructures and CNTs were examined by X-ray diffraction (XRD) using a Bruker™ D8 X-Ray Diffractometer (XRD) (CuK_α radiation, 40 kV and 40 mA, λ = 0.154 nm). Thermal analysis of the as-prepared tungsten oxide nanopowders was carried out in a Netzsch™ 204 F1 Phoenix® differential scanning calorimeter (DSC) device under Ar atmosphere (30 mL/min) with a heating rate of 20 ^oC/min at 550 ^oC. Microstructural characterizations were carried out by using a Jeol™ 6340F FEG-SEM, a high resolution scanning electron microscopy. For scanning electron microscopy (SEM) analyses, a thin layer of gold was sputtered onto the surface of the samples to reduce any charging effects. Transmission electron microscopy (TEM) and high-resolution TEM (HRTEM) investigations were also used to examine both the micro-and crystal structures of the tungsten oxide and CNT samples using a Jeol™ 2000FX TEM and FEI™ Tecnai F20-G2 FEGTEM.

3.3 W - Mn Matrix Composite System

3.3.1 Production of W - Mn matrix composites

In this study, W (99.9% purity, Alfa Aeasar™), Mn (99.3% purity, Alfa Aesar™), VC (99.0% purity, Alfa Aesar™) and ZrC (99.5% purity, Alfa Aesar™) powders were used. Furthermore, graphite powders (+99% purity, Alfa Aesar™) were used as a process control agent (PCA) to minimize cold welding between powder particles and thereby to inhibit the agglomeration. VC and ZrC used as reinforcement agents were premilled for 24 h and have average particle sizes around 200 nm. First, the W-Mn

matrix was prepared by mechanical alloying (MA) of the powder blends of W - 1 wt.% Mn and W - 3 wt.% Mn for 6 h. After that, premilled VC powders were added and mixed to form powder batches to constitute the composition W - 1 wt.% Mn - 2 wt.% VC (hereafter referred to as W1Mn2VC) and W - 3 wt.% Mn - 2 wt.% VC (hereafter referred to as W3Mn2VC). Finally, powder blends were MA'd together for 3 h, 6 h, 12 h and 24 h. In addition, ZrC powders as reinforcement agents were also added to W-Mn matrix and MA'd together for 6 h and 24 h for comparison. Mechanical alloying experiments were carried out in a tungsten carbide (WC) vial using a 8000D Spex™ mill with a speed of 1200 rpm. WC balls with a diameter of 6.35 mm (¼ inches) were used as the milling media. The ball-to-powder (BPR) weight ratio was 10:1. As in the WB system, the loading and unloading of the powders into the vial was carried out inside a Plas-Labs™ atmosphere-controlled glove box to prevent any oxidation or contamination. Powder consolidation was carried out in a 10 ton capacity APEX™ 3010/4 uniaxial hydraulic press to obtain cylinder type compacts of MA'd W-Mn-X composites with a diameter of 6.36 mm under a uniaxial pressure of 450 MPa. Sintering experiments were carried out in a reductive high temperature 1800 M Vac Graphite Linn™ furnace at 1300 ^{o}C (1573 K) under both inert Ar and reducing H_2 gas flowing conditions for 1 h.

3.3.2 Characterization studies on W - Mn matrix composites

A Malvern™ Mastersizer Laser particle size analyzer was used for powder particle size measurements. Microstructural characterization of as-blended and MA'd powders were accomplished by using a Jeol™-JSM-T330 scanning electron microscope (SEM) and a Bruker™ X-Ray Diffractometer (XRD) (CuK_{α} radiation). Some of the powders were analyzed by high resolution scanning electron microscopy (Jeol™ 6340F FEG-SEM). TOPAS 3 (Bruker AXS) software was used to estimate the crystallite sizes.

Vickers microhardness tests were conducted on the sintered samples using a Shimadzu™ micro-hardness tester under a load of 100 g for 15 seconds. Results of hardness tests were averaged out of 15 successive indentations. Sintered densities were measured by using the Archimedes method. For comparison, W1Mn and W3Mn matrix alloy samples without any VC addition were also investigated. Additionally, the sliding wear experiments of W3Mn2VC samples were conducted

on a Tribotech™ Oscillating Tribotester using 6 mm alumina balls under an applied force of 5 N. The tests were carried out at room temperature in air with a sliding speed of 2 mm/s, 2 mm stroke length and a sliding distance of 12 m. Abraded surfaces were characterized using a Veeco™ Dektak 6 M Stylus Profiler and test results were arithmetic mean of three different measurements for each sample. In addition to these, microhardness, relative densities and sliding wear resistances as well as the fracture surfaces of W3Mn2ZrC composite samples MA'd for 6 h and 24 h were also investigated for comparison.

4. RESULTS AND DISCUSSION

This chapter includes three sections discussing the results obtained during the characterization investigations on the three aforementioned W-based material systems. The first section of this chapter is about the tungsten boride system. A detailed X-ray diffraction (XRD) analysis on the tungsten boride system will be revealed and the advantages as well as the disadvantages of the proposed mechanical alloying route to produce tungsten borides will be discussed. In the second section, results acquired from the morphological and microstructural characterization investigations conducted via XRD, Scanning Electron Microscopy (SEM), Transmission Electron Microscopy (TEM) and High Resolution Transmission Electron Microscopy (HRTEM) techniques on tungsten oxide nanoparticles, nanorods, nanowires as well as CNTs and CNT/tungsten oxide hybrids will be discussed and their potential applications will be proposed. Finally, the third section will reveal the mechanical and microstructural properties of W-Mn matrix composites by discussing the results from XRD and SEM analyses as well as from the density, microhardness and sliding wear measurements. In addition, these results will be compared with those in the literature to discuss the success of the proposed production route for W-Mn matrix composites.

4.1 Tungsten Boride System

This section reveals the results of a detailed X-ray diffraction study on WB + W_2B powder mixtures and ditungsten pentaboride (W_2B_5) powders. These results are discussed in the sense of the proposed production route of the boride powders, which is mechanical alloying followed by leaching and the stoichiometry of the initial powders used in. To prevent any inconvenience, all samples prepared to produce WB + W_2B powder mixtures will hereafter be referred to as WBM, whereas all samples prepared to produce W_2B_5 powders will be referred to as 2W5BM.

4.1.1 Characterization of WB + W_2B powder mixtures

X-ray diffraction (XRD) patterns from as-blended WBM powders and those MA'd for 7 h are shown in Figure 4.1. It is clearly seen that the peak intensities of both $WO_{2.72}$ (Bravais lattice: Simple monoclinic; a = 1.832 nm; b = 0.378 nm; c = 1.403 nm; $\alpha = 90^o$; $\beta = 115.2^o$; $\gamma = 90^o$; Space group: Pnm, ICDD Card No: 36-0101) and Mg (Bravais lattice: Simple hexagonal; a = 0.320 nm; c = 0.521 nm; $\alpha = 90^o$; $\beta = 90^o$; $\gamma = 120^o$; Space group: $P6_3/mm$, ICDD Card No: 35-0821) phases decrease with MA duration, which might indicate some grain refinement and decrease in amount. Moreover, it is evident that after MA for 7 h, the presence of very small amounts W_2B (Bravais lattice: Body-centered tetragonal; a = 0.556 nm; c = 0.474 nm;; Space group: I4/mcm, ICDD Card No: 89-1991) and MgO (Bravais lattice: FCC; a = 0.556 nm; Space group: $Fm\bar{3}m$, ICDD Card No: 71-3631) phases are identified.

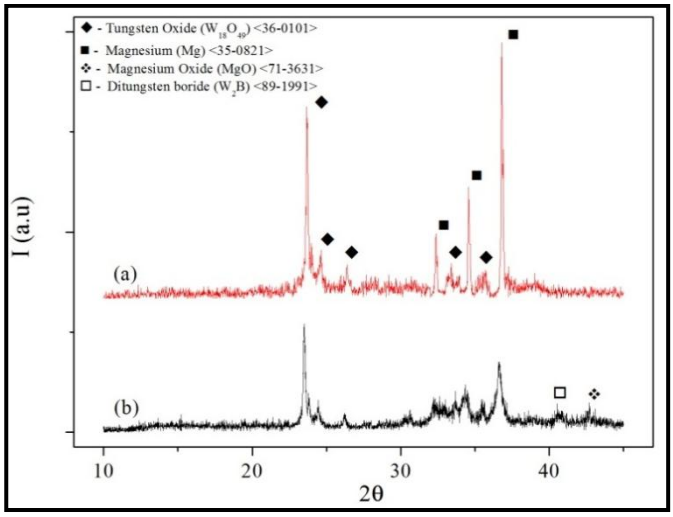

Figure 4.1 : XRD patterns of; a) as-blended powders and b) powder blend MA'd for 7 h.

This result shows that the reaction between $WO_{2.72}$ and Mg has just started, however the MA duration is far from sufficient to produce any WB. As a result, MA duration was increased up to 30 h. During these experiments, a crust formation on the walls of the stainless steel vial was observed. Only ~10% of the sample was in the form of loose powders and the rest was kept in this crust. The crust was broken into pieces using a screwdriver and hammer and grinded in an agate mortar to render it in powder form. During this operation, the most important thing was to retrieve maximum amount of powders without damaging the vial, which was very tedious

and time consuming. Figure 4.2 shows the XRD patterns of loose powders in the WBM samples MA'd for 15 h, 20 h and 30 h.

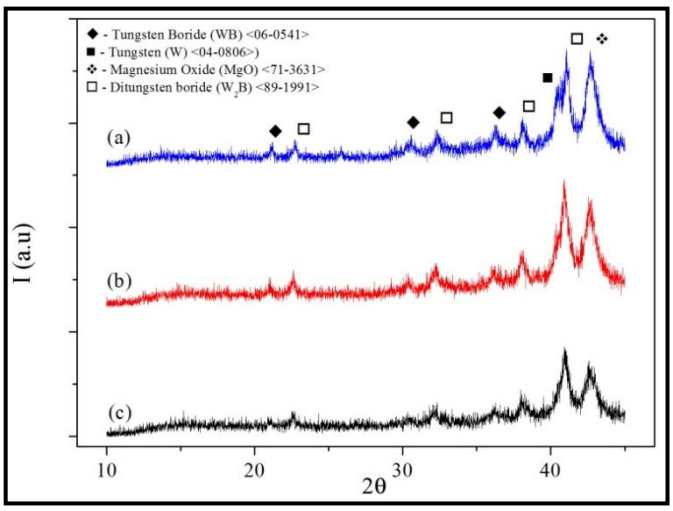

Figure 4.2 : XRD patterns of loose powders in the WBM sample MA'd for; a) 15 h, b) 20 h and c) 30 h.

As seen in the Fig. 4.2, the peaks of W (Bravais lattice: BCC; a = 0.316 nm; Space group: Im$\bar{3}$m, ICDD Card No: 04-0806), WB (Bravais lattice: Base-centered orthorhombic; a = 0.319 nm; b = 0.840; c = 0.307 nm; Space group: Cmcm, ICDD Card No: 06-0541), W_2B and MgO are identified in all WBM samples. Furthermore, it is also clear that with increasing amount of MA, peaks are broadened and peak heights decreased as a result of grain refinement and an increase in internal strain due to mechanical alloying. It can be seen that W_2B instead of WB is the major boride phase when the peak intensities are considered, although the powder blend had an appropriate stoichiometry for the WB synthesis. Moreover, the W_2B-to-WB ratio does not change with MA duration, which is unexpected, because it was considered that increasing amount of MA would give the sufficient energy for WB synthesis. The reason for this might be that the WB is a high temperature phase in W-B binary system (Stubicar et al, 1994). Figure 4.3 shows the XRD patterns of the crust formation in the WBM samples MA'd for 15 h, 20 h and 30 h.

As seen in the Fig. 4.3, the peaks of W, WB, W_2B and MgO are identified in all WBM samples similar to loose powders (Fig. 4.2) in the same samples. Also in these WBM samples, W_2B phase is the major boride phase. Contrary to what evidenced in Fig. 4.2, W_2B-to-WB ratio increases with increasing amount of MA indicating the fact that WB cannot be produced by further increasing MA durations in these

conditions. Moreover, the amount of W decreases with MA duration indicating that more W is consumed to produce borides.

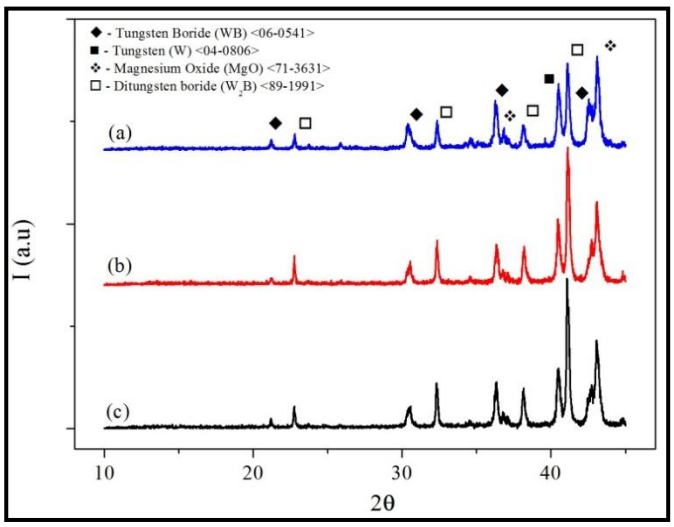

Figure 4.3 : XRD patterns of the crust formations in the WBM samples MA'd for; a) 15 h, b) 20 h and c) 30 h.

Since the loose powders and crusts in WBM samples consist of the same phases, they were ground together in an agate mortar to prepare samples for leaching. Leaching is the process of bringing a solid in contact with an aqueous solvent with the objective of dissolving one or more of the compounds contained in the solid (Arsdale, 1953) resulting in more concentrated desired part of the material (Habashi, 1970). In the present system, 1 g of every sample was leached with HCl (Walker and Tarn, 1991) with the objective of dissolving all components other than borides so as to obtain pure borides. Figure 4.4 shows the XRD patterns of the WBM samples MA'd for 15 h, 20 h and 30 h after leaching with a 3.6 M HCl solution. The 3.6 M HCl solution contains ~1.5 times more HCl than the stoichiometric amount. Leaching with stoichiometric excess amount of acid solution gives a better result compared to leaching with stoichiometric amount (Yazıcı, 2009; Bilgi, 2007). As clearly seen from Fig. 4.4, the peak intensity of MgO phase drastically decreases in the WBM sample MA'd for 15 h after leaching with the 3.6 M HCl solution. It continues to decrease with increasing MA duration. Moreover, it is clearly evident that W cannot be removed from the system after leaching with 3.6 M HCl solution. In addition, the 2θ values for the (200) plane of the MgO phase and the (040) plane of the WB phase overlap, which makes the interpretation harder. However, it can be deduced that the peak around 43° belongs to the WB phase instead of MgO in the WBM samples

MA'd for 20 h and 30 h, when the comparison of theoretical and actual intensity ratios of the peaks corresponding to the (111) and (040) planes of WB phase has been taken into account. Moreover, the fact that this ratio does not seem to change in the WBM sample MA'd for 20 h and 30 h is another point to support this idea. On the other hand, the peak intensities of the WB phase also decrease with increasing MA duration, which gives rise to thought that the WB phase might also be dissolved during leaching. Overall, 0.736 g for the WBM sample MA'd for 15 h, 0.618 g for the WBM sample MA'd for 20 h and 0.559 g for the WBM sample MA'd for 30 h were recovered after leaching.

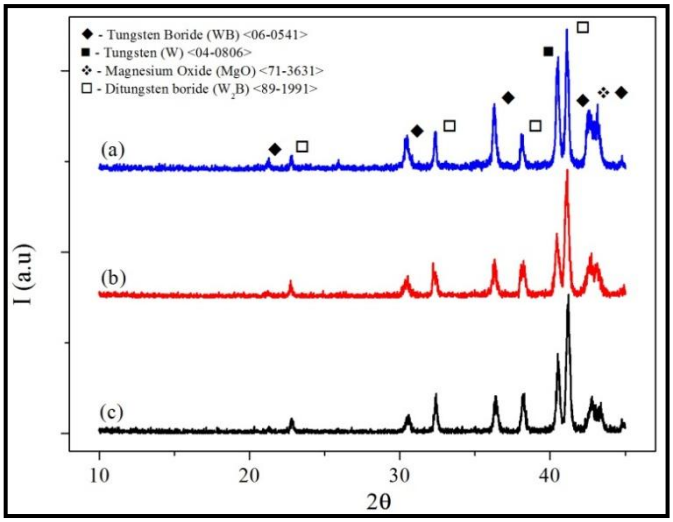

Figure 4.4 : XRD patterns of the WBM samples MA'd for; a) 15 h, b) 20 h and c) 30 h after leaching with 3.6 M HCl solution.

Table 4.1 gives the results of atomic absorption spectroscopy (AAS) analyses of the filtered leaching solutions from the WBM samples MA'd for 15 h, 20 h and 30 h.

Table 4.1 : Atomic absorption spectroscopy (AAS) analyses of the filtered leaching solutions from the WBM samples MA'd for 15 h, 20 h and 30 h.

MA Duration	Composition of the leaching solution (ppm)		
	W	Fe	Mg
15	-	12.00	4650
20	16.37	36.00	6450
30	22.43	52.28	6553

As clearly seen from Table 4.1, there is a high amount of Mg present in the solutions indicating that leaching process with HCl solution is an effective way to remove MgO from the system. Moreover, these values are in accordance with the XRD

patterns shown in Fig. 4.4, which shows that a higher amount of MgO is remained in the WBM sample MA'd for 15 h after leaching compared to the WBM samples MA'd for 20 h and 30 h. Furthermore, Mg amounts in the leaching solutions from the WBM samples MA'd for 20 h and 30 h are very close to each other, again consistently with XRD results. Fe in the leaching solutions is probably associated with the contamination from the milling medium caused by the wear of balls and of the vial. Its increasing amount with increasing MA duration supports this consideration. On the other hand, W present in the leaching solutions of the WBM samples MA'd for 20 h and 30 h strengthens the idea of dissolution of the WB phase. Following these, WBM samples MA'd for 20 h and 30 h were also leached with a 5 M HCl solution, which contains twice as much HCl as the stoichiometric amount, shown in Figure 4.5 and 4.6, respectively. However, it caused the peak intensities of all phases to decrease. The decreases in peak intensities of the WBM samples after leaching with 3.6 M compared to unleached WBM samples are related to the amount of the samples used in XRD, which is expected. However, drastic decreases in all peak intensities have been observed when 5 M HCl solution instead of 3.6 M was employed, although same amount of powders have been used in both XRD analyses, which indicates that all phases start to dissolve, which is unfavorable in a leaching process.

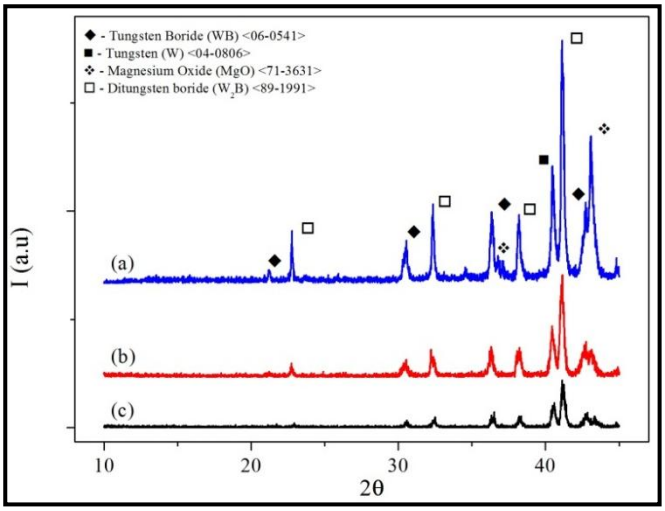

Figure 4.5 : XRD patterns of the WBM sample MA'd for 20 h; a) before leaching, b) after leaching with 3.6 M HCl and c) after leaching with 5 M HCl.

Moreover, the ratio of W phase in both samples MA'd for 20 h and 30 h does not change even 5 M HCl solution was used for leaching, meaning that W cannot be removed from this system without dissolving the boride phases. Therefore, the ideal

solution for this drawback should be to prevent the formation of the W phase from the beginning. The presence of the W phase implies that the stoichiometric amount of B_2O_3 is not sufficient for the synthesis of borides. Thus, experiments with stoichiometric excess amounts of B_2O_3 were carried out.

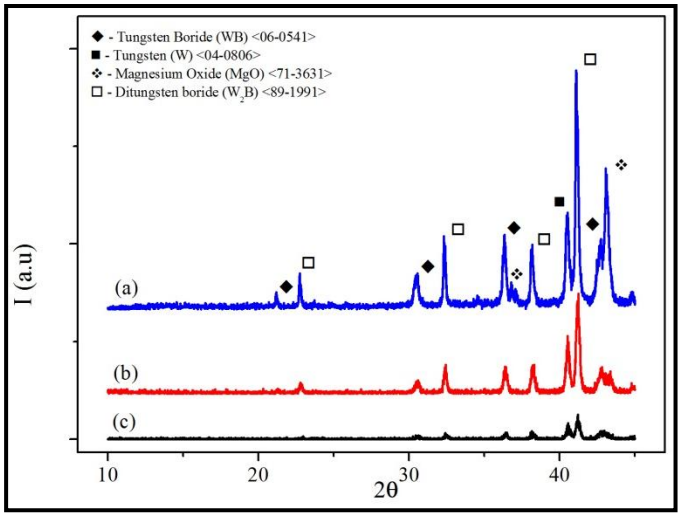

Figure 4.6 : XRD patterns of the WBM sample MA'd for 30 h; a) before leaching, b) after leaching with 3.6 M HCl and c) after leaching with 5 M HCl.

Figure 4.7 are the XRD patterns of the WBM sample MA'd for 30 h containing the stoichiometric B_2O_3 amount and those having 30%, 50% and 100% of excess B_2O_3. By presenting Fig. 4.7, it is intended to make comparisons between the sample MA'd for 30 h containing stoichiometric B_2O_3 amount with those having different excess amounts of B_2O_3.

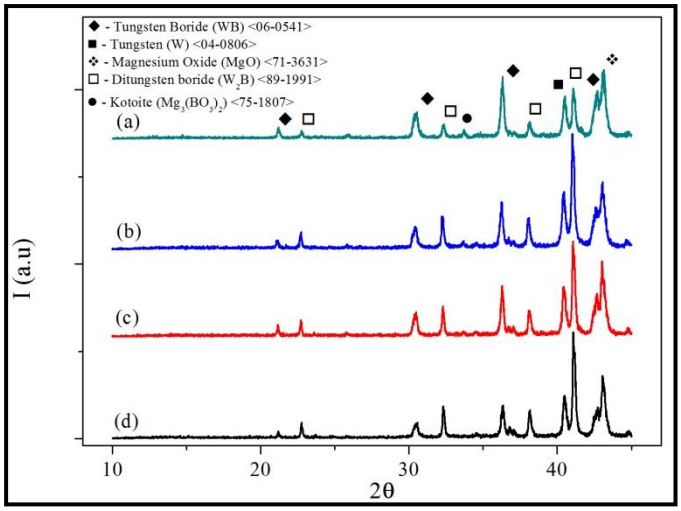

Figure 4.7 : XRD patterns of the WBM samples MA'd for 30 h; a) with 100% of excess B_2O_3, b) 50% of excess B_2O_3, c) 30% of excess B_2O_3 and d) with stoichiometric B_2O_3.

As clearly seen from Fig. 4.7, the WB-to-W_2B ratio increases with increasing amount of excess B_2O_3, although similar amounts of W phase are still present in all samples. However, synthesis of pure WB or W_2B could not be achieved. Moreover, in the WBM samples MA'd for 30 h with 50% and 100% of excess B_2O_3, a magnesium borate phase ($Mg_3(BO_3)_2$) (Bravais lattice: Simple orthorhombic; a = 0.540 nm; b = 0.842; c = 0.450 nm; Space group: Pnmn, ICDD Card No: 75-1807) is observed indicating that some of the excess B_2O_3 reacted with Mg. This $Mg_3(BO_3)_2$ phase cannot be removed from the tungsten boride system by leaching at room temperature (Yazıcı, 2009).

In overall, only a powder mixture of W + W_2B + WB could be synthesized by this route. In this case, it is not reliable to calculate the molar yield of this process by means of retrieved boride powders. However, if the amount of the removed part of the powders after leaching (0.470 g for the 30 MA'd WBM sample after leaching with 3.6 M HCl) and theoretical amount of the residual MgO (0.482 g for 1 g of product) is compared, one can definitely notice the high yield in residual removal. It is a fact that the main aim of this study could not be fully achieved, which was to produce pure WB. However, the potential applications of this synthesized W + W_2B + WB powder mixtures should not be disregarded, if it is considered that the powder mixtures of W_2B + WB have commercial uses as mentioned in the section 2.1.1 and W can be used as a binder in the sintering of borides (Ellis and Goetzel, 1990; Telle et al, 2000).

4.1.2 Characterization of W_2B_5 powders

Since XRD investigations on about WB + W_2B powder mixtures revealed that no significant changes occur in the W-B binary system for MA durations less than 20 h, characterization studies presented in this part of the section focuses on only to 2W5BM boride powders MA'd for 20 h and 30 h. Similar to the experiments with WB + W_2B powder mixtures, also during these experiments for W_2B_5 synthesis using stoichiometric amounts of initial powders, a crust formation on the walls of the stainless steel vial was observed. Similarly, ~10% of the 2W5BM sample was in the form of loose powders and the rest was kept in this crust. The only difference was that the crust formation on the walls of the vials was much more tightly bonded than the crust formation in the WB + W_2B powder mixture synthesis. Thus, breaking the

crust without damaging the vials required an extreme effort and even sometimes could not be achieved. Figure 4.8 shows the XRD patterns of loose powders in the 2W5BM samples MA'd for 20 h and 30 h.

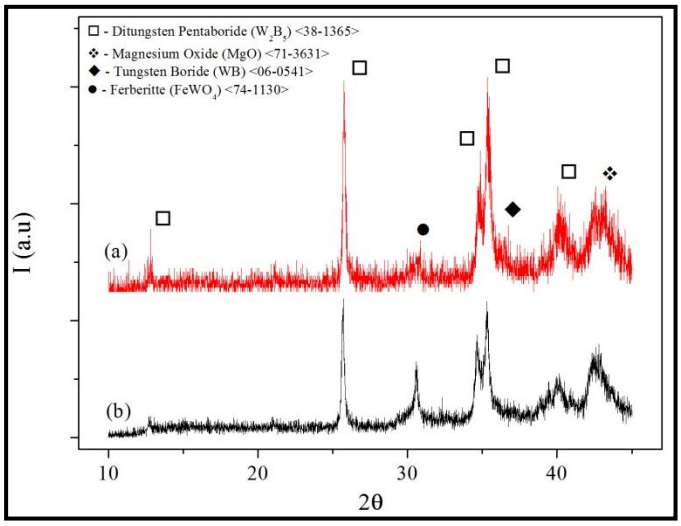

Figure 4.8 : XRD patterns of loose powders in the 2W5BM samples MA'd for; a) 30 h and b) 20 h.

As seen in Fig. 4.8, the peaks of W_2B_5 (Bravais lattice: Simple hexagonal; a = 0.298 nm; c = 1.387 nm; Space group: $P6_3/mmc$; ICDD Card No: 38-1365) and MgO can be identified in both samples. However, there is also a ferberitte ($FeWO_4$) phase (Bravais lattice: Simple hexagonal; a = 0.473 nm; b = 0.570; c = 0.495 nm; $\beta = 90^o$; Space group: P2/c; ICDD Card No: 74-1130) observed in the 2W5BM samples, whose peak intensity decreases with increasing MA duration. It is likely that Fe contamination resulted from the wear of milling medium reacted with tungsten oxide to form $FeWO_4$ present in the MA'd samples. It is also clear for the Fig. 4.8 that the intensities of W_2B_5 peaks get stronger, whereas that of $FeWO_4$ weaken. The reason for that is considered to be that further MA might cause $FeWO_4$ to decompose and that the resulting WO_x to react with B_2O_3 to form W_2B_5. This type of formation, decomposition and reformation cycles are possible with non-equilibrium processes such as mechanical alloying (Suryanarayana, 2001). Furthermore, it is evident that a small amount of WB also formed in the 2W5BM sample MA'd for 30 h. Figure 4.9 shows the XRD patterns of the crust formation in the 2W5BM samples MA'd for 20 h and 30 h. As seen in the Figure 4.9, the peaks of W, WB, W_2B, W_2B_5, MgO and $FeWO_4$ are identified in both 2W5BM samples. Similar to the XRD patterns of loose powders of these 2W5BM samples, the peak intensities of W_2B_5 phase in crust

formations increase, whereas the intensities for $FeWO_4$ peaks decrease. In fact, the peaks of both W_2B_5 and $FeWO_4$ phases in the crust formation of the 2W5BM sample MA'd for 20 h have almost same heights of intensities, which indicates that similar amounts of these phases are present in the crust.

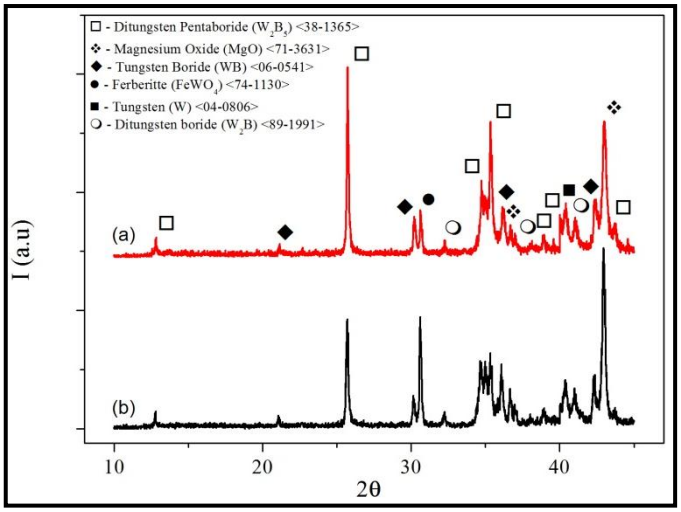

Figure 4.9 : XRD patterns of crust formations in the 2W5BM samples MA'd for; a) 30 h and b) 20 h.

It is likely that in the 2W5BM sample MA'd for 20 h, a high amount of $WO_{2.72}$ reacted with Fe during the crust formation instead of with B_2O_3 to produce W_2B_5. In this sense, crust formations and loose powders in the 2W5BM samples MA'd for 20 h and 30 h have similar characteristics. Moreover, it can be seen that there is slight increase in the amount of W with increasing MA.

Fig. 4.10 shows both 2W5BM samples MA'd for 20 h and 30 h after leaching with 5 M HCl, where loose powders and crusts were ground together in an agate mortar to prepare samples for leaching. Although 5 M HCl contains 2 times more HCl than is theoretically required to remove all MgO in the samples, it is clearly seen for Fig. 4.10 that some amount of MgO is still present in the 2W5BM sample MA'd for 20 h more than that in the sample MA'd for 30 h. Higher dissolution of MgO with increasing MA durations can be attributed to the presence of finer particles with higher surface areas resulted during MA at longer durations (Bilgi, 2007). However, there is no change in the amount of $FeWO_4$ phase present in both samples indicating that leaching with HCl cannot be used to remove $FeWO_4$. Actually, it is almost impossible to remove $FeWO_4$ for such a system via leaching process (İ. Duman, personal communication, October 20, 2011). Moreover, there is a substantial amount

of W present in both 2W5BM samples MA'd for 20 h and 30 h after leaching, which was expected due to low or no dissolution of W in an HCl solution (Walker and Tarn, 1991; İ. Duman, personal communication, 20 October, 2011).

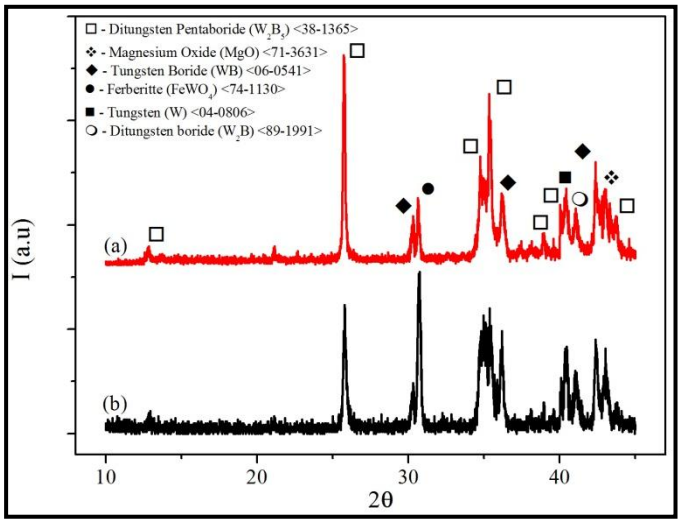

Figure 4.10 : XRD patterns of the 2W5BM samples MA'd for; a) 30 h and b) 20 h, both after leaching with 5 M HCl.

Table 4.2 gives the results of AAS analyses of the filtered leaching solutions from the 2W5BM samples MA'd for 20 h and 30 h. As clearly seen in the Table 4.2, the amount of Mg in the filtered leaching solution is higher for the 2W5BM sample MA'd for 30 h, which is consistent with the XRD patterns shown in Fig. 4.10. Moreover, there is a big difference in Fe amounts in the solutions. The reason for that is considered to be that most of the Fe resulting from contamination was consumed to form $FeWO_4$ in the 2W5BM sample MA'd for 20 h, which did not dissolve in HCl. In the 2W5BM sample MA'd for 30 h, the amount of $FeWO_4$ is much lower than that in the 2W5BM sample MA'd for 20 h indicating that most of the Fe contamination was blend in the powder mixture, which than dissolved during leaching process.

Table 4.2 : AAS analyses of the filtered leaching solutions from the samples MA'd for 20 h and 30 h.

MA Duration	Composition of the leaching solution (ppm)		
	W	Fe	Mg
20	-	16.17	5908
30	-	62.28	6135

As a result, it is evident that these conditions are not appropriate for W_2B_5 synthesis. The presence of $FeWO_4$ is the most important problem, although its amount decreases with increasing MA duration. Increasing the MA duration was not considered as an appropriate solution for this problem, since the amounts of W and other borides in the 2W5BM samples do not change with MA duration. The presence of W and low boride phases like WB and W_2B was considered to be due to insufficient amount of B_2O_3. Thus, further experiments with stoichiometric excess amounts of B_2O_3 were carried out.

Similar to other experiments with borides, also in these experiments with stoichiometric excess amounts of B_2O_3 to produce W_2B_5, crust formation on the walls of the vials was observed. However, the amount of this crust formation did not exceed more than ~10% of the entire 2W5BM sample and almost 90% of the samples were obtained as loose powders, which was the opposite case in other experiments. This phenomenon may be explained in a way that the excess amount of B_2O_3 might have acted as a surfactant in the MA process (Suryanarayana, 2001) and prevented the crust formation. However, this type of mechanism did not occur in WB + W_2B powder mixtures with stoichiometric excess amounts of B_2O_3.

Figure 4.11 shows the comparison of the XRD patterns of the crust formation in the stoichiometric 2W5BM sample MA'd for 30 h with those in the 2W5BM samples MA'd for 30 h having 50% and 100% stoichiometric excess of B_2O_3.

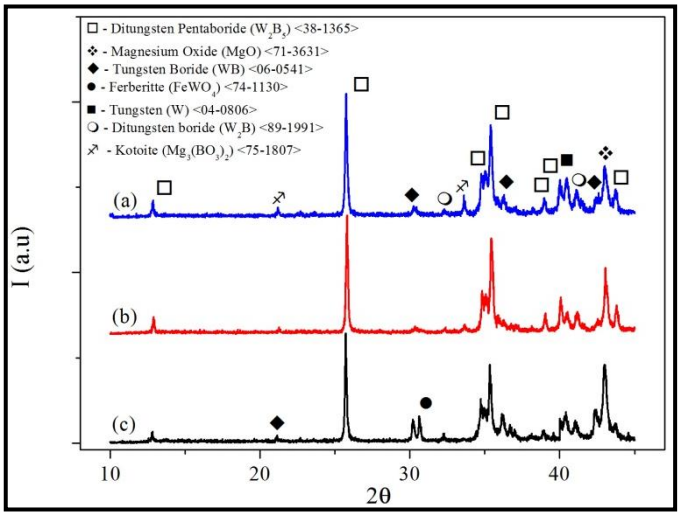

Figure 4.11 : XRD patterns of the crust formations in the 2W5BM samples MA'd for 30 h; a) with 100% of excess B_2O_3, b) 50% of excess B_2O_3 and c) with stoichiometric B_2O_3.

As seen in Fig. 4.11, the peaks of W, WB, W_2B, W_2B_5 and MgO and are identified in all three 2W5BM samples. On the other hand, the peak for $FeWO_4$ disappears when excess amount of B_2O_3 was used. Moreover, $Mg_3(BO_3)_2$ is observed in the 2W5BM samples with excess B_2O_3 and its peak intensity increases with increasing amount of B_2O_3. It is likely that some of excess B_2O_3 reacted with Mg to form $Mg_3(BO_3)_2$. Figure 4.12 shows the XRD patterns of the 2W5BM samples MA'd for 30 h having 50% and 100% stoichiometric excess of B_2O_3 after leaching with 5 M HCl. Although most of the MgO powders seemed to be removed after the leaching process, $Mg_3(BO_3)_2$ phase could not be removed due to reasons mentioned in the previous part on WB + W_2B powder mixtures.

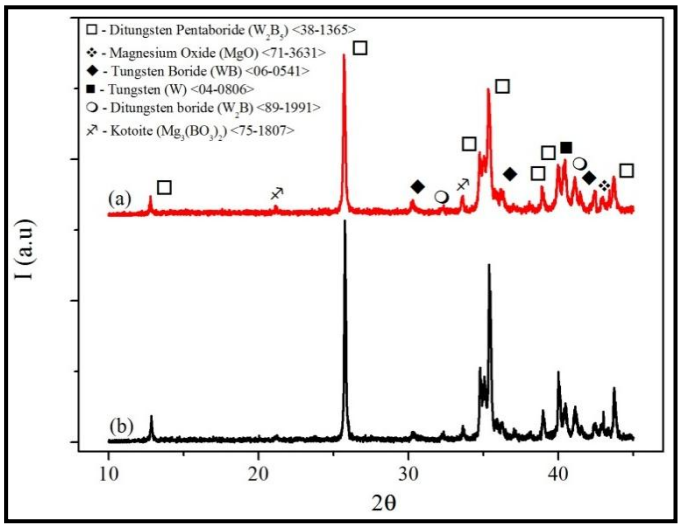

Figure 4.12 : XRD patterns of the crust formations in the 2W5BM samples MA'd for 30 h; a) with 100% of excess B_2O_3 and b) 50% of excess B_2O_3 after leaching with 5 M HCl.

Figure 4.13 reveals the comparison of the XRD pattern of loose powders in the 2W5BM sample with stoichiometric B_2O_3 with the XRD patterns of loose powders in the 2W5BM samples with 50% and 100% excess of B_2O_3, all MA'd for 30 h. As clearly seen from the Fig. 4.13, there are no traces of $FeWO_4$ or $Mg_3(BO_3)_2$ observed when excess amount of B_2O_3. Moreover, W peaks disappear in the sample with 50% excess of B_2O_3, whereas small amounts of W and WB are present in the sample 100% excess of B_2O_3. As a result, only the sample with 50% excess of B_2O_3 was leached, since it was already well known that W and WB could not be removed from the system via leaching.

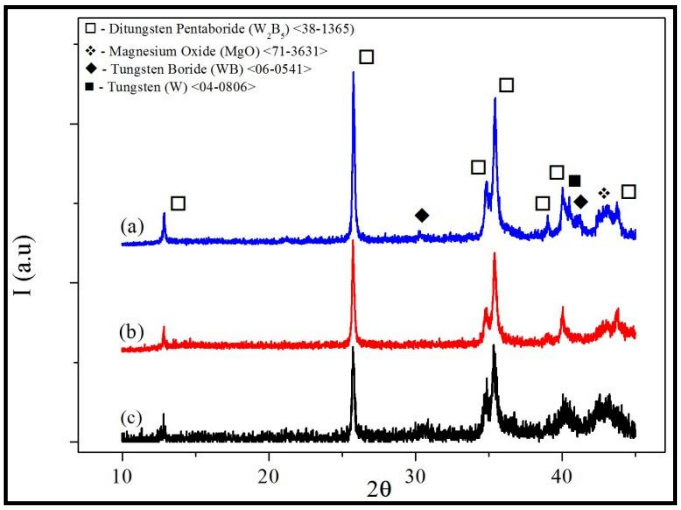

Figure 4.13 : XRD patterns of loose powders in the 2W5BM samples MA'd for 30 h; a) with 100% excess of B_2O_3, b) 50% excess of B_2O_3 and c) with stoichiometric B_2O_3.

Figure 4.14 shows the XRD pattern of the 2W5BM sample MA'd for 30 h with 50% excess of B_2O_3 after leaching with 5 M HCl. As evident from Fig. 4.14, only the peaks of W_2B_5 phase could be identified after leaching. There is only a small bump, which can be seen at the 2θ value of the strongest peak of MgO.

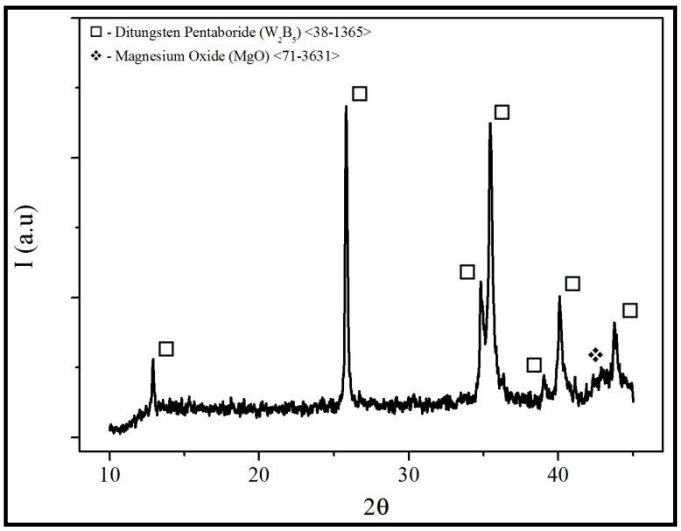

Figure 4.14 : XRD pattern of the 2W5BM sample MA'd for 30 h with 50% excess of B_2O_3 after leaching with 5 M HCl.

DTA analysis could be a good verification to determine whether the reaction is complete or not. Thus, even if a small amount of MgO was still present in the powders, it would react with W_2B_5 to form $MgWO_4$, which is a highly exothermic reaction according to the enthalpy and the Gibbs free energy calculations (HSC Chemistry® software). Figure 4.15 shows the DTA curves of the unleached and leached 2W5BM samples MA'd for 30 h with 50% excess of B_2O_3. As clearly seen

in Fig. 4.15a, there is a broad and large exothermic peak between the temperatures of ~450 ^{o}C and ~750 ^{o}C for the unleached sample. It has been shown that a self-propagating reaction results in a narrow and very intense exothermic peak during DTA due to the near instantaneous combustion of the entire sample (Setoudeh and Welham, 2006). Because of the theoretically calculated highly exothermic nature of the $MgWO_4$ formation, it was considered that this reaction would be a self-propagating reaction, however DTA analysis shown in Fig. 4.15a revealed a complex exotherm indicating that the formation of $MgWO_4$ was not a simple process. Moreover, the presence of this type of broad exotherms is indicative of a system, which reacted gradually including several reactions (Setoudeh and Welham, 2006). Moreover, several individual reactions might have occurred.

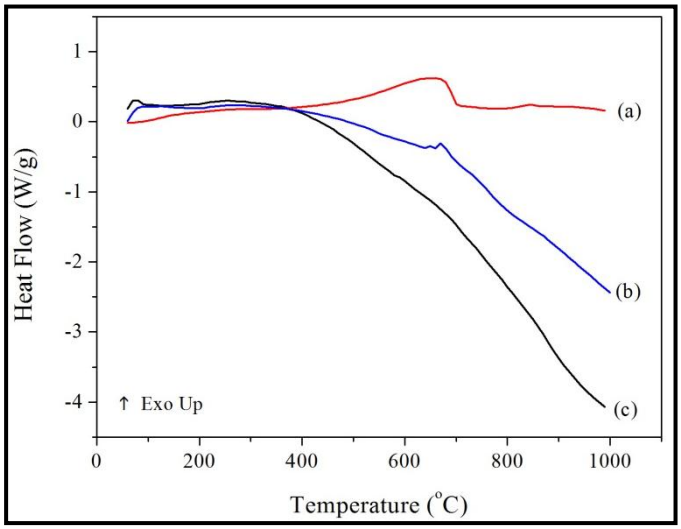

Figure 4.15 : DTA curves of; a) the unleached 2W5BM sample, b) the 2W5BM sample leached with 5 M HCl and c) the 2W5BM sample leached with 7 M HCl under Ar atmosphere (100 mL/min) at a heating rate of 10 ^{o}C/min.

In Figure 4.16a, XRD pattern of the unleached 2W5BM sample MA'd for 30 h with 50% excess of B_2O_3 is shown. As clearly seen in Fig.4.16a, almost all of the sample consists of the $MgWO_4$ phase (Bravais lattice: Simple monoclinic; a = 0.492 nm; b = 0.567; c = 0.468 nm; β = 90.7^{o}; Space group: P2/a, ICDD Card No: 27-0789) with no sign of the W_2B_5 phase, indicating that all of the W_2B_5 reacted with MgO. Moreover, peaks of W and $Mg_3(BO_3)_2$ phases can be also identified, which implies that reactions other than $MgWO_4$ formation also occurred in consistency with the DTA curve shown in Fig. 4.15a. Furthermore, the peak of MgO is also observed as expected (Fig. 4.16a), because there is more than enough amount of MgO presented

in the sample for the formation of $MgWO_4$ (HSC Chemistry® software). Therefore, according to these results from DTA and XRD analyses, it is clear that no exothermic peak would emerge during DTA analysis of the 2W5BM sample MA'd for 30 h with 50% excess of B_2O_3 after leaching with 5 M HCl, if all the MgO phase successfully removed from the sample. In Fig. 4.15b, the DTA curve of the 2W5BM sample leached with 5 M HCl is given, exhibiting a small exothermic peak around 650 ^oC-750 ^oC. Accordingly, XRD pattern of the leached 2W5BM sample MA'd for 30 h with 50% excess of B_2O_3 after DTA analysis shown in Fig.4.16b reveals the formation of $MgWO_4$, whereas there is still a substantial amount of W_2B_5 present in the sample. The absence of any MgO peak is reasonable, since there was very small amount of MgO in the sample before leaching and therefore all of MgO should have been consumed to form $MgWO_4$ leaving considerable amount of W_2B_5 unreacted.

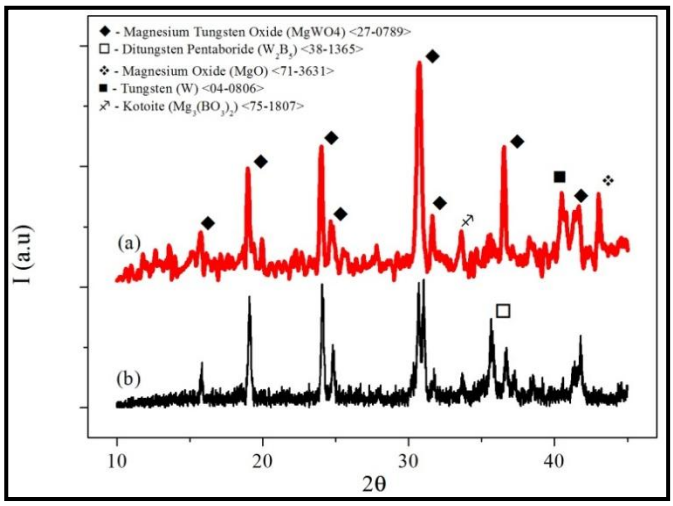

Figure 4.16 : XRD patterns of the 2W5BM sample MA'd for 30 h with 50% excess of B_2O_3; a) before leaching and b) after leaching with 5 M HCl, both after DTA analyses.

Table 4.3 shows the AAS analyses of the filtered leaching solution after second leaching of the 2W5BM sample leached with 5 M HCl, which also reveals that small amount of MgO is still present in the sample after leaching with 5 M HCl. Since it was evident from DTA, XRD and AAS analyses that leaching with 5 M HCl was not enough to obtain pure W_2B_5 powders, 7 M HCl solution (~2.5 times more than stoichiometrically required amount) was prepared for the leaching process. Figures 4.17a and 4.17b are the XRD patterns of the samples MA'd for 30 h with 50% excess of B_2O_3 after leaching with 7 M HCl and 5 M HCl, respectively.

Table 4.3 : Atomic absorption spectroscopy (AAS) analyses of the filtered leaching solutions from the 2W5BM samples MA'd for 30 h after leaching with 5 M HCl and after second leaching of the sample leached with 5 M HCl

Sample	Composition of the leaching solution (ppm)		
	W	Fe	Mg
After leaching with 5 M HCl	-	62.28	6135
After second leaching of the sample leached with 5 M HCl	-	3.17	259

As clearly evident in Fig. 4.17a, only the peaks of W_2B_5 are identified, whereas there is not any slightest trace of MgO phase. Moreover, DTA curve shown in Fig. 4.15c does not reveal any thermal event, which is a solid evidence that the sample MA'd for 30 h with 50% excess of B_2O_3 is pure enough after leaching with 7 M HCl.

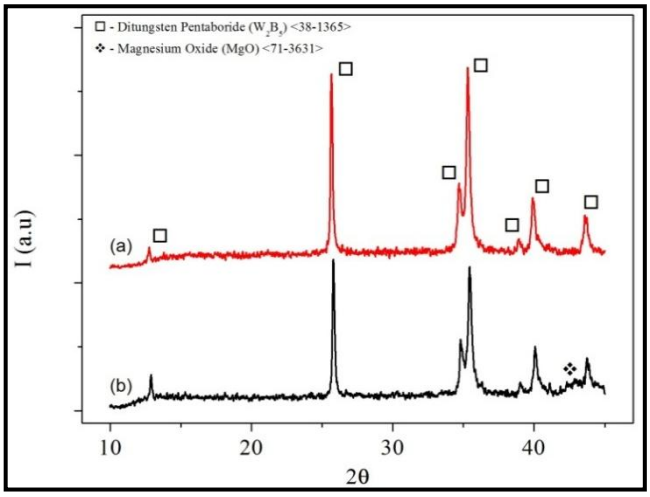

Figure 4.17 : XRD patterns taken from the 2W5BM samples MA'd for 30 h with 50% excess of B_2O_3 after leaching a) with 7 M HCl and b) with 5 M HCl.

Figures 4.18a-4.18c are the SEM-Back-Scattered Imaging (BEI) micrograph of as-blended 2W5BM sample with 50% excess of B_2O_3, SEM-Secondary Electron Imaging (SEI) micrograph of the 2W5BM sample MA'd for 30 h with 50% excess of B_2O_3 before leaching and SEM-SEI micrograph of pure W_2B_5 sample obtained after leaching with 7 M HCl, respectively. EDS scans revealed that the gray particles in Fig. 4.18a are MgO, white particles are tungsten oxide and black/dark gray particles are B_2O_3. The particle sizes vary between 60 and 70 μm for tungsten oxide and MgO powders, while the mean particle size of B_2O_3 powders higher than 150 μm. In Fig. 4.18b, SEM-SEI micrograph of the 2W5BM sample after MA for 30 h is seen. EDS scans show that light gray small powder particles are W_2B_5 and dark gray agglomerates consist of the MgO phase. It is clearly seen that, the particle sizes of

the powders drastically decrease to well below 1 μm for W_2B_5 powders, whereas MgO can be seen in larger agglomerates with sizes of 4-5 μm. After leaching with 7 M HCl, only very fine W_2B_5 powders with no MgO phase can be observed in the SEM-SEI micrograph shown in Fig. 4.18c.

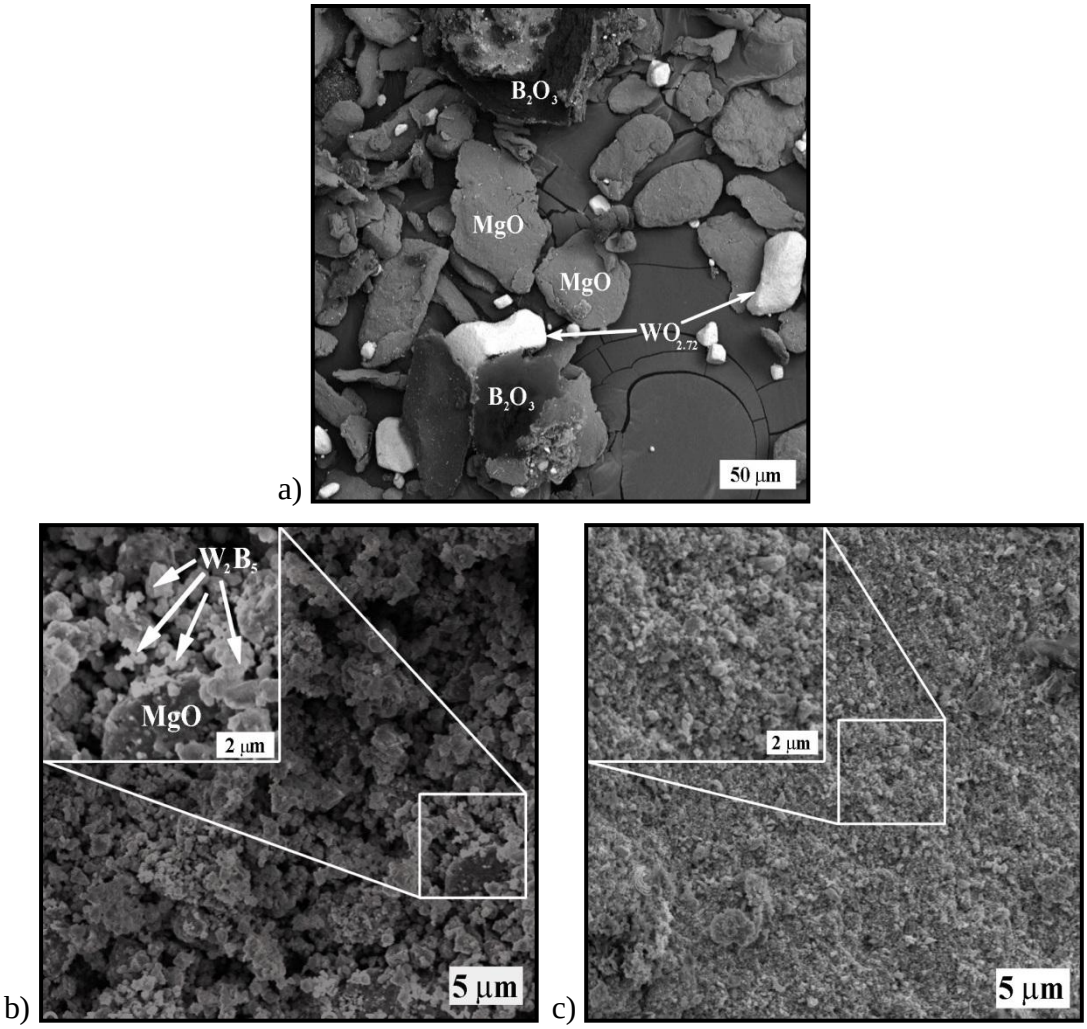

Figure 4.18 : a) SEM-BEI micrograph of as-blended 2W5BM sample with 50% excess of B_2O_3, b) SEM-SEI micrograph of the 2W5BM sample MA'd for 30 h with 50% excess of B_2O_3 before leaching and c) SEM-SEI micrograph of the pure W_2B_5 sample obtained after leaching with 7 M HCl.

Moreover, EDS scans did not reveal any MgO signals from the sample. As evident from Fig. 4.18c, particle sizes are around several 100 nm for pure W_2B_5 powders obtained via MA for 30 h of the as-blended 2W5BM powders followed by leaching with 7 M at room temperature. Average crystallite sizes of 69 nm and 55.3 nm were estimated for the 2W5BM sample MA'd for 30 h with 50% excess of B_2O_3 before leaching and after leaching with 7 M, respectively. This decrease in the crystallite

sizes after leaching with 7 M is considered to be due to strong acid attack preferentially to the grain boundaries resulting in dissolution during leaching process (İ. Duman, personal communication, October 20, 2011).

Figure 4.19 shows the particle size distributions of B_2O_3, $WO_{2.72}$ and MgO powders in as-blended 2W5BM sample as well as the samples MA'd for 30 h with 50% excess of B_2O_3 before leaching and after leaching with 7 M. According to these results, B_2O_3, $WO_{2.72}$ and MgO powders possess average particle sizes about 191 μm, 61 μm and 72 μm, which are consistent with the SEM micrograph shown in 4.18a. Average particle sizes of the 2W5BM sample with 50% excess of B_2O_3 drastically decreases to 851 nm after MA for 30 h and it further declines to 226 nm after leaching with 7 M HCl when the bigger MgO agglomerates removed.

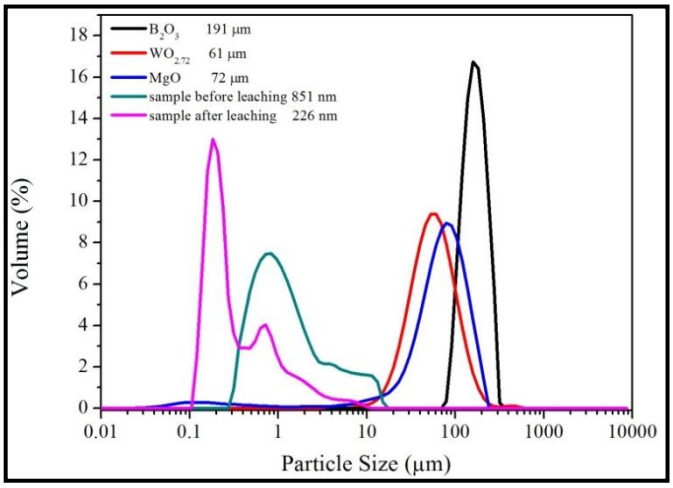

Figure 4.19 : Particle size distributions of B_2O_3, $WO_{2.72}$ and MgO in as-blended 2W5BM sample as well as the samples MA'd for 30 h with 50% excess of B_2O_3 before leaching and after leaching with 7 M.

In overall, pure W_2B_5 powders with an average particle size of 226 nm and an average grain size of 55.3 nm were successfully produced via mechanical alloying of $WO_{2.72}$, MgO and 50% stoichiometrically excess amount of B_2O_3 powders for 30 h, followed by leaching with a 7 M HCl solution. The molar yield of the W_2B_5 synthesis was calculated as 89% according to Equation 3.5.

4.2 Tungsten Oxide System

In this section, detailed information about the microstructural characterization studies on as-prepared tungsten oxide nanoparticles, nanorods and nanowires as well as tungsten oxide/CNT hybrid materials with pristine and functionalized CNTs has been

given and obtained results have been thoroughly discussed. Furthermore, possible formation mechanism for the nanorods and -wires as well as potential applications for tungsten oxide/CNT hybrid materials have been proposed.

4.2.1 Characterization of tungsten oxide nanoparticles

X-ray diffraction (XRD) pattern taken from the as-prepared nanoparticles shown in Figure 4.20 reveals a typical pattern with very broad peaks of a poorly crystallized material or even an amorphous material.

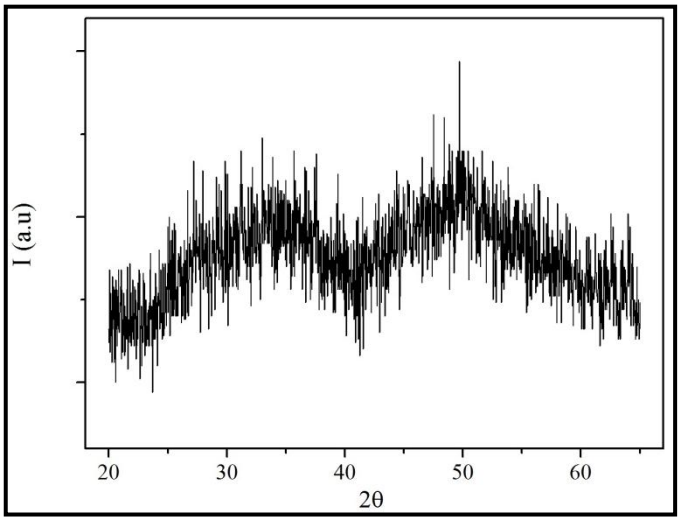

Figure 4.20 : XRD pattern of the as-prepared nanoparticles.

It is considered that also the small particle sizes could be the reason of this kind of XRD pattern and to support this idea, Transmission Electron Microscopy (TEM) investigations were carried out. Bright field (BF)-TEM micrograph (Fig. 4.21) shows that the powder particles are in the form of clusters and generally have small average diameters, with size distributions between 25-50 nm. To be more precise, average particle size and particle size distribution of the powder particles were determined from the high resolution Field Emission Gun (FEG)-SEM micrograph (Fig. 4.22) using the Image J® software, which revealed that the particle sizes of the as-prepared nanopowders show a homogenous distribution with an average particle size of 35 ± 9 nm (37 ± 10 nm for annealed powders). According to the Fig. 4.22, as-prepared nanopowders have very small particle sizes leading to high surface area. As a result of this high surface area, there is a lot of agglomeration between the powder particles, which is typical in drying processes (Maskara and Smith, 1997; Iller, 1979; Mouzon and Oden, 2007).

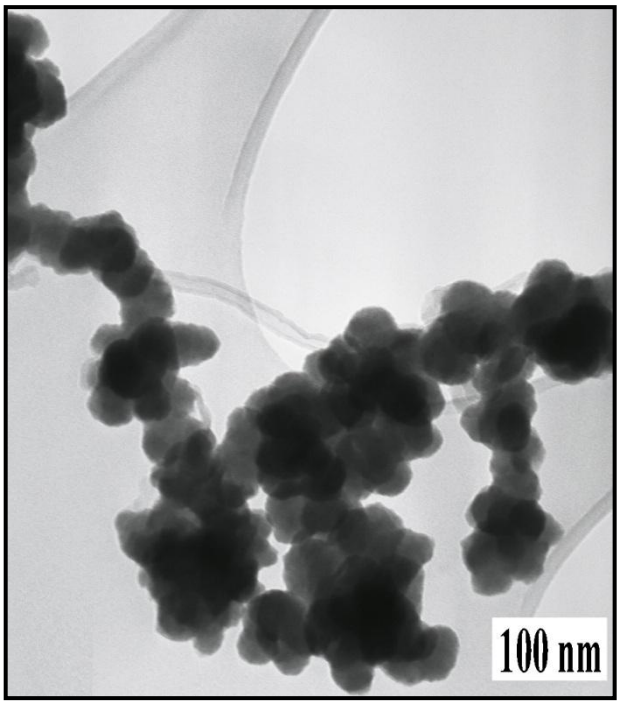

Figure 4.21 : A BF-TEM micrograph taken from a general area exhibiting as-prepared nanopowders.

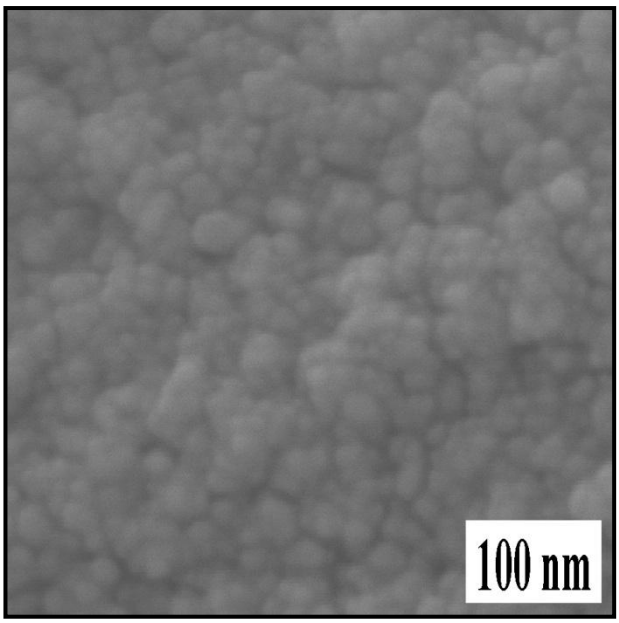

Figure 4.22 : High-resolution FEG-SEM micrographs of the as-prepared sample.

In Figures 4.23a and 4.23b, BF-TEM micrographs of the powders taken from different regions of the grid are shown. It can be observed from Figs. 4.23a and 4.23b that the as-prepared powders possess almost identical shapes although their sizes vary. Figs. 4.23c and 4.23d are the corresponding dark-field (DF) micrographs and selected area electron diffraction (SAED) patterns given as insets, respectively. Based on the SAED patterns (inset of Figs. 4.23c and 4.23d), nanopowders, which

were already crystallized during the synthesis, have the same tungsten oxide (WO_2) phase (Bravais lattice: Simple orthorhombic; a = 0.971 nm; b = 0.843 nm; c = 0.475 nm; Space group: Pnma, ICDD Card No: 48-1827). Fig. 4.23 clearly shows that the as-prepared powders have been already partially crystallized. Differential scanning calorimetry (DSC) thermogram taken from the as-prepared powders is shown in Fig. 4.24, which also supports that the crystallization of the powders were not completed. There is an exothermic peak near 450 ^{o}C, which is assigned to the crystallization of nanopowders and the large endothermic peak between 50 ^{o}C-250 ^{o}C is believed to correspond to the removal of the trapped water in the structure.

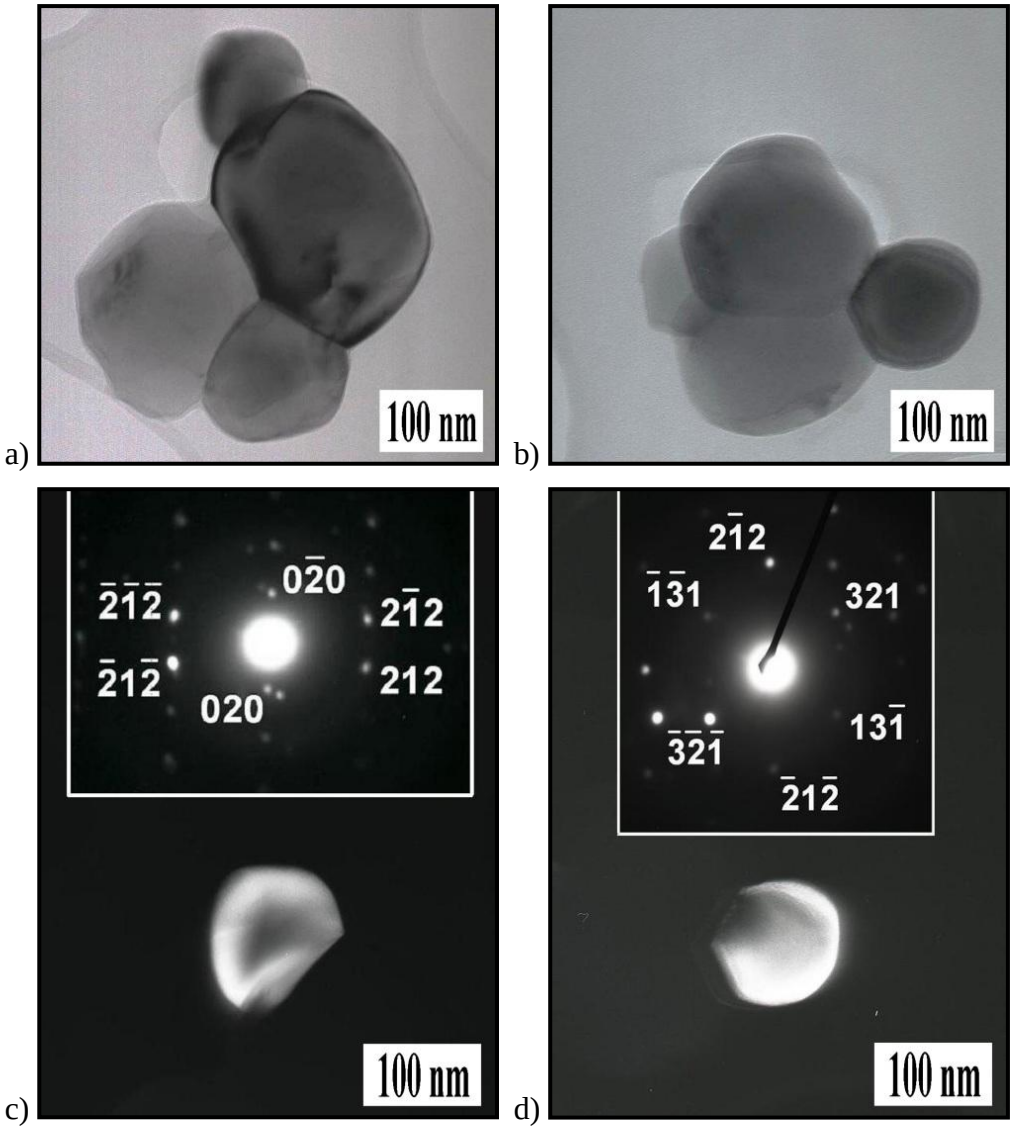

Figure 4.23 : a) and b) BF-TEM micrographs of different powder particles, c) and d) their corresponding DF-TEM micrographs with SAED patterns inset.

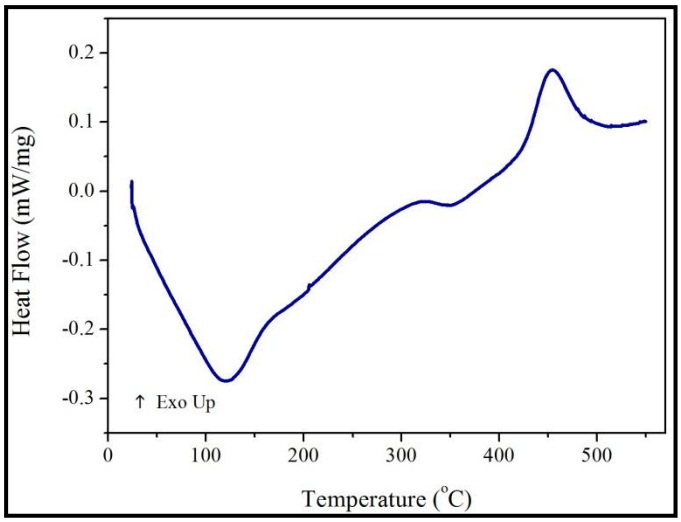

Figure 4.24 : DSC thermogram of the as-prepared powders scanned under Ar atmosphere (30 mL/min) at a heating rate of 20 ^{o}C/min.

Upon annealing the samples at 500 ^{o}C for 2 h, the XRD pattern reveals only the crystalline orthorhombic WO_2 phase (Fig. 4.25), which is identical to those identified in the SAED patterns. The broad peaks indicate small grain sizes and the nano-crystalline nature of the powder particles. An average crystallite size of 2.9 nm for the sample annealed at 500 ^{o}C for 2 h has been estimated using TOPAS 3 software, which supports this indication.

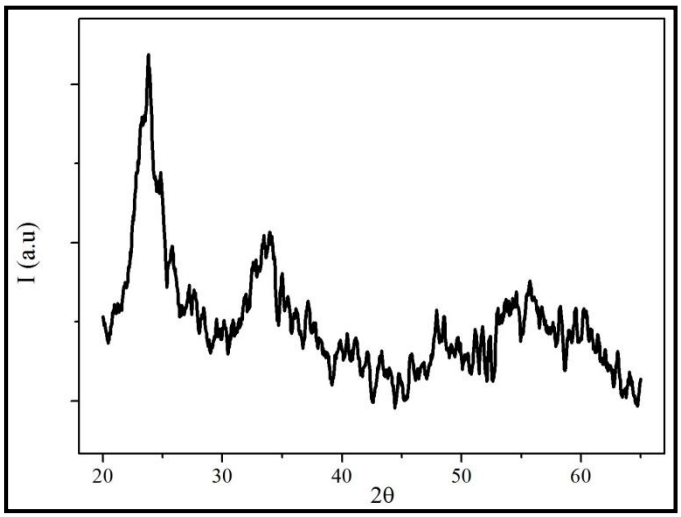

Figure 4.25 : XRD patterns of the as-prepared nanoparticles annealed at 500 ^{o}C for 2 h.

A high-resolution FEG-SEM micrograph of the as-prepared sample annealed at 500 ^{o}C for 2 h is shown in Fig. 4.26, which reveals that these annealed powders possess almost identical equiaxed shapes and sizes as the as-prepared powders (Fig. 4.22). On the basis of Figs. 4.22 and 4.26, it can be stated that the annealing process did not

cause any morphological changes. This result is also in accordance with the observations of Supothina et al (2007), who did not observe any significant grain growth and increase in surface area of WO_3 particles after annealing at 500 ^oC for 2 h.

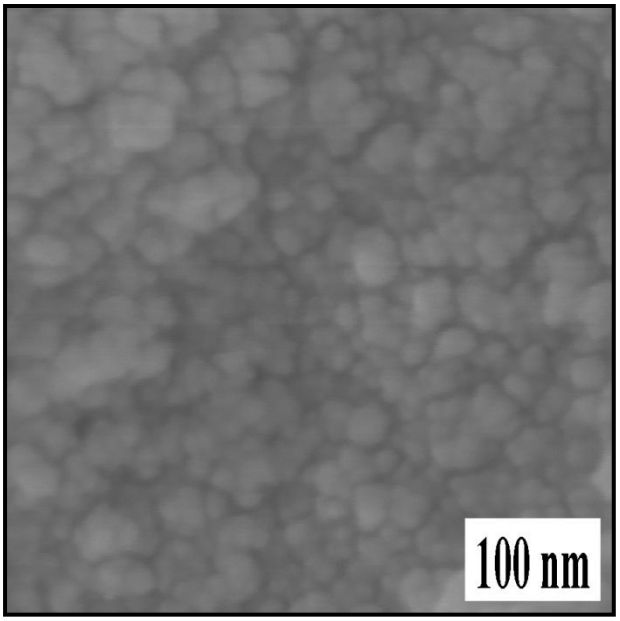

Figure 4.26 : High-resolution FEG-SEM micrograph of as-prepared nanoparticles annealed at 500 ^oC for 2 h.

In overall; TEM, XRD and DSC investigations have shown that clusters of partially crystallized nanopowders could be produced from an aqueous solution with a high yield of around 90%. Fully crystallized nanopowders without any morphological were obtained after annealing at 500 ^oC and observed via XRD and FEG-SEM analyses. As a result, these nanopowders might be a new candidate for applications below 500 ^oC, since they do not show any serious morphological or structural change.

4.2.2 Characterization of tungsten oxide nanostructures after annealing

The as-prepared nanopowders were annealed at different temperatures and changes in their morphologies and crystal structures were investigated. XRD patterns of the as-prepared samples annealed at 600 ^oC, 700 ^oC and 800 ^oC for 6 h are shown in Figure 4.27. As clearly seen, above 500 ^oC there are two stable phases. There is a second WO_2 phase (Bravais lattice: Simple monoclinic; a = 0.557 nm; b = 0.489 nm; c = 0.566 nm; β = 120.678^o; Space group: $P2_1/c$; ICDD Card No: 86-0134) present beside the orthorhombic WO_2 phase, which was identified in as-prepared WO_2

samples and WO_2 samples annealed at 500 ^oC for 2 h. The amount of monoclinic WO_2 phase in all samples seem to be more than the orthorhombic WO_2 phase, since the intensities of monoclinic WO_2 phase in all samples are much higher than those of the orthorhombic WO_2 phase.

However; as evident from the Fig. 4.27, the intensities of orthorhombic WO_2 phase increase relatively to those of monoclinic WO_2 phase with increasing temperature, which indicates that the amount of this phase increases. Consistently, Koltypin et al (2002) reported the existence powder particles consisting of a mixture of monoclinic and orthorhombic WO_2 crystals after annealing of amorphous tungsten oxide powder at 550 ^oC for 3 h under Ar. However, annealing at 1000 ^oC in that study caused the formation of a WO_2-WO_3 mixture containing nanorods (around 50 nm in diameter) and packs of these nanorods, where no traces of orthorhombic WO_2 was detected above 500 ^oC (Koltypin et al, 2002). On the other hand, Wang et al (2005) reported the coexistence of orthorhombic WO_2 phase together with a mixture of different tungsten oxides by the oxidation of W_2C nanowires at 500 ^oC.

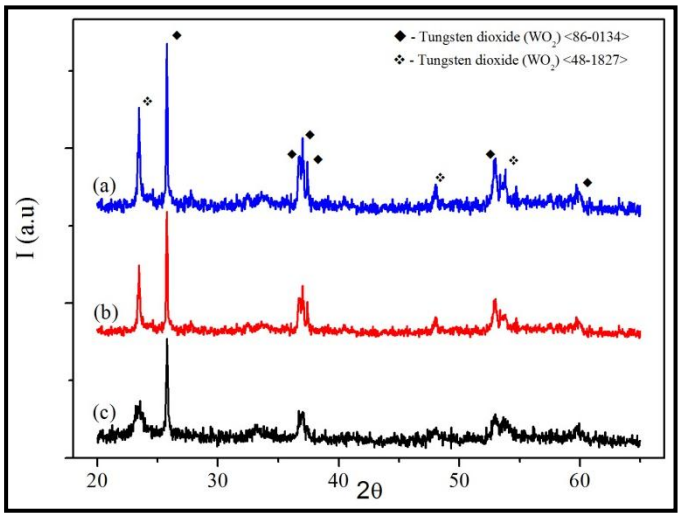

Figure 4.27 : XRD patterns of the as-prepared WO_2 nanoparticles annealed at; a) 800 ^oC, b) 700 ^oC and c) 600 ^oC for 6 h.

FEG-SEM micrographs of the nanoparticles annealed at 600 ^oC for 6 h are shown in Figure 4.28. As clearly seen from the micrographs, some interesting shaped textures emerged when the temperature have been raised to 600 ^oC from 500 ^oC. Although these textures are not totally regular shaped, one can definitely say that these formations possess different textures than its origin (parent structure).

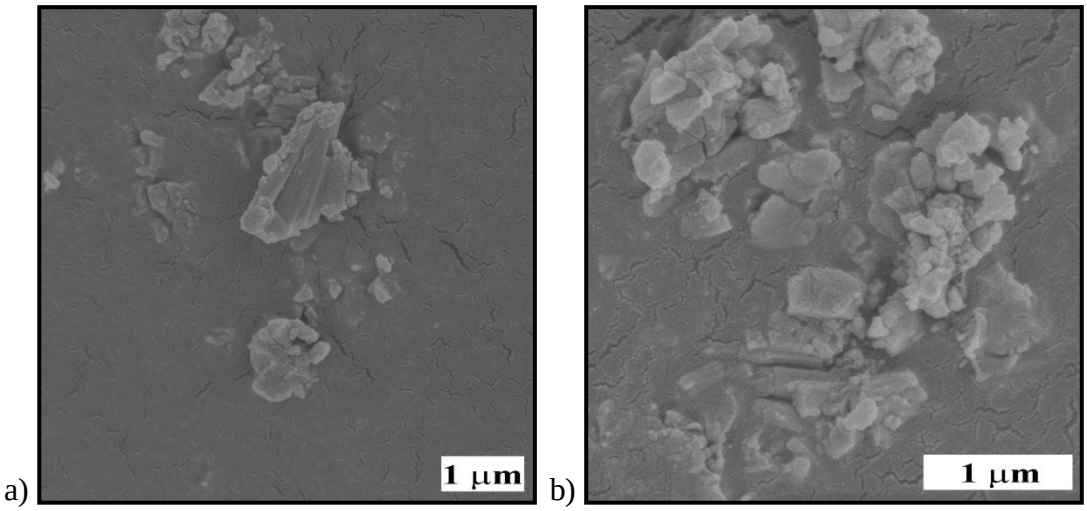

Figure 4.28 : FEG-SEM micrographs of the WO_2 nanoparticles annealed at 600 ^oC for 6 h.

These different textures become much more distinguishable when the temperature was further increased. FEG-SEM micrographs of the sample annealed at 700 ^oC for 6 h clearly reveal the formation of regularly shaped nanorods on the surface of the parent structure (Fig. 4.29). The nanorods have an average diameter of 60-70 nm and a length of several 100 nm. Most importantly, these nanorods seem to grow from the parent structure as clearly seen in the inset SEM micrograph (Fig. 4.29). Regions, where the nanorods clearly root from the parent structure, are marked with a white arrow in the inset of the Fig. 4.29.

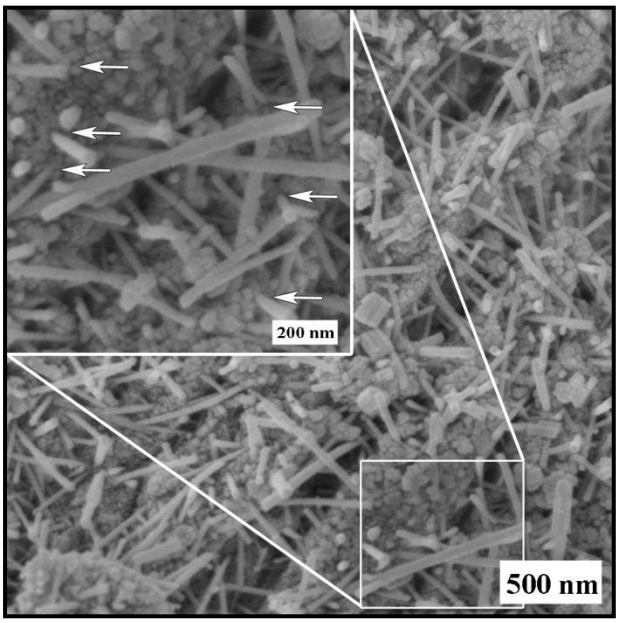

Figure 4.29 : FEG-SEM micrograph of the WO_2 nanoparticles annealed at 700 ^oC for 6 h with higher magnification inset.

Figure 4.30 shows a representative FEG-SEM micrograph of the nanoparticles annealed at 800 ^{o}C for 6.

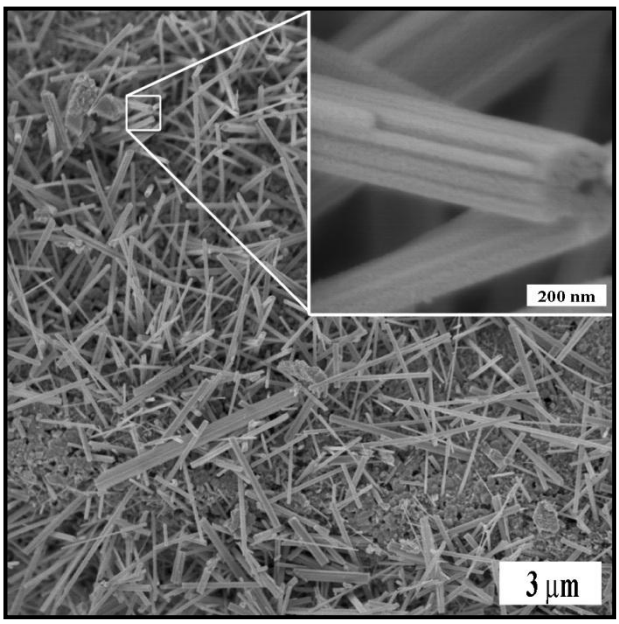

Figure 4.30 : Representative FEG-SEM micrograph of the WO_2 nanoparticles annealed at 800 ^{o}C for 6 h with higher magnification inset.

As clearly seen in the Fig. 4.30, the aspect ratios and the amount of the nanorods increase with increasing annealing temperature. Although the diameter of individual nanorods does not change, the lengths of nanorods increase from several hundreds of nanometers to several micrometers. Moreover, it is obvious form the inset micrograph of the Fig. 4.30 that nanorods coalesce into a bundle-like structure.

Figure 4.31 is a FEG-SEM micrograph taken from the parent structure of the sample annealed at 800 ^{o}C for 6 h. This micrograph reveals clearly that the nanorod and their bundles initiate from its parent structure. This microstructure conforms very well with the study of Pfeifer et al (1996), who observed the formation of $W_{18}O_{49}$ nano-needles rooting on an amorphous-like substrate. They suggested that the single crystalline nanorods grew by a root growth mechanism from a nucleus formed in the cauliflower-like surface of the parent particle. Root growth of a leading whisker in the growth process of $W_{18}0_{49}$ needles is also a new hypothesis (Pfeifer et al, 1996). However, certain experimental observations published in the literature seem to support this hypothesis (Pfeifer et al, 1996; Sarin, 1975). On the other hand, Gu et al (2006) reported the formation of WO_3 nanorods from the nanoparticles where different types of sulfates acted as capping agents. They mentioned about a

mechanism for growth of various oriented and hierarchical nanostructures via self-assembly of nanocrystals, where primary particles may aggregate in an oriented fashion to produce a larger single crystal, or they may aggregate randomly and reorient, recrystallize, or undergo phase transformations to produce larger single crystals (Gu et al, 2006).

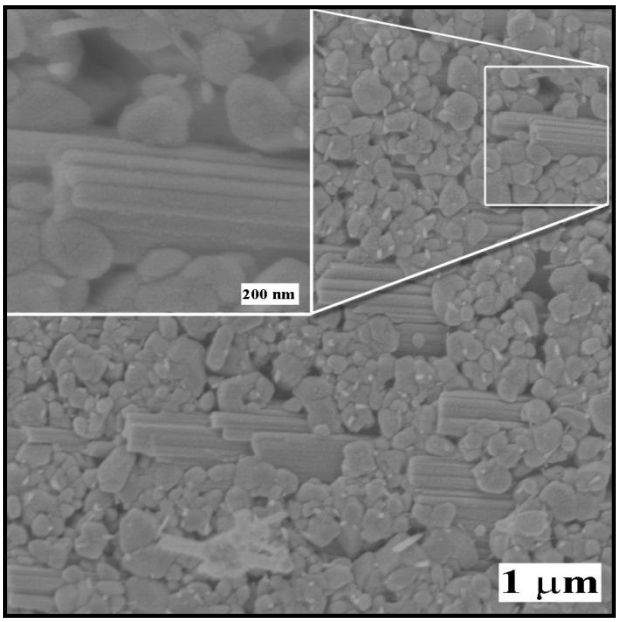

Figure 4.31 : FEG-SEM micrograph of the WO_2 nanoparticles annealed at 800 ^{o}C for 6 h showing the roots of the nanorods in the parent structure.

Figure 4.32a is a typical BF-TEM micrograph showing a single nanorod with a diameter of approximately 50 nm and a length of several 100 nm. Figure 4.32b is the SAED pattern taken from the nanorod revealing the single crystalline nature of the nanorods indexed as belonging to the orthorhombic WO_2 phase.

A high-resolution TEM (HRTEM) micrograph of a WO_2 nanorod, shown in Figure 4.33, reveals that lattice spacings of 0.381 and 0.301 nm can be indexed. These d-spacings correspond to the (111) and $(12\bar{1})$ planes, respectively. In addition, the major peak in the XRD pattern in Fig. 4.27 corresponds to the (111) plane for the orthorhombic WO_2 phase, which is the closest-packed plane of the WO_2 crystals, suggesting that the dominant growth direction of the WO_2 nanorod bundles is along the closest-packed plane. Furthermore, there is an amorphous layer on the surface of these nanorods. These amorphous layers on nanorod surfaces develop to decrease the surface free energy and to keep the surface tension of the nanorods balanced, otherwise, they could not remain as nanorods (M.L. Öveçoğlu, personal

communication, May 18, 2010). In other words, much energy can be gained by surface reconstitution toward an amorphous gradient surface layer; one costly interface is substituted by two with much lower energy.

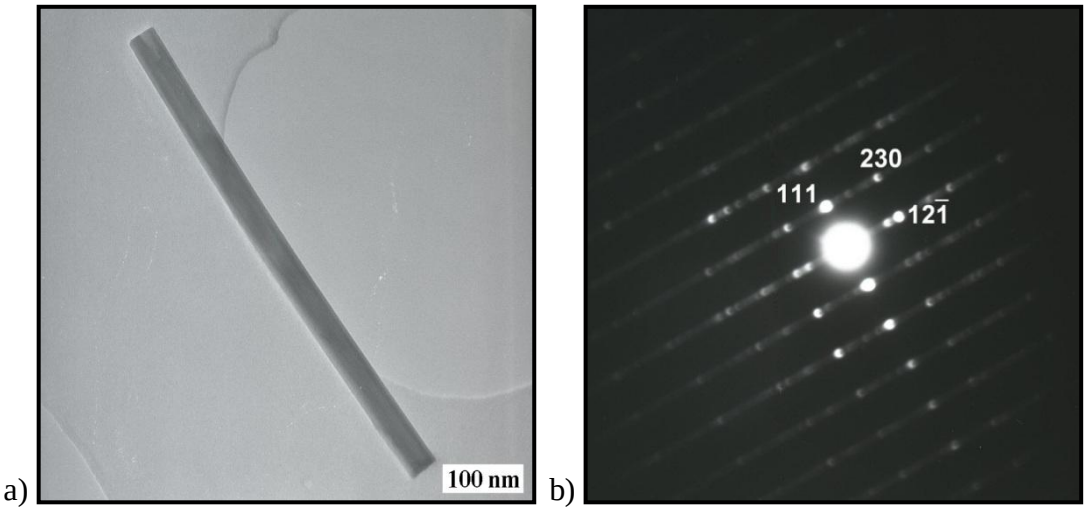

Figure 4.32 : a) BF-TEM micrograph and b) the SAED pattern taken from an individual nanorod.

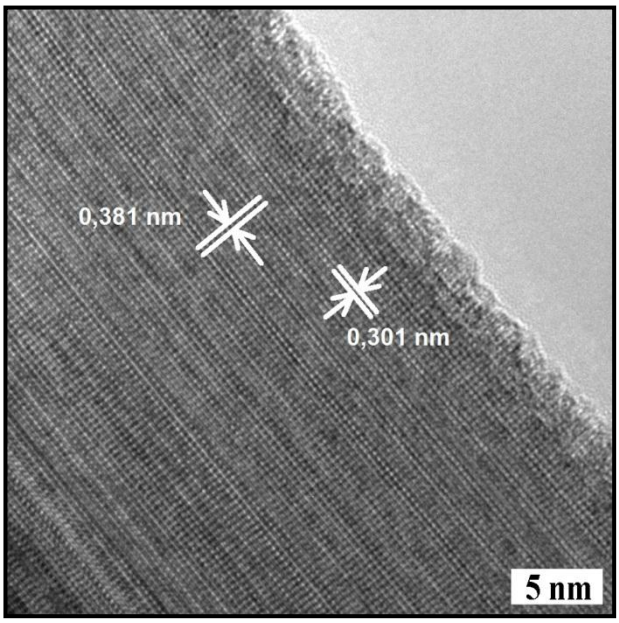

Figure 4.33 : HRTEM micrograph of a nanorod.

Figure 4.34 shows the BF-TEM micrograph and the diffraction pattern taken from the nanopowders, which were present beside the nanorods and considered as the parent phase. The BF-TEM micrograph (Fig. 4.34a) reveals that these nanopowders possess equiaxed shapes with very small diameters well below 20 nm. Actually, these powder particles appeared in the form of large agglomerates as shown in the inset of the Figure 4.34a, which broke up when the e-beam was focused on. The ring

pattern in Fig. 4.34b shows that these powders are consisted of the monoclinic WO_2 phase.

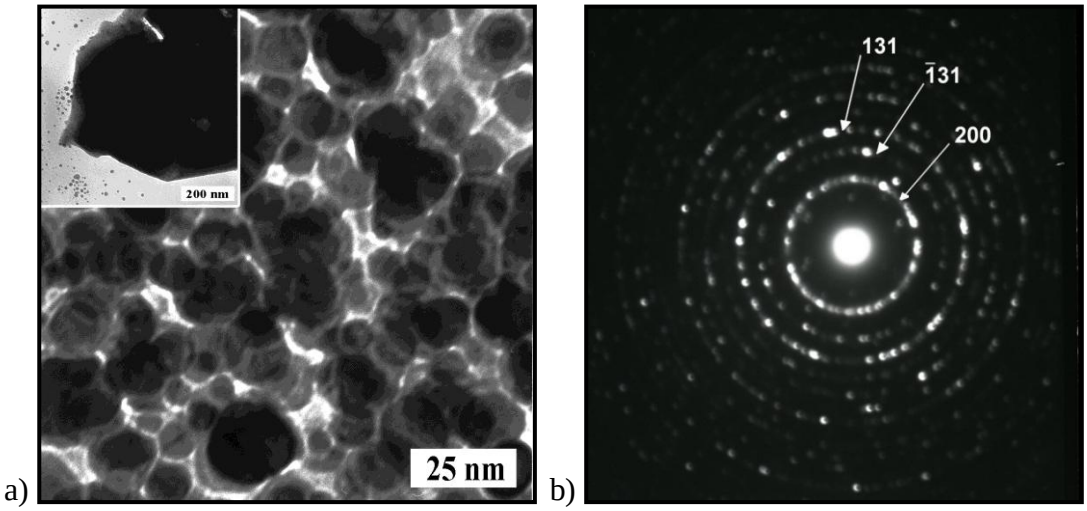

Figure 4.34 : a) BF-TEM micrograph and b) the SAED pattern taken from nanopowders, which were present beside the nanorods.

Figure 4.35 shows the HRTEM micrograph taken from nanopowders, which were present beside the nanorods. According to this micrograph, lattice spacings of 0.243 nm, 0.216 nm, 0.184 nm and 0.170 nm can be indexed. On this HRTEM micrograph, these interplanar spacings correspond to (200), (012), $(30\bar{2})$ and $(\bar{1}13)$ planes of the monoclinic WO_2 phase, respectively. Moreover, crystallite sizes around 3 nm can be easily noticed.

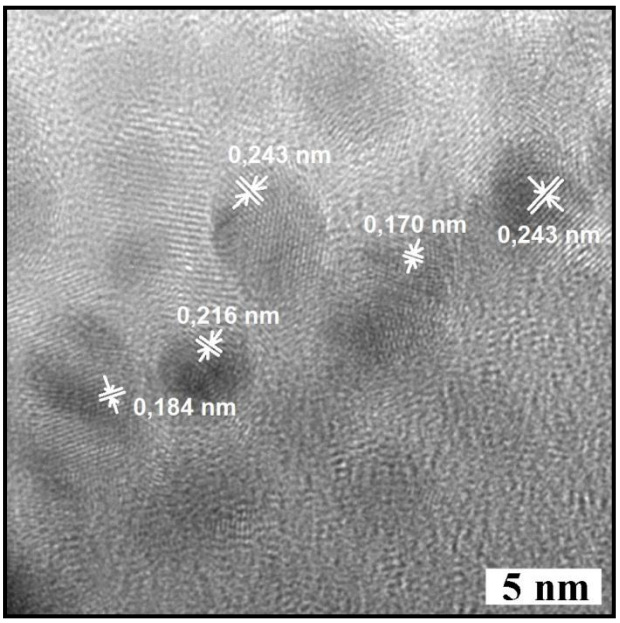

Figure 4.35 : HRTEM micrograph of WO_2 nanopowders.

Considering that this sample was annealed at 800 ^{o}C for 6 h, estimated average crystallite size of 2.9 nm for the sample annealed at 500 ^{o}C for 2 h is quiet reasonable. Therefore, these results of the TEM and HRTEM investigations are in consistency with the XRD results, which clearly indicates that the nanorods are made of orthorhombic WO_2 and the nanopowders are made of monoclinic WO_2 crystals.

To have better understanding about the effect of annealing durations and formation mechanism of these nanorods , nanopowders were annealed for different durations at different temperatures. Figure 4.36 shows the XRD patterns of the samples annealed at 700 ^{o}C for 2 h and at 800 ^{o}C for only 5 min. According to these patterns, both samples consist of the monoclinic and orthorhombic WO_2 phases. The intensity ratio of the orthorhombic WO_2 phase to the monoclinic WO_2 phase in the sample annealed at 800 ^{o}C for 5 min is relatively higher than in the sample annealed at 700 ^{o}C for 2 h, indicating that the amount of orthorhombic WO_2 phase is higher in the sample annealed at 800 ^{o}C for 5 min.

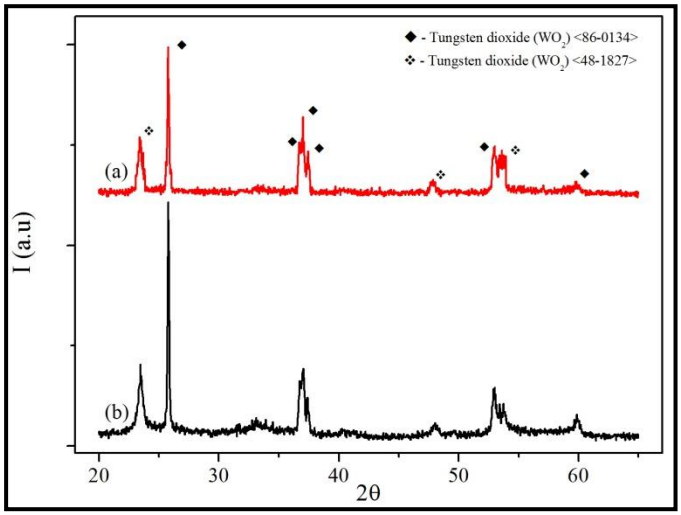

Figure 4.36 : XRD patterns of the samples annealed; a) at 800 ^{o}C for only 5 min and b) at 700 ^{o}C for 2h.

Figures 4.37a and 4.37b show the FEG-SEM micrographs of the sample annealed at 700 ^{o}C for 2 h. According to Fig. 4.37a, there are regular rectangular-like or rod shaped textures formed. Moreover, Fig. 4.37b reveals the formation of few nanorods with diameters of below 100 nm on some island-like structures assembled over the surface. These island-like morphologies are considered as the origin of the nanorod formation, which will be explained later.

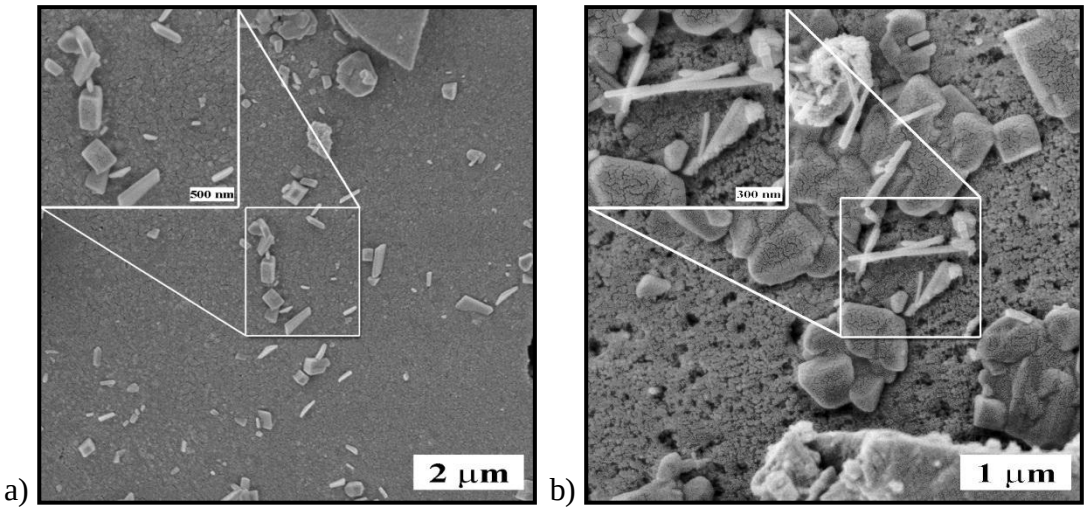

Figure 4.37 : FEG-SEM micrographs of the sample annealed at 700 ^{o}C for 2 h with; a) regular shapes and b) some nanorod formations on or near the island-like structures.

Figure 4.38 is a FEG-SEM micrograph of the sample annealed at 800 ^{o}C for 5 min. It is clearly seen that similar nanorod textures with a diameter of below 100 nm have already started to form, however their number is limited because of insufficient dwell time. Considering that similar structures have formed in both samples annealed at 700 ^{o}C for 2 h and at 800 ^{o}C for 5 min., it can be deduced that during annealing temperature has more crucial role than the annealing duration. Therefore, these results suggest that a suitable combination of annealing temperature and time is required for the stable growth of nanorods. Moreover, it is apparently evident from Fig. 4.38 inset that these nanorods root from a parent phase.

In the light of these observations, it can be speculated that the change in surface morphology of the annealed samples suggest that first the nucleus sites of WO_2 nanocrystallites are assembled as island-like structures with a cauliflower-like surface. Then, leading individual nanorods root from these parent structures followed by the growth of thickness via root growth of secondary rods parallel to the primary rod forming bundles of nanorods (Figs. 4.30 and 4.31). The aggregation of nanorods into a bundle-like structure might be favored because it probably reduces the interfacial energy between the nanorods. Finally, these nanorods or bundles of nanorods might act as new nuclei sites for new rods.

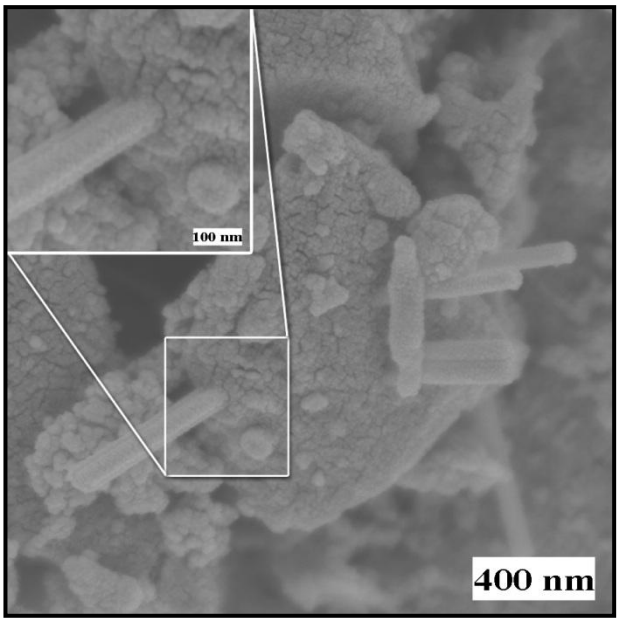

Figure 4.38 : SEM micrograph of the sample annealed at 800 ^{o}C for 5 min with higher magnification inset.

Following these, a last set of experiments were carried out in which the samples were annealed at 900 ^{o}C and 1000 ^{0}C for 6 h. SEM micrographs of these samples are shown in Figures 4.39 and 4.40, respectively. In Fig. 4.39, both the nanorods and the parent structure are clearly seen.

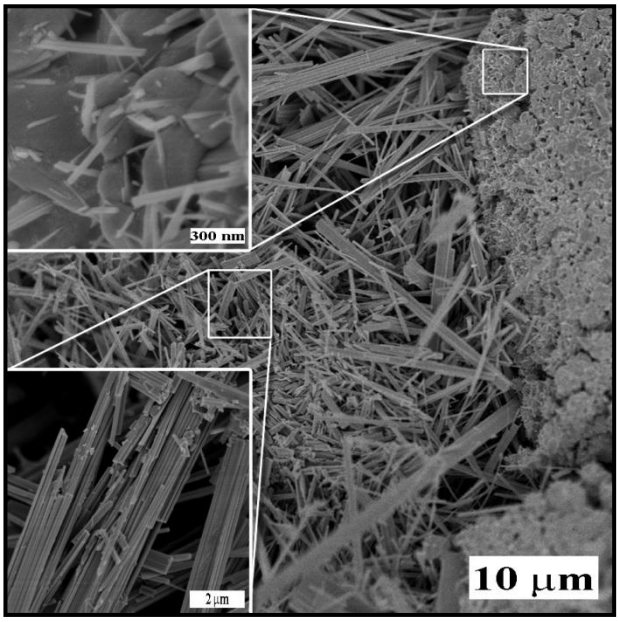

Figure 4.39 : FEG-SEM micrograph of the sample annealed at 900 ^{o}C for 6 h with higher magnifications inset.

a) 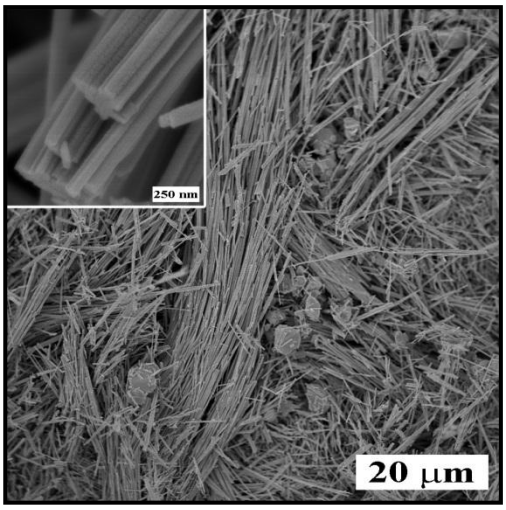

b) 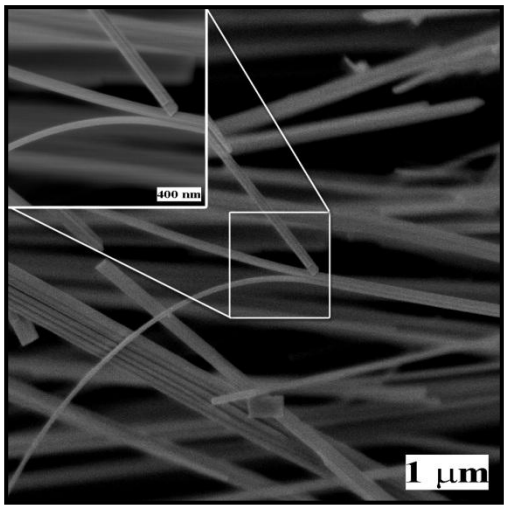

Figure 4.40 : FEG-SEM micrographs of the sample annealed at 1000 ^{o}C for 6 h with higher magnifications inset.

As evident from the figure insets, the nanorods root from the parent structure and nanorod bundles grew up to several micrometers, while the diameters did not change significantly. Actually, the expected result would be that the nanorods would grow more with increasing temperature. However, they grew up much more above expectations especially for the sample annealed at 1000 ^{o}C for 6 h as shown in Figure 4.40a. They became nanowires with a length of several 10 μm. However, their nature to be present in bundles seemed not to vary as clearly seen inset the Fig. 4.40a. Moreover, their diameter is still 60-70 nm, which clearly showed that the length was the only dimension, which changed. Figs. 4.30 and 4.40a reveal almost the identical nature of these nanorod or nanowire bundles. Another, interesting property of these nanowires is that they are pretty elastic in nature, as shown in Fig. 4.40b, compared to the nanorods produced at lower temperatures. More or less, one could definitely say that they have wool or cotton like fabric, which is very different from the nature of nanoparticles annealed at lower temperatures. All things considered, WO_2 nanorods and nanowires can be produced via annealing of the as-prepared WO_2 nanopowders. Although the formation mechanism has not been clearly understood yet, a root growth mechanism from a parent structure can be proposed. Moreover, it is evident that with increase in annealing temperature, the length of the nanorods increases, whereas the small diameters of 60-70 nm remain unchanged.

4.2.3 Characterization of CNTs and CNT-tungsten oxide hybrid materials

4.2.3.1 Characterization of as-prepared pristine and functionalized CNTs

Investigating the CNTs with SEM provides an overview of their morphology and quality. In Fig. 4.41, there are low magnification FEG-SEM micrographs of pristine CNTs.

a) 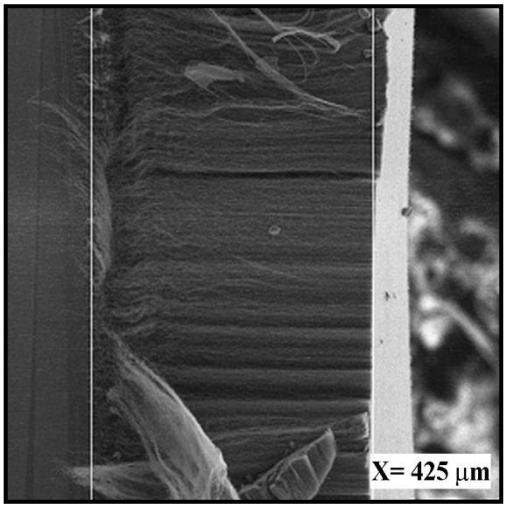

b) 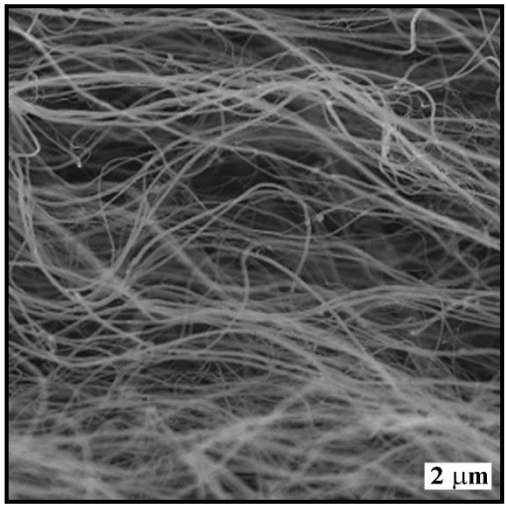

Figure 4.41 : Low magnification FEG-SEM micrographs of carpet growth pristine CNTs.

As clearly seen, the as-prepared CNTs are well aligned and the CNT carpet has a length of about 425 μm, which is consistent with the 4 h duration of growth. The white layer in the Fig. 4.41a is the quartz substrate. The SEM pictures demonstrate that CNTs possess a very high aspect ratio. While the diameters of CNTs can easily be measured by examining the SEM or TEM micrographs, measuring their lengths is not trivial. The CNTs are so long and entwined and it is rarely possible to identify any entire CNT. However, in the case of aligned carpets on substrates, the length of CNTs can be estimated as the length of carpets. In the cases where no substrate were used, the CNTs grew directly on the quartz tube and became randomly oriented as well as entangled because of scratching from the quartz tube (Fig. 4.42). Moreover, in a closer observation some amount of contamination (brighter spots in Fig. 4.42) can be seen, which formed during the process, which are generally amorphous carbon, nanoparticles and catalyst residues.

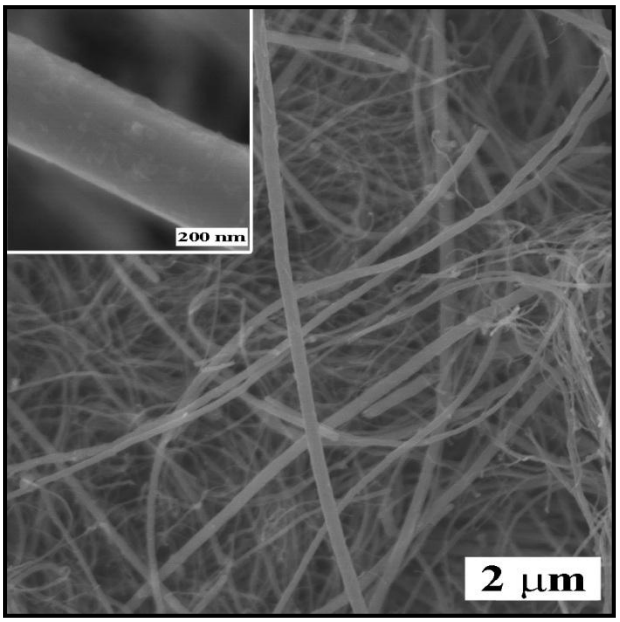

Figure 4.42 : FEG-SEM micrograph of randomly oriented and entangled CNTs with high magnification SEM micrograph of an individual CNT.

Figure 4.43 is a BF-TEM micrograph of a MWNT with iron particles inside (dark grey regions in the tube) and some contamination on the surface (dark grey and black areas). When the CNTs are functionalized, the amount of contamination on the surfaces and catalysts inside the CNTs should be minimized.

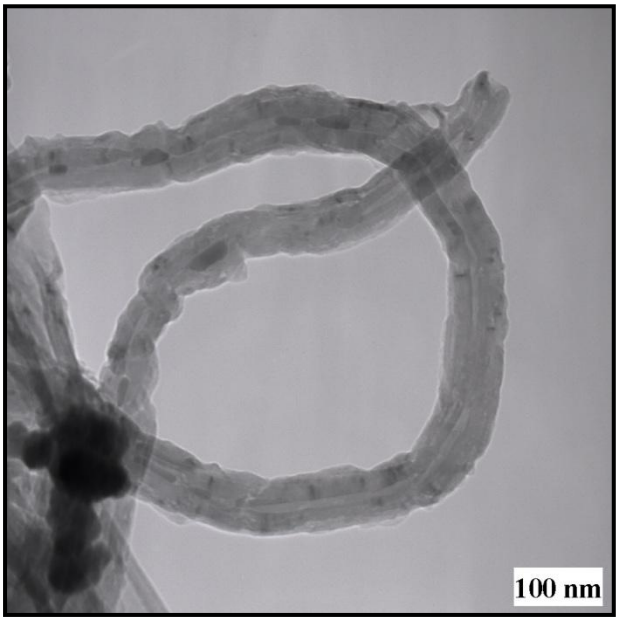

Figure 4.43 : BF-TEM micrograph of a pristine MWCNT.

The FEG-SEM micrograph shown in Figure 4.44 and the BF-TEM micrograph shown in 4.45 reveal that the functionalized CNTs (fCNTs) are free from any

catalysts and contamination. Moreover, some alterations on the walls of the fCNTs can be seen in Figures 4.44 and 4.45.

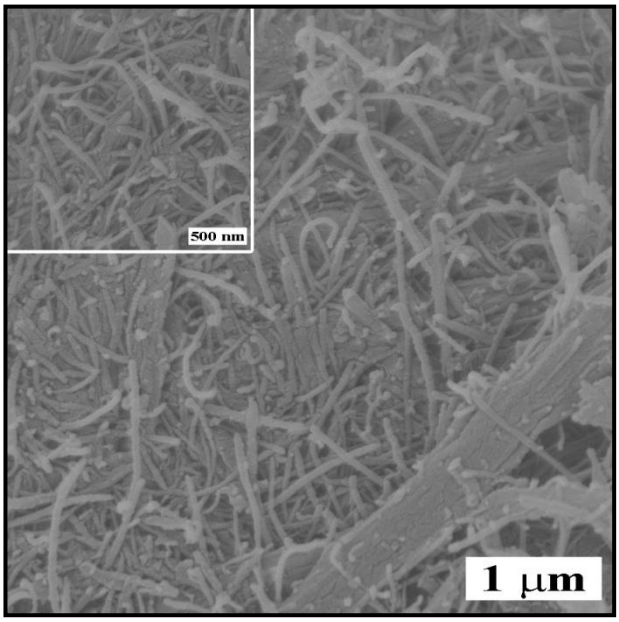

Figure 4.44 : FEG-SEM micrograph of functionalized CNTs with higher magnification inset.

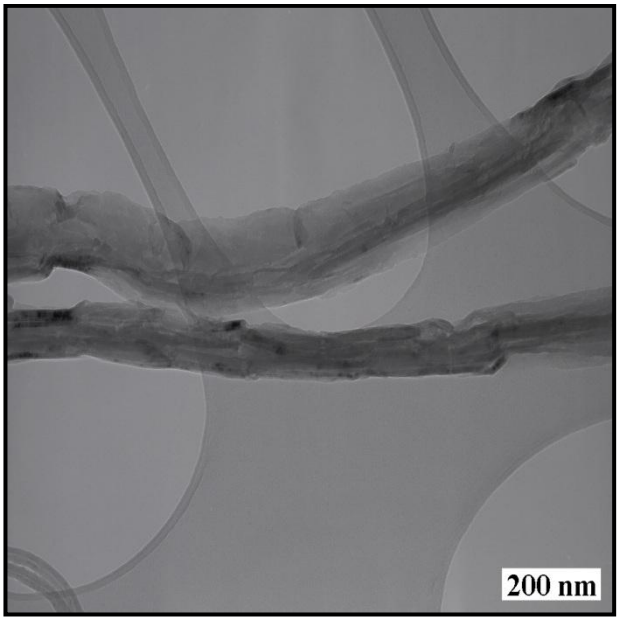

Figure 4.45 : BF-TEM micrograph of fCNTs.

These alterations are caused by the strong acid attack to the walls during the functionalization process. In addition, the lengths of fCNTs are smaller than those of pristine CNTs, as shown in Fig. 4.44. The darker regions on the fCNT surfaces shown in Fig. 4.45 are some surface defects causing the e-beam to scatter or diffract differently. In order to monitor the functionalization process, XRD analyses have

been also carried out. Figure 4.46 shows the XRD patterns of pristine and functionalized CNTs. As seen in Fig. 4.46, after the functionalization process, the peak intensities decrease and peaks are broadened, due to shortening of the CNT lengths and the high amount of strain induced by the acid attack during functionalization.

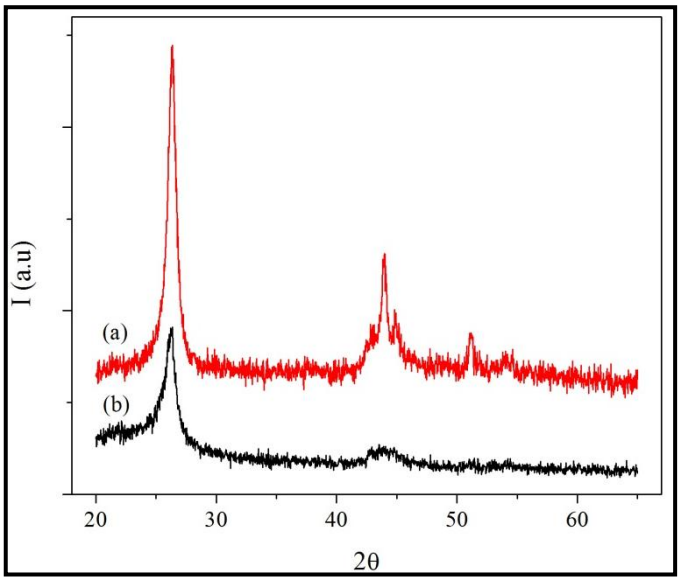

Figure 4.46 : XRD patterns of; a) pristine and b) functionalized CNTs.

4.2.3.2 Coating of CNTs with tungsten oxide nanoparticles for hybrid synthesis

After the CNTs have been synthesized and characterized successfully, they have been coated by following two main routes. In the first route, functionalized CNTs have been used in different solutions (water or water/ethanol). In the second route, pristine CNTs have been used, where benzyl alcohol (BA) has been employed as a surfactant. In the early works, pristine CNTs were used for coating and their hydrophobic nature provided little attractive interaction with the inorganic compound and thus limited the quality of the coating. The most common approach to change the surface chemistry of CNTs is to functionalize them by treating in strong oxidizing acids (H_2SO_4-HNO_3) (Eder, 2010). This process introduces a variety of organic groups, with limited control over their number, type, and location, and causes surface etching and shortening of the tubes (Korneva, 2008; Eder, 2010). Consequently, the inorganic coatings on acid-treated CNTs provides better interaction in comparison with pristine CNTs (Eder, 2010). Alternatively, pristine CNTs can be used with a surfactant like benzyl alcohol, which adsorbs onto the CNTs' surface via π-π interactions with the alcohol's benzene ring while simultaneously providing

hydrophilic hydroxyl groups on the CNT surface for better interaction with the coating (Eder and Windle, 2008; Eder, 2010).

Both routes have led to coatings but there should be more research to do about this subject specifically to achieve ideal coatings. In both routes, there was not any formation of coating when only water was used as the solution. Figure 4.47 is a FEG-SEM micrograph of nanotubes without any coating when only water was used. Similar structures were observed for both routes.

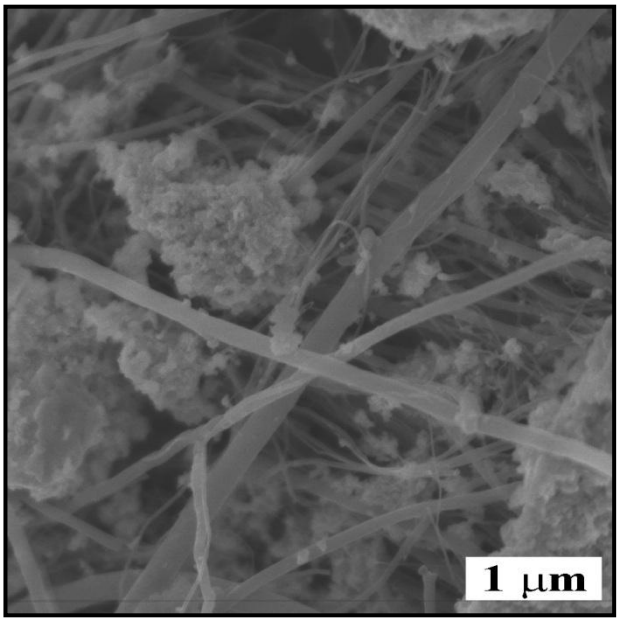

Figure 4.47 : FEG-SEM micrographs of CNTs without any coating when only water was used.

Tungsten oxide particles precipitated in the form of large clusters beside the nanotubes and no CNT was coated. This type of microstructure of tungsten oxide and CNTs are very similar to the microstructures WO_x/CNT hybrid composites, which have already been used in gas sensors (Hashishin and Tamaki, 2008; Balazsi et al, 2008). So, with some improvements, these materials prepared via both routes might lead to alternative candidates for sensor applications.

In Figure 4.48, a FEG-SEM micrograph of a CNT with a continuous coating via functionalized CNT route is seen. The excess amount of particles can be seen as agglomerates on the coating, however the coating consist of very fine particles. A BF-TEM micrograph in Figure 4.49 reveals the details of this continuous coating.

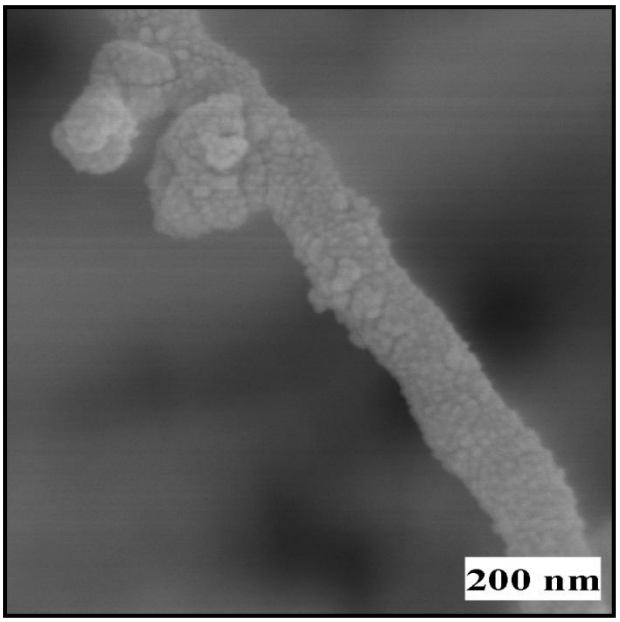

Figure 4.48 : FEG-SEM micrograph a CNT with a continuous coating via fCNT route.

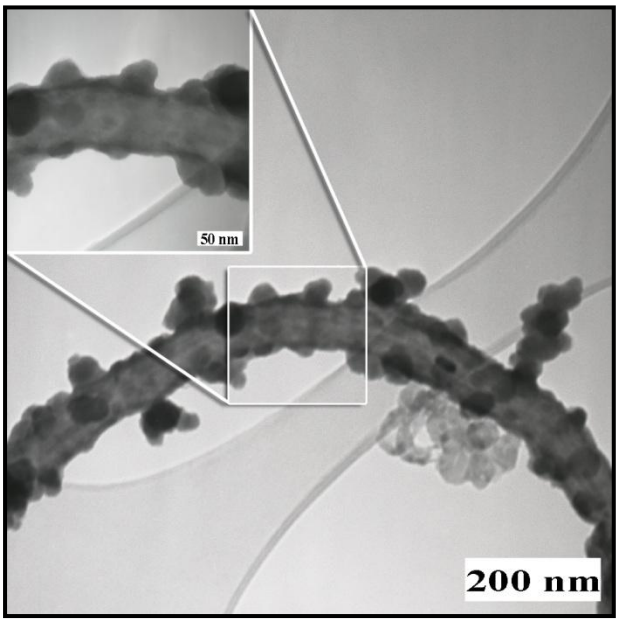

Figure 4.49 : BF-TEM micrograph a CNT with a continuous coating via fCNT route with higher magnification inset.

As clearly seen, the coating on the CNT is only 5-10 nm thick, although there are several particle agglomerates on the coating. Moreover, the coating seem to be tightly bonded on the CNT. The reason for this tight bonding is the covalent interaction of the carboxyl groups with the oxide particles via a W-O-C bond (Eder, 2010; Eder and Windle, 2008). This coating is obtained only with a 30% ethanol – 70% water solution. Other ratios did not lead to any coating using this processing route.

When the second route with the BA surfactant was followed, it was seen that the amount of ethanol has a crucial effect on the coating. In case of 5% ethanol addition to the solution in the BA route, there was a non-continuous coating observed, as shown in the FEG-SEM micrograph in Figure 4.50. The coating seem to peel off the CNT probably because of the insufficient interaction between the coating and the CNT. Presumably, BA acts as a weak surfactant and enhances the dispersion of pristine CNTs in the solution, which helps to achieve a uniform distribution of tungsten oxide particles. However, in case of deficient amount of ethanol in the solution, the dispersion of CNTs was hampered, which led to a non-continuous coating.

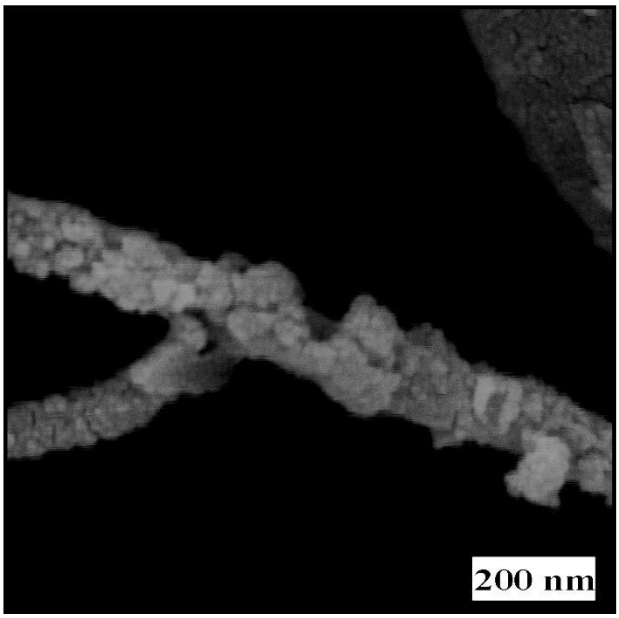

Figure 4.50 : FEG-SEM micrograph of a CNT with non-continuous coating via BA route.

If the amount of ethanol used in the solution was increased to 30% similar to fCNT route, then a continuous coating on CNTs can be observed as shown in Figure 4.51. Together with the BF-TEM micrograph shown in Figure 4.52, it can be clearly seen that the coating consists of very fine particles similar to the coating obtained in the fCNT route. However, particles in this coating seem to be kept together mechanically rather than chemically. Also, in Fig. 4.51, there is a region where the coating was broken indicating the weaker interaction between the CNTs and oxide particles, which is consistent with the study of Eder and Windle (2008). From this result, it can be assumed that this coating was formed via π-π interactions between the alcohol's benzene ring and the aromatic CNT surface. Then, the groups of BA would

coordinate with the tungsten and form a W-O-W network resulting a continuous coating.

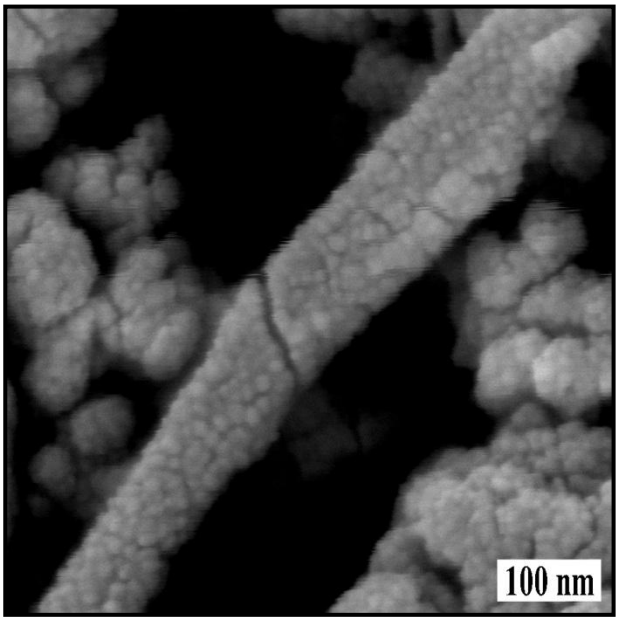

Figure 4.51 : FEG-SEM micrograph of a CNT with a continuous coating via BA route.

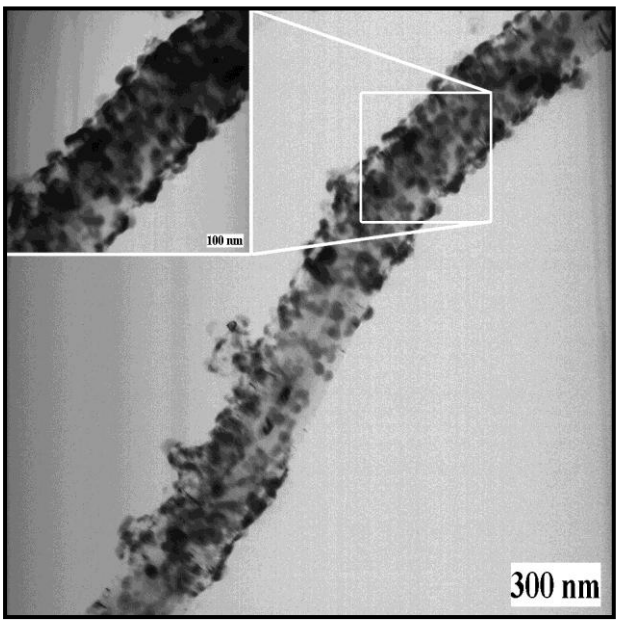

Figure 4.52 : BF-TEM micrograph of a CNT with a continuous coating via BA route with higher magnification inset.

Moreover, for both coating routes, similar type of XRD patterns shown in Figure 4.53 for coated CNTs has been obtained, where the peaks are broadened and the intensities decrease compared to pristine CNTs (Fig. 4.46b), probably because of the surface alterations of CNTs and the small grain sizes of the coating.

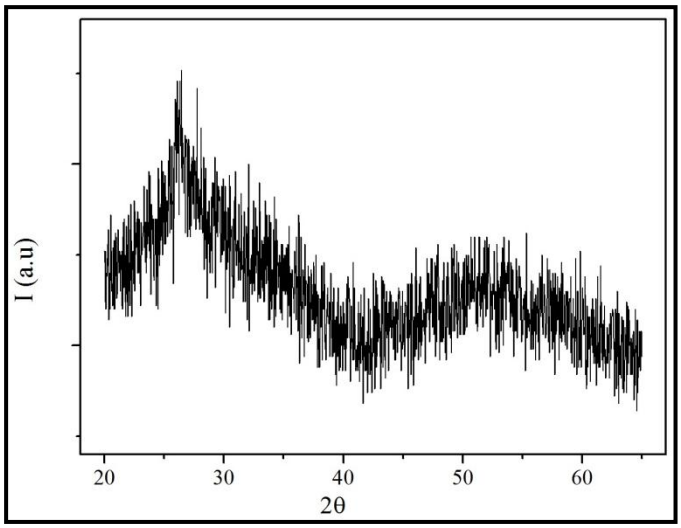

Figure 4.53 : Typical XRD pattern of a coated CNT.

In overall, it can be stated that pristine and functionalized CNTs were synthesized and characterized successfully. Following this, coatings of tungsten oxide particles were employed on CNTs via two different routes. In the first route, functionalized CNTs were used, whereas the other utilized pristine CNTs with BA as a surfactant. Both routes led to continuous coatings when a 30% ethanol – 70% water solution was used. As a result, this type hybrid materials can be interesting candidates for potential sensor applications instead of WO_x/CNT composites produced by Balazsi et al (2008) and Hashishin and Tamaki (2008) since the distributions of tungsten oxide and CNTs is much more homogenous and controllable than a similar WO_x/CNT composite.

4.3 W - Mn Matrix Composite System

This section is about the microstructural and physical characterization of W - Mn matrix composite powders and their sintered counterparts. The results are discussed regarding the effect of Mn amount and mechanical alloying duration on the microstructure, mechanical properties and sintering behavior of the composites.

4.3.1 Microstructural characterization of powders

XRD diffraction patterns of mechanically alloyed W1Mn2VC composite powders with W1Mn matrix alloy powders and W3Mn2VC composite powders with W3Mn matrix alloy powders are shown in Figures 4.54 and 4.55, respectively. As seen in both Figures, only the peaks of W (Bravais lattice: BCC; a = 0.316 nm; Space group:

Im$\bar{3}$m, ICDD Card No: 04-0806) are identified in all the samples. Peaks for VC and Mn are not seen, probably due to the small amount (2 wt.% and 1-3 wt.%, respectively) in the powder blend and also probably due to the broadening, which caused VC and Mn peaks to disappear in the background.

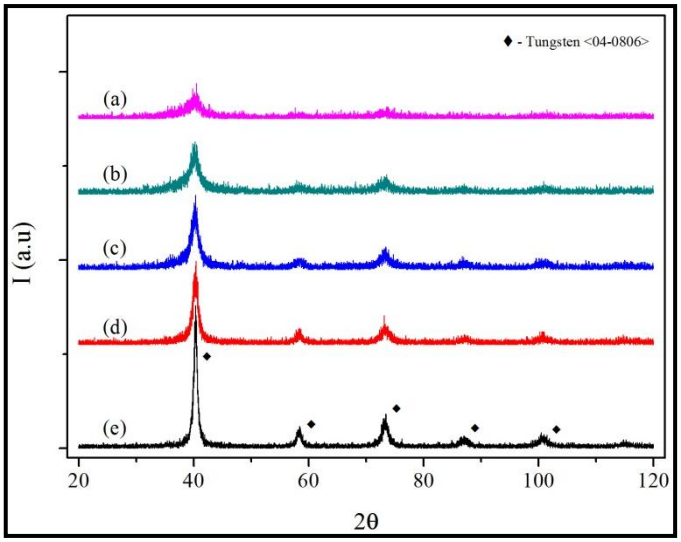

Figure 4.54 : XRD patterns of W1Mn2VC composite powders MA'd for; a) 24 h, b) 12 h, c) 6 h, d) 3 h and e) of W1Mn matrix alloy powders MA'd for 6 h.

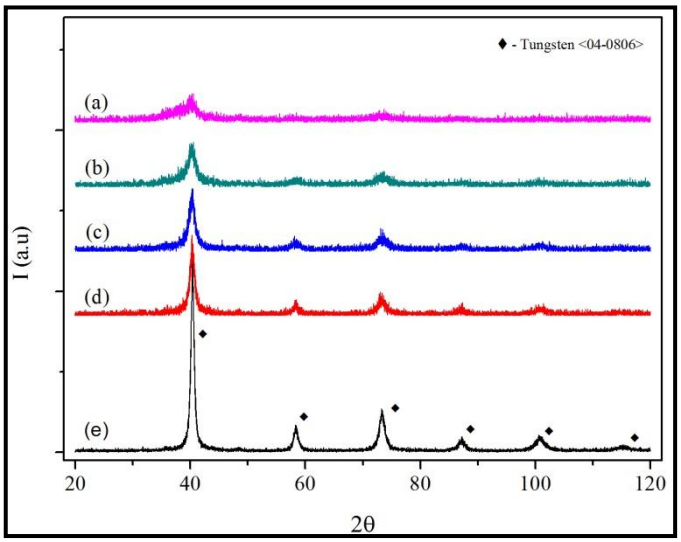

Figure 4.55 : XRD patterns of W3Mn2VC composite powders MA'd for; a) 24 h, b) 12 h, c) 6 h, d) 3 h and e) of W3Mn matrix alloy powders MA'd for 6 h.

Further, it is also clear that with increasing amount of MA, peaks are broadened and peak heights are decreased as a result of grain refinement and an increase in internal strain due to mechanical alloying. Figures 4.56a-4.56b show the particle size distributions of 6 h MA'd W1Mn matrix alloy powder with W1Mn2VC composite

powders MA'd for 3 h, 6 h, 12 h and 24 h, and of 6 h MA'd W3Mn matrix alloy powder with W3Mn2VC composite powders MA'd for 3 h, 6 h, 12 h and 24 h, respectively. According to these analyses, the median particle sizes of W1Mn and W3Mn matrix alloy powders drastically decrease to 453 nm and 481 nm after 6 h of MA, respectively. With increasing MA with VC, grain sizes further decrease to 191 nm and 183 nm for W1Mn2VC and W3Mn2VC composite powders MA'd for 24 h, respectively. Moreover, with increasing MA durations, an average specific surface area value of less than 1 m^2/g for as-blended matrix alloy powders increases to 14.5 m^2/g and 14 m^2/g for 6 h MA'd W1Mn and W3Mn matrix alloy powders, respectively. It further increases to 27.7 m^2/g and 29.9 m^2/g for W1Mn2VC and W3Mn2VC composite powders MA'd for 24 h, respectively.

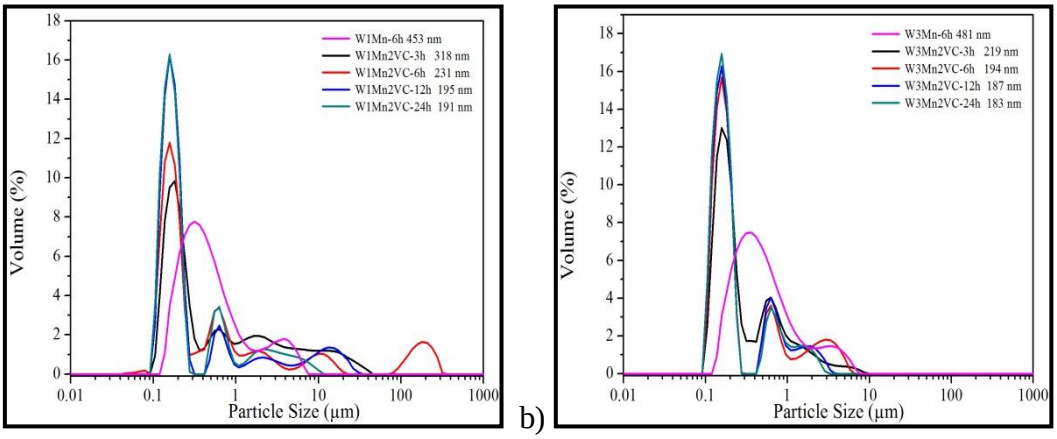

Figure 4.56 : Particle size distributions of MA'd powders of; a) 6 h MA'd W1Mn matrix alloy powder with W1Mn2VC composite powders MA'd for 3 h, 6 h, 12 h and 24 h and b) 6 h MA'd W3Mn matrix alloy powder with W3Mn2VC composite powders MA'd for 3 h, 6 h, 12 h and 24 h.

Figure 4.57 shows the dependence of the grain size of W grains as a function of the MA duration in as-blended W1Mn and W3Mn matrix alloy powders (no MA), in W1Mn and W3Mn matrix alloy powders MA'd for 6 h (MA'd for 6 h in total) and in W1Mn2VC and W3Mn2VC composite powders MA'd for 3 h (MA'd for 9 h in total), 6 h (MA'd for 12 h in total), 12 h (MA'd for 18 h in total) and 24 h (MA'd MA'd for 30 h in total). According to this, the average grain size of W (~400 nm) in as-blended W1Mn and W3Mn matrix alloy powders decreases rapidly to about 66.6 nm for W3Mn matrix alloy powders and 41.4 nm for W1Mn matrix alloy powders after MA for 6 h and it is about 3.2 nm and 2.2 nm for W3Mn2VC and W1Mn2VC composite powders after MA for 24 h, respectively. The particle sizes of the

W1Mn2VC and W3Mn2VC composite powders slightly change after 6 h of MA while the grain sizes exponentially decrease with increasing amount of MA and these results are consistent with the XRD patterns in Figures 4.54 and 4.55, which indicate a continuous decrease in grain sizes due to broadening.

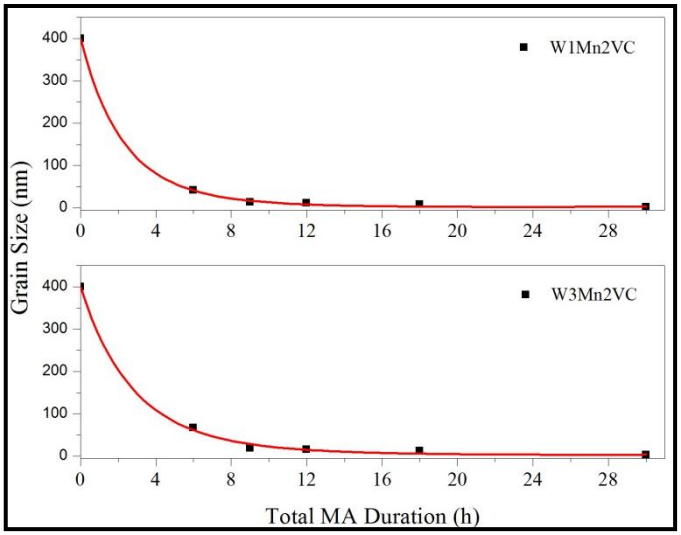

Figure 4.57 : Evolution of the grain size of W as a function of the MA time in as-blended W1Mn and W3Mn powders (no milling), in W1Mn and W3Mn matrix alloy powders MA'd for 6 h (MA'd for 6 h in total) as well as in W1Mn2VC and W3Mn2VC powders MA'd for 3 h (MA'd for 9h in total), 6 h (MA'd for 12 h in total), 12 h (MA'd for 18h in total) and 24 h (MA'd for 30h in total).

Figures 4.58a, 4.58b and 4.58c are the FEG-SEM micrographs taken from as-blended powders as well as W1Mn2VC and W3Mn2VC composite powders MA'd for 24 h, respectively. EDS spectra taken from the as-blended powders revealed that spherical shaped particles are W particles while flat-like particles are Mn particles, as shown in Fig. 4.58a. Consistent with particle size distributions in Fig. 4.56, it is quite clear that the powder particle sizes decrease by orders of magnitude (from micrometer to nanometer scales) after mechanical alloying. In Figs. 4.58b and 4.58c, it can be seen that individual particles sizes range from 100 nm to 200 nm. Moreover, some local agglomerations (Figs. 4.58b-4.58c) are detected which were formed because of the decreasing particle sizes and increasing surface areas. The amount of agglomeration seems to be increased in W3Mn matrix alloy powder because of the increased amount of Mn, which is a more ductile phase compared to W.

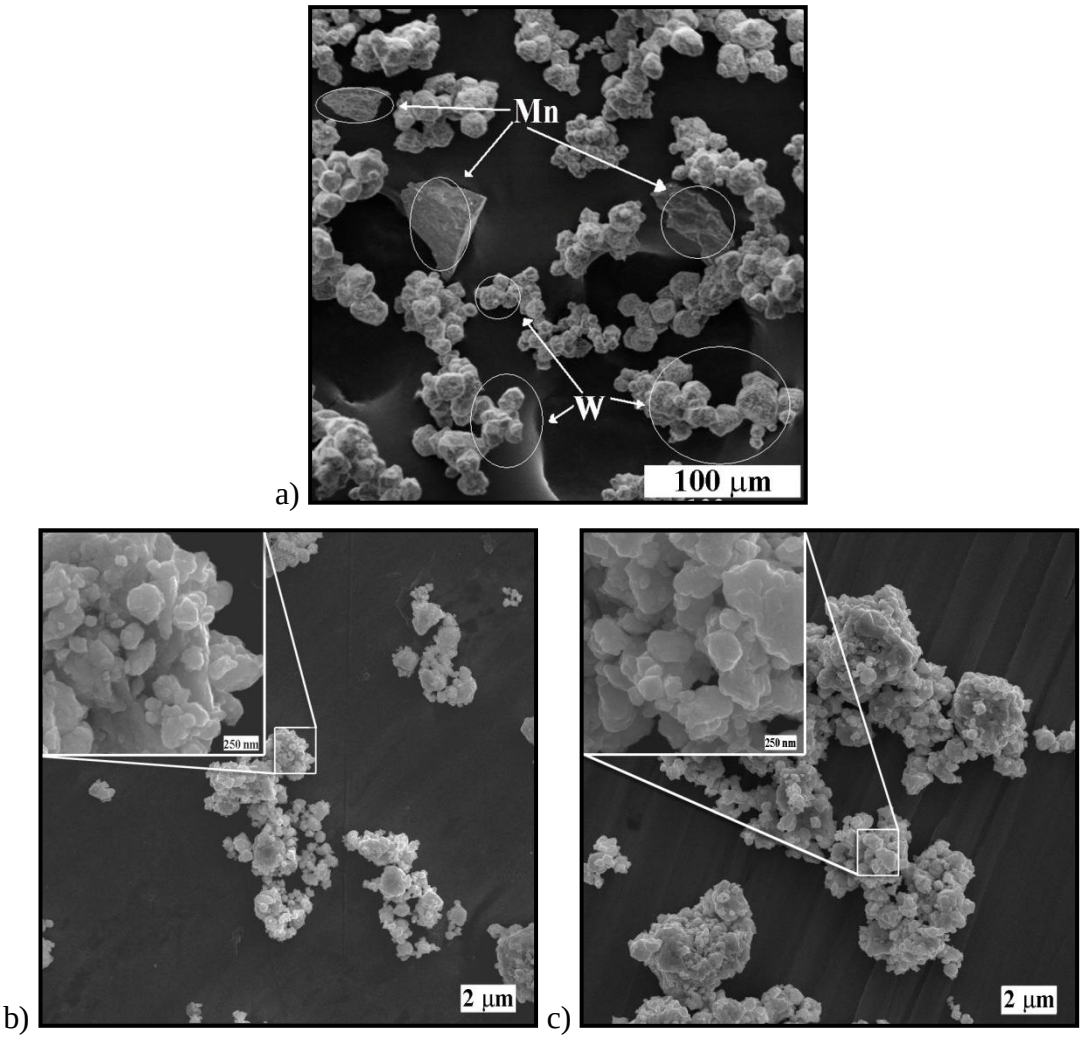

a) b) c)

Figure 4.58 : FEG-SEM micrographs of a) as-blended powders, b) W1Mn2VC composite powders MA'd for 24 h and c) W3Mn2VC composite powders MA'd for 24 h**.**

4.3.2 Microstructural characterization of the sintered samples

Figures 4.59 and 4.60 are the respective XRD patterns showing the effect of MA duration taken from the sintered W1Mn2VC and W3Mn2VC composite samples MA'd for 3 h, 6 h, 12 h and 24 h. As clearly seen in Fig. 4.6, a W_2C phase is identified in all the W1Mn2VC composite samples (Bravais lattice: Simple hexagonal; a=0.519 nm; c=0.472 nm; Space group: $\bar{3}$m1; ICDD Card No: 79-0743). Moreover, there is also a different W_2C phase ((Bravais lattice: Simple orthorhombic; a = 0.472 nm, b = 0.603 and c = 0.518 nm; Space group: Pbcn; ICDD Card No: 65-8829) identified only in the W1Mn2VC sample MA'd for 24 h, although it is observed in all the W3Mn2VC samples in Fig. 4.60. In addition to these, a manganese carbide ($Mn_{23}C_6$) phase (Bravais lattice: FCC; a = 1.06 nm;

Space group: $Fm\bar{3}m$; ICDD Card No: 80-1701) is identified in all the W1Mn2VC and W3Mn2VC samples. Moreover, a complex manganese tungsten carbide (Mn_3W_3C) phase (Bravais lattice: FCC; a = 1.11 nm; Space group: $Fd\bar{3}m$; ICDD Card No: 89-4882) is observed in the sintered W3Mn2VC composite sample MA'd for 24 h. On the other hand, all the peaks indexed with an arrow are from the Struers^{TM} MultiFast Bakelite resin, which was used for routine metallographic mounting of samples. The presence of manganese carbide and tungsten manganese carbide phases in the samples is considered to refer to transient LPS, where the liquid phase disappears during sintering cycle due to the dissolution into the solid or formation of new phase (German et al, 2009).

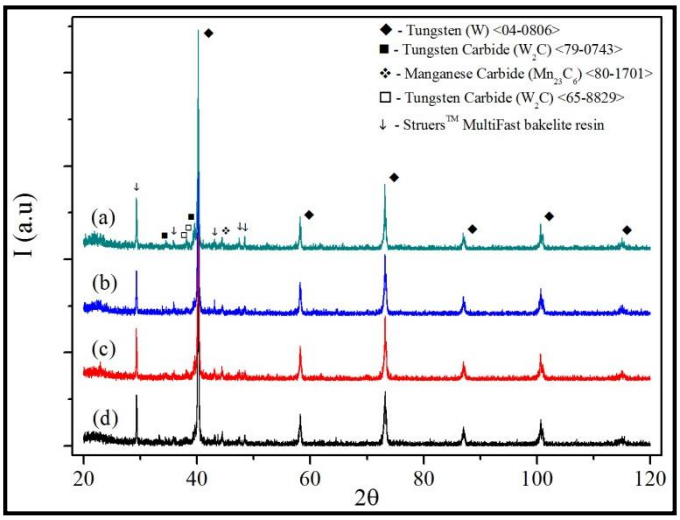

Figure 4.59 : XRD patterns of sintered W1Mn2VC composites MA'd for; a) 24 h, b) 12 h, c) 6 h and d) 3 h.

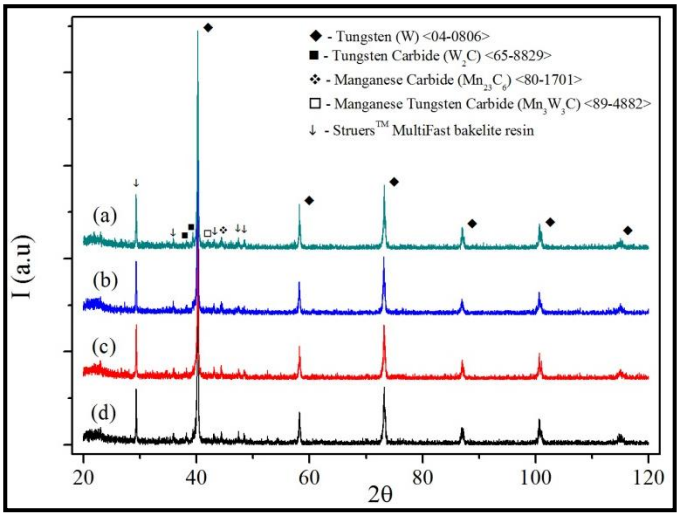

Figure 4.60 : XRD patterns of sintered W3Mn2VC composites MA'd for; a) 24 h, b) 12 h, c) 6 h and d) 3 h.

Typical SEM-SEI micrographs of the sintered W1Mn2VC composite samples are shown in Figs. 4.61a-4.61d.

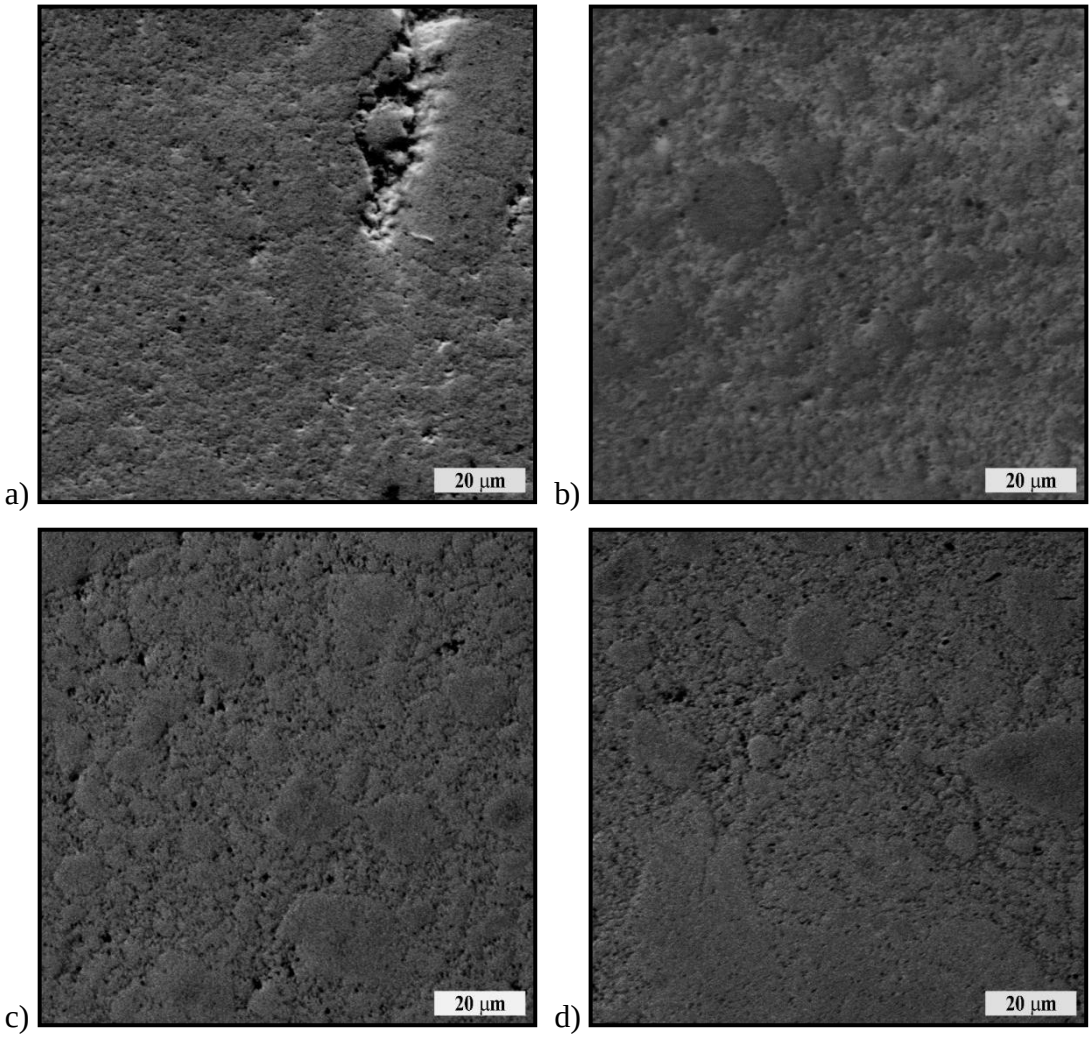

Figure 4.61 : SEM-SEI micrographs taken from sintered W1Mn2VC composite samples MA'd for; a) 3 h, b) 6 h, c) 12 h and d) 24 h.

As clearly seen, all the W1Mn2VC composite samples have a non-uniform microstructure, where the grains quietly differ in size and shape from each other. Moreover, the sample MA'd for 3 h has big cracks and some pores beside the inhomogeneous microstructure, which is considered as a consequence of insufficient sintering. EDS analyses revealed that the plain and brighter regions in the micrographs are Mn rich grains and the darker ones are Mn poor areas where insufficient sintering occurred. Although still inhomogeneous, the amount and sizes of Mn rich grains increase with increasing amount of MA, which caused relatively better distribution of Mn.

Figure 4.62 is a SEM-SEI micrograph showing the Vickers Microhardness marks on the W1Mn2VC composite sample MA'd for 24 h. As a result of non-uniform microstructure of W1Mn2VC composite samples, there is a big difference in sizes of microhardness marks from different regions/grains even in W1Mn2VC composite sample MA'd for 24 h.

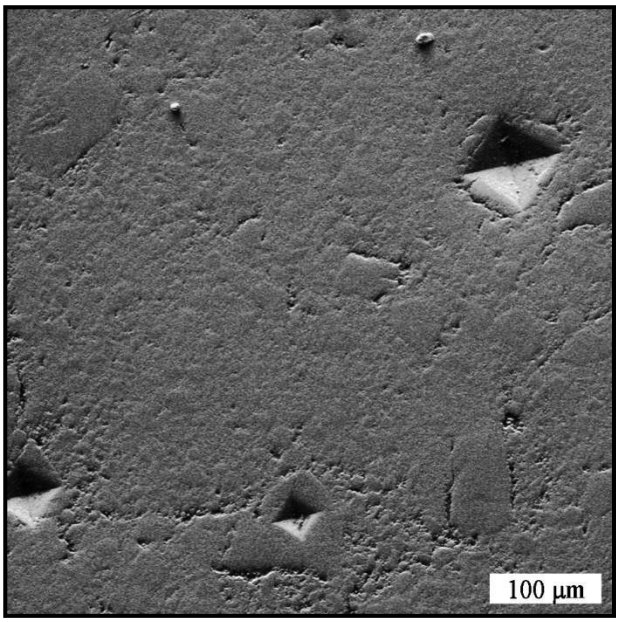

Figure 4.62 : Vickers Microhardness marks on the W1Mn2VC composite sample MA'd for 24 h.

Typical SEM-SEI micrographs of the sintered W3Mn2VC composite samples are shown in Figures 4.63a-4.63d. Contrary to the sintered W1Mn2VC composite samples, the sintered W3Mn2VC composite samples have a fine and homogenous microstructure, possess low amount of pores or cracks and their grain sizes are approximately a few micrometers. These microstructures resemble those observed in the study of Zaharee et al (2008), who reported comparable microstructures with increasing amount of Mn in W-Mn/Ni samples. Similar to the study of Zaharee et al (2008), it is likely that the extra Mn prevented very effectively the coarsening of the W grains due to mutual insolubility of W and Mn. In addition, Mn distribution in the sintered W3Mn2VC samples is homogeneous according to the EDS analyses, which is consistent with the homogeneous microstructure due to sufficient sintering.

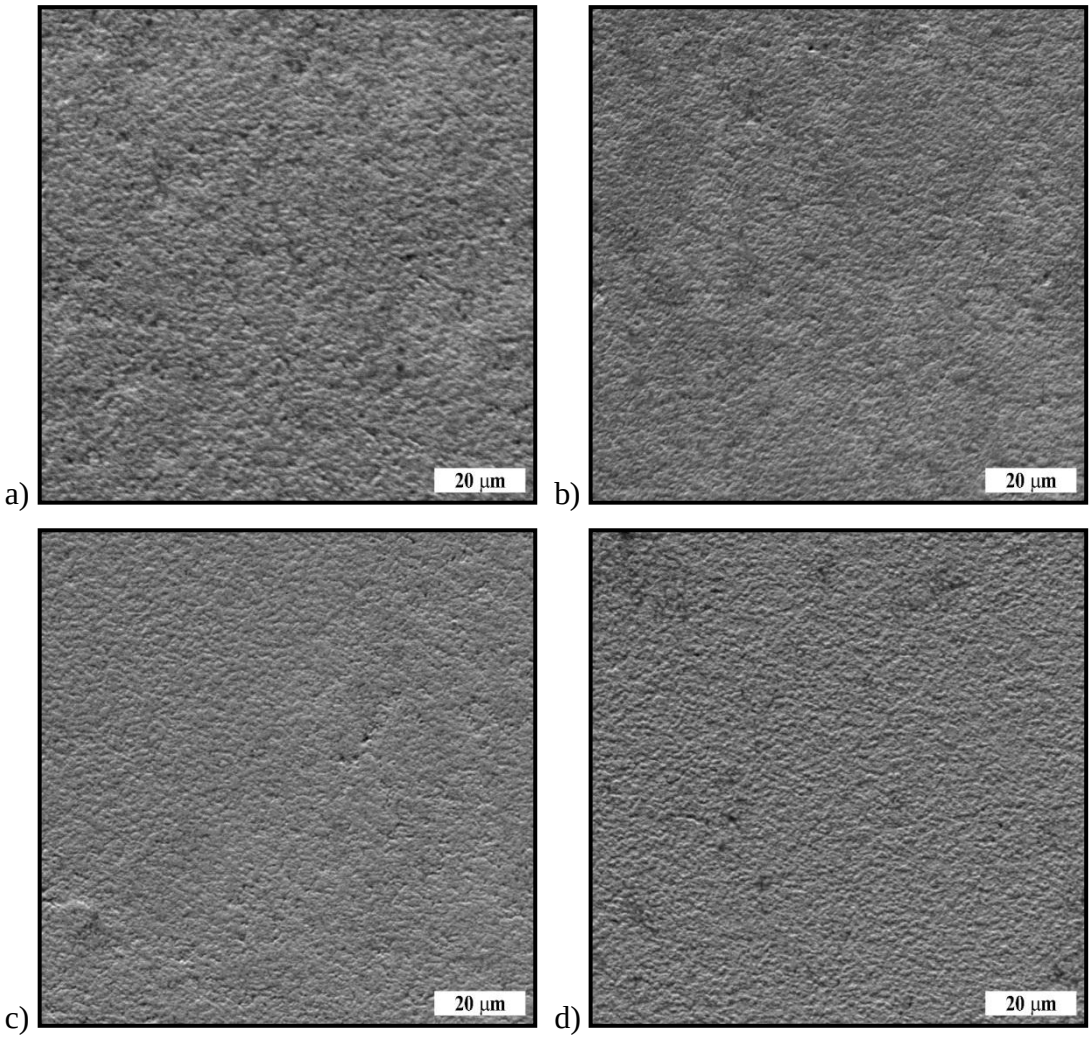

Figure 4.63 : SEM-SEI micrographs taken from sintered W3Mn2VC composite samples MA'd for; a) 3 h, b) 6 h, c) 12 h and d) 24 h.

Sintered W3Mn2VC samples were fractured manually in order to get a better evaluation about fine microstructural features in the bulk of the samples. Figure 4.64 shows the SEM-SEI fractographs of the sintered W3Mn2VC composite samples. According to these micrographs, grains of the W3Mn2VC samples MA'd for 3 h, 6 h and 12 h have sizes around 1-2 μm and among all others, the sample MA'd for 24 h has a very fine microstructure with typical grain sizes varying from a couple of hundreds of nanometers to a max of ~1 μm. Generally, the grains of all sintered W3Mn2VC samples possess polygonal shapes, typical for tungsten alloys and composites. There is also a small amount of sinter pores in all sintered W3Mn2VC composite samples. Furthermore, these fractographs revealed that the dominant fracture mode is intergranular, with fracture at grain boundaries and sinter pores, for the W3Mn2VC samples MA'd for 3 h, 6 h and 12 h. On the other hand, the

W3Mn2VC sample MA'd for 24 h display characteristics of both intergranular and transgranular fracture.

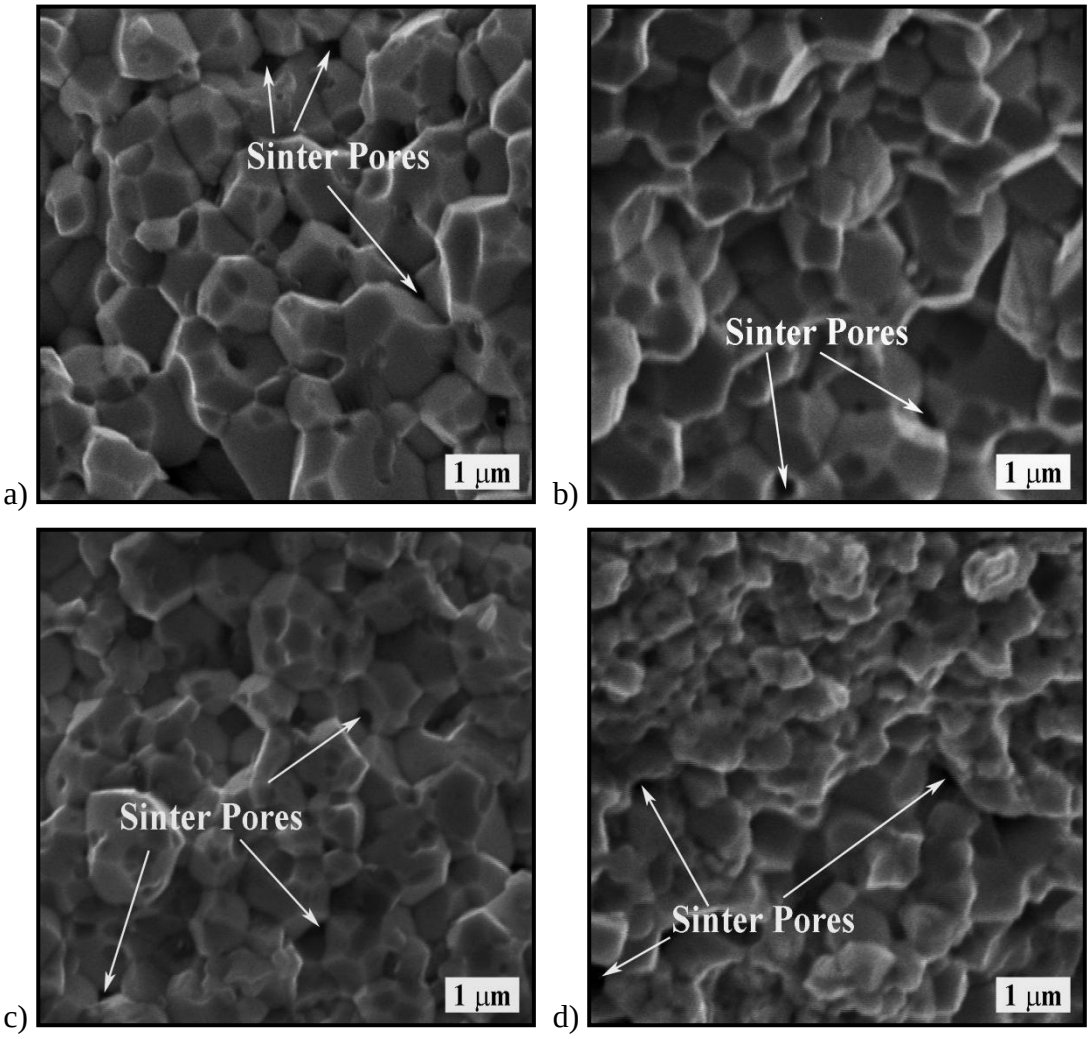

Figure 4.64 : SEM-SEI micrographs of fracture surfaces taken from sintered W3Mn2VC composite samples MA'd for; a) 3 h, b) 6 h, c) 12 h and d) 24 h.

Figure 4.65 shows the SEM-BEI micrographs taken from the fracture surfaces of the sintered W3Mn2VC composite samples. EDS spectra taken from different locations of all fractographs revealed that the black regions are sinter pores, dark gray particles are VC and large light gray regions are $Mn_{23}C_6$ (or/and Mn_3W_3C for the W3Mn2VC sample MA'd for 24 h). Needless to mention that the EDS spectra taken from all white grains have W-rich chemistry, as expected. According to these, VC particles are mainly located at quadruple grain or triple grain junctions in the sintered W3Mn2VC composite samples MA'd for 3 h, 6 h and 12 h. They possess particle sizes of max. ~500 nm. On the other hand, VC particles in the sintered W3Mn2VC

composite sample MA'd for 24 h are mostly retained and homogeneously dispersed inside the W-rich grains and have very small particle sizes of less than ~50 nm.

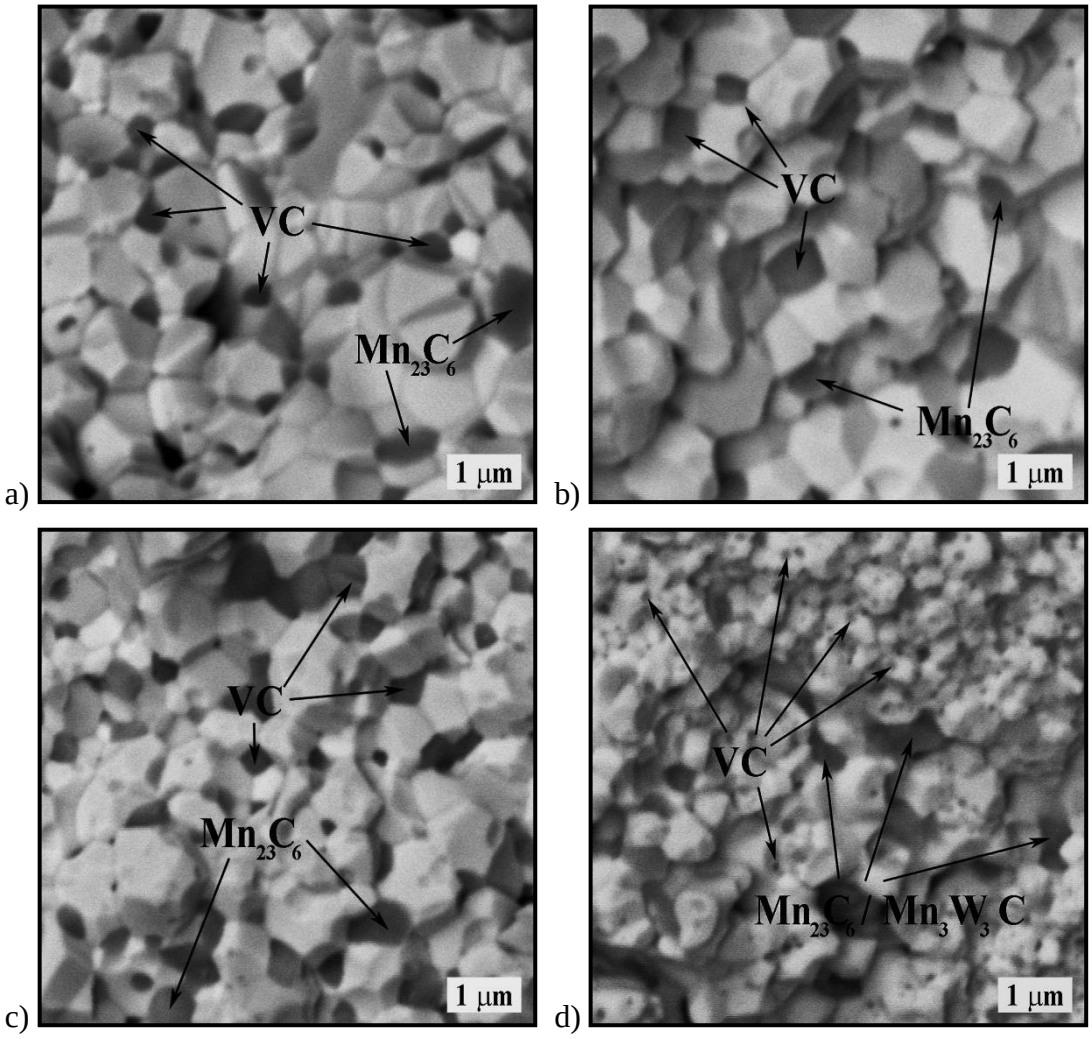

Figure 4.65 : SEM-BEI micrographs of fracture surfaces taken from sintered W3Mn2VC composite samples MA'd for; a) 3 h, b) 6 h, c) 12 h and d) 24 h.

In addition to these, fracture surfaces of sintered W3Mn2ZrC composites mechanically alloyed for 6 h and 24 h were also investigated for comparison. Figure 4.66 shows the SEM-SEI fractographs of the sintered W3Mn2ZrC composite samples. According to these micrographs, the microstructure of W3Mn2ZrC composite samples resembles the microstructure of W3Mn2VC samples, where the grains of the samples generally possess polygonal shapes. However, W3Mn2ZrC sample MA'd for 6 h has biggest grain sizes of ~2 μm or more among all W3Mn matrix composites, while W3Mn2ZrC sample MA'd for 24 h possess very fine microstructure similar to that of W3Mn2VC composite sample MA'd for 24 with

typical grain sizes below 1 μm. By comparing W3Mn matrix composite systems reinforced with VC and ZrC, one can deduce that 24 h of mechanical alloying is adequate for achieving very fine microstructures in W3Mn matrix composite systems.

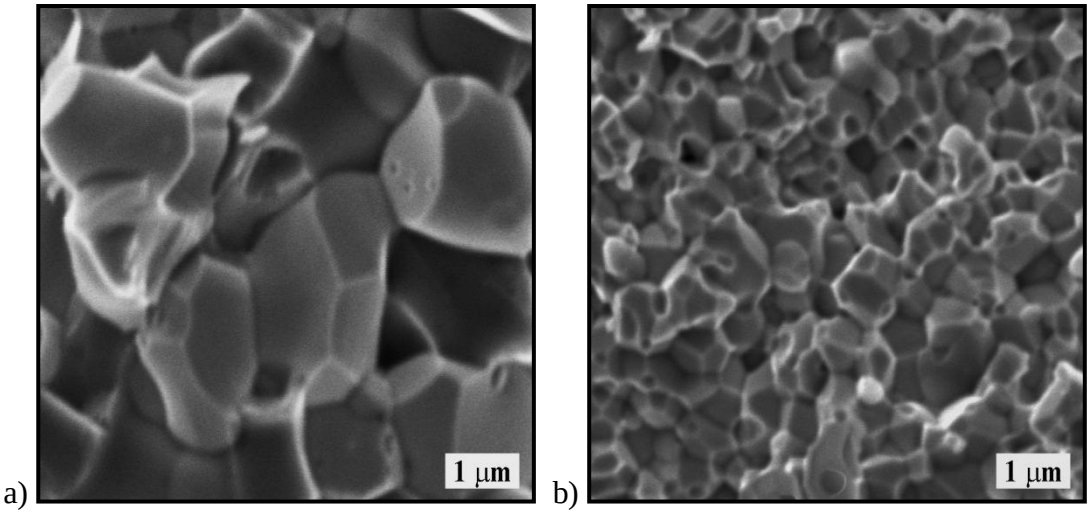

Figure 4.66 : SEM-SEI micrographs of fracture surfaces taken from sintered W3Mn2ZrC composite samples MA'd for; a) 6 h and b) 24 h.

4.3.3 Physical properties of sintered composites

Relative density results together with Vickers microhardness values of the sintered W1Mn2VC and W3Mn2VC composite samples are given in Figures 4.67 and 4.68, respectively.

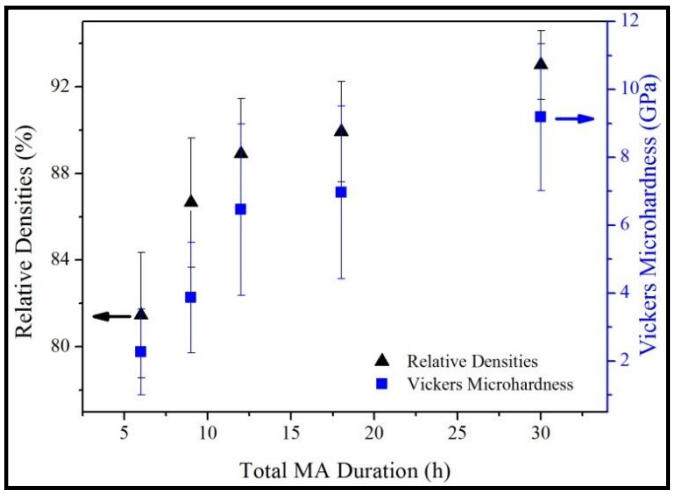

Figure 4.67 : Relative density and Vickers microhardness results vs. total MA duration of the sintered W1Mn matrix alloy sample MA'd for 6 h (MA'd for 6 h in total) with the sintered W1Mn2VC composite samples MA'd for 3 h (MA'd for 9 h in total), 6 h (MA'd for 12 h in total), 12 h (MA'd for 18 h in total) and 24 h (MA'd for 30 h in total).

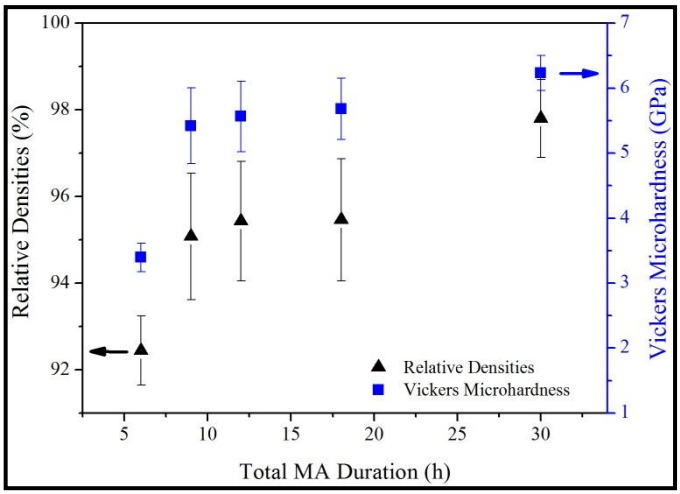

Figure 4.68 : Relative density and Vickers microhardness results vs. total MA duration of the sintered W3Mn matrix alloy sample MA'd for 6 h (MA'd for 6 h in total) with the sintered W3Mn2VC composite samples MA'd for 3 h (MA'd for 9 h in total), 6 h (MA'd for 12 h in total), 12 h (MA'd for 18 h in total) and 24 h (MA'd for 30 h in total).

As seen in both Figures, the relative density and hardness values of the both sintered W1Mn2VC and W3Mn2VC composite samples correlate very well with each other. Moreover, the addition of VC drastically increases both values for W1Mn2VC and W3Mn2VC composite samples. The relative density value of sintered W1Mn matrix alloy sample without any VC addition increases from ~81% to about 86% for the sintered W1Mn2VC composite sample MA'd for 3 h, while the relative density value of the sintered W3Mn matrix alloy sample without any VC addition increases from ~92% to around 95% for the sintered W3Mn2VC composite sample MA'd for 3 h. Similarly, there is a remarkable increase of ~70% and ~60% in hardness values of the sintered W1Mn2VC and W3Mn2VC composite samples MA'd for 3 h, respectively, when compared to the sintered W1Mn and W3Mn matrix alloy samples without any VC addition. However, as clearly seen from both Figures, density results of W1Mn2VC samples are more dependent to the MA duration than those of W3Mn2VC samples are. Actually, this result is consistent with the study of Coşkun et al (2009), where the density results barely changed with MA duration. In the presence of a sufficient amount of a sintering aid, the dominant effect of MA to the sintering process diminished (Coşkun et al, 2009). On the contrary; in the W1Mn2VC composite system, MA duration became the dominant effect during the sintering process because of the insufficient amount of Mn resulting that the relative densities in the W1Mn2VC samples remarkably increased from 86% for W1Mn2VC

composite sample MA'd for 3 h to 93% for W1Mn2VC composite sample MA'd for 24 h. Moreover, the standard deviation values of the density results in the W1Mn2VC samples decrease with MA duration due to increasing homogenization of the microstructure and better distribution of Mn in the structure. Similar to the relative densities, also the hardness results of the W1Mn2VC samples are more dependent to the MA duration than W3Mn2VC samples are. Moreover, the high standard deviation values for microhardness results in the W1Mn2VC samples are consistent with the SEM micrographs (Figs. 4.61 and 4.62) where the samples have a non-uniform microstructure. However, these high standard deviation values decrease with MA duration from 42% for W1Mn2VC composite sample MA'd for 3 h to 23% for W1Mn2VC composite sample MA'd for 24 h, while hardness values increase from 3.86 GPa to 9.18 GPa for W1Mn2VC samples. Although there is an almost 300% increase in the hardness values of the W1Mn2VC composite samples, non-uniform microstructures resulting high standard deviation values and low relative densities make this system unfavorable for any potential application.

On the other hand, W3Mn2VC composite system reveals promising results. The microhardness values slightly increase and the relative density values barely change in the W3Mn2VC samples between 3 h and 12 h of mechanical alloying and both values increase noticeably in the sample MA'd for 24 h. Thus, among all the sintered W3Mn2VC samples, the W3Mn2VC composite sample MA'd for 24 h has the highest relative density and microhardness values of 97.8% and 6.23 GPa, respectively. Especially, the increase in hardness value for the sintered W3Mn2VC composite sample MA'd for 24 h corresponds to an increase of approximately 85%. Normally, powder mixtures should contain min. 15 wt.% (30 vol% for systems having low mutual solubility) liquid phase (German et al, 2009; Kim et al, 1998; Johnson and German, 1994; Ibrahim et al, 2009; Dore et al, 2004) to yield complete densification. Although only 3 wt.% Mn is used in the present system, high relative density values (>95%) are on account of fairly good homogenization and distribution of Mn in the sintered W3Mn2VC composite samples resulted from mechanical alloying. Besides, these high relative densities might be also associated to the activation effect of Mn on tungsten densification even though it is not comparable to Pd or Ni (Corti, 1986). Considering that very small amount of Mn has been used in this work, it might also possible that some kind of an activated liquid phase sintering

has been involved during the consolidation process of the composites. However, a detailed investigation on this consideration would be off the topic for this work.

On the other hand, fluctuations in the theoretical density values could be expected when the formation of some new phases (W_2C, $Mn_{23}C_6$ etc.) has been taken into account after sintering. However; especially for W3Mn2VC composite samples, both the high microhardness values (Fig. 4.67) and SEM-SEI micrographs (Figs. 4.63-4.65) containing no or very low amount of sinter pores can be considered as a solid evidence for small or no density fluctuations and that these fluctuations, if any, would not cause any dramatic change in the morphological and mechanical properties of the W3Mn2VC composites. Moreover, in correlation with the SEM micrographs depicting uniform microstructures for the sintered W3Mn2VC composite samples, small standard deviations varying from 4% to 10% for the microhardness results are evidence for good Mn distribution. In addition, these low standard deviation values and homogenous microstructure of the W3Mn2VC samples might be attributed to orthorhombic W_2C phase formed during sintering different from the hexagonal W_2C phase formed in the W1Mn2VC samples. Supporting this idea, only in the 24 h MA'd sample among the W1Mn2VC samples, which had the lowest standard deviation values for both density and hardness results, this orthorhombic W_2C phase was formed beside the hexagonal W_2C phase. However, this point needs to be investigated deeply, which is out of the scope of the present dissertation work.

On the other hand, noticeable increases in the relative density and microhardness values for the sample MA'd for 24 h are believed to be contributed also by the uniform distribution of the nanosized carbide phases in the matrix as well as the refinement in the microstructure. Generally, a high elastic modulus of the strengthening particles (VC in this case) enables the particles to carry more stress than the matrix when exposed to the same strain, which contributes to the strengthening of the composite via load transferring mechanism (Chen et al, 2008). Moreover, the intergranular-to-transgranular change in the fracture mechanism is also believed to have a positive effect on the sudden increment of the microhardness value of the sintered W3Mn2VC composite sample MA'd for 24 h.

In addition to these, W3Mn matrix composites reinforced with ZrC instead of VC were also investigated by means of relative density and microhardness for comparison. Below is the Table 4.4, where the relative density and micro hardness results of W3Mn2VC and W3Mn2ZrC composite samples MA'd for 6 h and 24 h are compared.

Table 4.4 : Comparison between W3Mn2VC and W3Mn2ZrC composite samples both MA'd for 6 h and 24 h.

Sample	MA Duration (h)	Hardness (GPa)	Relative Density (%)
W3Mn2VC	6	5.57 ± 0.54	95.43 ± 1.38
	24	6.23 ± 0.26	97.80 ± 0.90
W3Mn2ZrC	6	4.73 ± 0.34	94.23 ± 1.69
	24	6.11 ± 0.28	96.92 ± 1.20

As clearly seen, both the microhardness and relative density results of W3Mn2ZrC composite samples increase with increasing amount of MA similar to W3Mn2VC samples. However, both values are lower than those of W3Mn2VC samples. While the increase in microhardness of W3Mn2VC is about 12%, it increases for an amount of 30% in the W3Mn2ZrC samples with increasing MA duration. Actually, this result is in consistency with the SEM micrographs (Figs. 4.66a and 4.66b) which reveal that the amount of microstructure refinement in the W3Mn2ZrC samples is higher than that in W3Mn2VC samples. Moreover, W3Mn2ZrC samples have small standard deviations varying from 5% to 7% for the microhardness results, which are also similar to W3Mn2VC composite samples. Additionally, high relative densities with very small standard deviations of 1-2% together with these hardness results indicate homogenous microstructures in accordance with SEM micrographs shown in Fig. 4.66.

Overall, these hardness and relative density results are comparable or sometimes better than the similar systems in the literature (Song et al, 2002; Song et al, 2003) although conventional consolidation methods were used in this work. For instance, Song et al 2002 reported a microhardness value of 5.77 GPa for a W-30 vol.% ZrC (equivalent to around 13 wt.%) composite produced via hot pressing at 2000°C/1h. In another study, Song et al (2003) reported a microhardness value of about 7.6 GPa and an approximate density value of 97% for a W matrix composite reinforced with 20 vol.% TiC (equivalent to around 4 wt.%) particles fabricated via hot pressing at

2000°C/1h. Similar to present work, Genç et al (2010) reported a relative density of 93.3% and a Vickers microhardness of 7.1 GPa for a W - 5 wt.% TiC + 1 wt.% Ni composite. Moreover, the hardness value of the W3Mn matrix alloy sample (3.40 GPa) without any VC addition is as high as those (2.65 GPa - 3.82 GPa) of sintered tungsten samples activated with different activating agents, such as Fe, Co, Ni, Ru, Rh, Pd and Pt (Corti, 1986) as well as those (2.45 GPa - 3.43 GPa) of conventional W-Fe-Ni heavy alloys (Kim et al, 1998; Upadhaya et al, 2007).

In addition to relative density and microhardness measurements, sliding wear resistances of W3Mn2VC and W3Mn2ZrC composite samples were also investigated. Figure 4.69 and Table 4.5 show the wear amounts and the friction coefficient values of the sintered W3Mn2VC as well as W3Mn2ZrC composite samples, respectively.

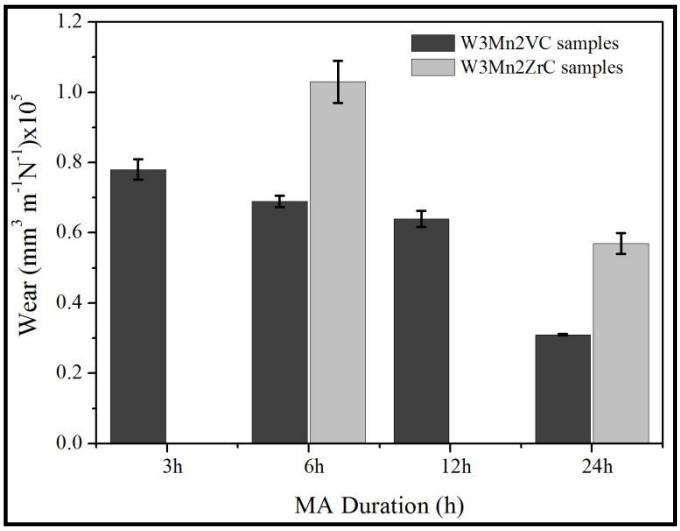

Figure 4.69 : Wear amounts of W3Mn2VC and W3Mn2ZrC composite samples.

Table 4.5 : Friction coefficients of the W3Mn2VC and W3Mn2ZrC samples.

Sample	MA Duration (h)	Min. friction coefficient	Max. friction coefficient	Mean friction coefficient
W3Mn2VC	3	0.107	0.547	**0.438**
	6	0.094	0.492	**0.421**
	12	0.068	0.464	**0.361**
	24	0.067	0.377	**0.340**
W3Mn2ZrC	6	0.073	0.505	**0.443**
	24	0.052	0.508	**0.429**

It is generally not reliable to compare friction results with the literature because it is well known that friction coefficient is not a natural property of a material, but depends on the friction system, test parameters (including test loads and sliding

speed) and environment (Lv et al, 2007). Therefore, wear resistances obtained in this work is for comparison among the composite samples, only.

As clearly seen, wear amounts of the both W3Mn2VC and W3Mn2ZrC composites decline with increasing amount of MA. Mean friction coefficient results are also proportional to the wear amounts, where they decrease with increasing MA amount. Moreover, these results are fairly in consistence with microhardness results. The wear amounts of W3Mn2VC composites slightly decrease between 3 h and 12 h of mechanical alloying and it decreases noticeably in the sample MA'd for 24 h, which is inversely proportional to microhardness results. In addition, wear amounts of W3Mn2VC composites MA'd for 6 h and 24 h are distinctly lower than those of W3Mn2ZrC composites. W3Mn2VC composite sample MA'd for 24 h possess the lowest wear amount with the lowest standard deviation value inversely proportional to its highest microhardness and relative density values.

Comparing these wear amounts with the microhardness, relative density and microstructures of the composites, it is evident that increasing MA amount improves the mechanical as well as the microstructural properties of W3Mn matrix composites. All things considered; among all others, W3Mn2VC composite sample MA'd for 24 h achieves to combine promising characteristics, like high hardness and wear resistance, high relative density as well as a homogenous and very fine microstructure into a single material.

5. CONCLUSIONS AND SUGGESTIONS FOR FUTURE WORK

5.1 Conclusions

This dissertation work focused on three different W-based material systems in terms of their production and characterization. The importance and major achievement of this work was due to the uniqueness of these different W-based systems in the sense of their production method and/or constituent elements used in.

In the first system, different tungsten borides were synthesized via mechanical alloying route. Firstly, a powder mixture of W + W_2B + WB was produced by mechanical alloying of $WO_{2.72}$, Mg and B_2O_3 powders for 30 h, followed by leaching in a 5 M HCl solution. A high yield in residual removal during leaching was achieved, although pure WB or W_2B phases could not be produced. Moreover, the formation of $Mg_3(BO_3)_2$ phase was observed when stoichiometrically excess amount of B_2O_3 was used. This minor phase could not be removed from the boride system by leaching. Secondly, pure W_2B_5 powders with an average particle size of 226 nm and an average grain size of 55.3 nm were successfully produced via mechanical alloying route for the first time in the literature. For the synthesis, $WO_{2.72}$, MgO and 50% stoichiometrically excess amount of B_2O_3 powders were mechanically alloyed for 30 h, followed by leaching with a 7 M HCl solution. However, the use of different amounts of B_2O_3 powders resulted the formation of some minor phases like $FeWO_4$ or $Mg_3(BO_3)_2$ which could not be removed from the system by leaching. The molar yield of the W_2B_5 synthesis was calculated as 89%. In all experiments for tungsten boride synthesis, stoichiometric excess (about 10 wt.%) amount of Mg was used to account for the surface oxidation of the metal and the residual oxygen that could be absorbed onto reactant surfaces and milling medium.

In the second system, WO_2 nanoparticles, nanorods and nanowires as well as WO_2/CNT hybrid materials were synthesized. First, clusters of partially crystallized WO_2 nanopowders were produced via a novel water assisted method developed by the present researcher (author) for the first time, in which appropriate amounts of

WCl_6 and $NaBH_4$ were simply ultrasonicated in water for 3 h. The yield of the process was around 90%. Fully crystallized nanopowders without any morphological change and an average diameter of 37 nm were obtained after annealing at 500 ^oC for 2 h. Bundles of WO_2 nanorods and nanowires with an average diameter of 60-70 nm were produced via annealing of the as-prepared WO_2 nanopowders at temperatures above 700 ^oC under Ar for 6 h. The lengths of nanowires increased from several 100 nm up to several 10 µm after annealing at 1000 ^oC, whereas the small diameters of 60-70 nm remained unchanged. Moreover, these nanowires were pretty elastic in nature and had wool or cotton like fabric, which was very different from the nature of nanoparticles annealed at lower temperatures. Although the formation mechanism for the nanorods has not been clearly understood yet, a root growth mechanism from a parent structure was proposed, in which first the nucleus sites of WO_2 nanocrystallites were assembled and then leading individual nanorods rooted from these parent structures followed by the growth of thickness via root growth of secondary rods parallel to the primary rod forming bundles of nanorods. Finally, CNT hybrids were prepared by coating of WO_2 nanoparticles on functionalized and pristine CNTs. For both type of CNTs, a 30% ethanol - 70% water solution led to continuous coatings, however, weaker interaction between the CNTs and oxide particles was obtained when pristine CNTs were used for coating.

In the third system, W-Mn matrix composites reinforced with VC were synthesized by mechanical alloying for different durations and sintering at 1300 ^oC under Ar and H_2 for 1 h. In some experiments, ZrC was also used as a reinforcement agent for comparison. It was clearly shown that increasing amount of Mn and mechanical alloying duration improved the mechanical and microstructural properties of the W-Mn matrix composites. Although there was an almost 300% increase (from 3.86 GPa to 9.18 GPa) in the hardness values of the W - 1 wt.% Mn - 2 wt.% 2VC (W1Mn2VC) composite samples, non-uniform microstructures resulting high standard deviation values and low relative densities varying between 86% and 93% have made this system unfavorable for any potential application. On the other hand, composites containing 3 wt.% Mn revealed promising results, where the addition of VC improved the hardness, wear resistance and relative densities of the composites better than the ZrC addition. Among all others, W3Mn2VC composite sample MA'd for 24 h achieved to combine promising characteristics, like high hardness (6.23

GPa) and wear resistance, high relative density (97.8%) as well as a homogenous and very fine microstructure into a single material. Considering that a relatively low sintering temperature of 1300 ^{o}C and very low amount of liquid phase were used in sintering of the tungsten based composites, remarkable Vickers microhardness and relative density values were achieved.

In overall, this dissertation work was based on a comprehensive and detailed study on three W-based systems and revealed the first scientific data on the production of different tungsten borides (W_2B, WB and W_2B_5) and their mixtures via mechanical alloying, tungsten oxide (WO_2) nanostructures with CNT hybrid materials via a water assisted method and W-Mn matrix composites via mechanical alloying and conventional sintering.

5.2 Suggestions For Future Work

While this dissertation work provides insight into the production and characterization of three different W-based systems, opportunities remain for future work.

As one of the conclusions of this work is that the different tungsten borides and their mixtures can be synthesized by mechanical alloying of $WO_{2.72}$, Mg and B_2O_3 powders, it appears that this represents a topic worthy of further investigation. The mechanical alloying experiments discussed in this work could be repeated in the presence of a different reducing agent. For instance, it is theoretically possible to replace Mg with Al or Ca. Another attempt would be to arrange the stoichiometry of the powder blends to produce W_2B. Moreover, sintered counterparts could be produced from synthesized pure tungsten boride powders or powder mixtures using different consolidation and sintering techniques. Experiments may be performed to determine their physical and mechanical properties. Another avenue of study involves looking for the recovery possibilities of Mg and Fe elements from the leaching solutions, since substantial amounts of these elements are eliminated during leaching process of the boride powders.

Second system studied in this work was the tungsten oxide system, in which WO_2 nanoparticles, nanorods and nanowires as well as WO_2/CNT hybrid materials were synthesized. A comparative study can be made on the synthesis of tungsten oxide nanoparticles with different morphologies or crystal structures by changing the

process parameters. These may include experiments with different WCl_6 concentrations or $NaBH_4$ amounts, process temperatures other than room temperature and various types or amounts of solutions. Moreover, stirring instead of sonication could be employed alternatively. Another subject of interest would be to investigate the growth mechanism of the nanorods or nanowires. Significant advances could be made in understanding the growth mechanism by observing these nanostructures under a hot-stage TEM. Furthermore, experiments may be performed to observe the catalytic, gasochromic, electrochromic and photochromic properties of synthesized WO_2 nanostructures as well as WO_2/CNT hybrid materials and to determine their potential applications.

Finally, W-Mn matrix composites reinforced with VC were synthesized via mechanical alloying followed by conventional consolidation and sintering techniques. Opportunities exist for further investigation of the W-Mn matrix composites with a Mn amount less than 3 wt.%. Attempts could be made to improve the sinter densities of low Mn (1 wt.%) composites by increasing the mechanical alloying amount, prolonging the sintering duration or slightly increasing the Mn amount. Moreover, advanced consolidation methods like HIP or SPS could be also employed to enhance the properties of the composites. Another possibility would be to use a variety of different reinforcing agents. Should it become possible to improve the relative densities of low Mn composites without hampering their mechanical properties, a new series of experiments would become possible to test their availability for ballistic applications.

In summary; beside the fact that this dissertation work includes comprehensive and detailed information on the production of different tungsten borides (W_2B, WB and W_2B_5) and their mixtures via mechanical alloying, tungsten oxide (WO_2) nanostructures with CNT hybrid materials via a water assisted method and W-Mn matrix composites via mechanical alloying and conventional sintering, from the scientific way of thinking, it is more appropriate to view it as only the beginning of the studies on these three W-based systems. Many new areas can yet be explored, and some points from this work further clarified.

REFERENCES

Acchar, W., Zollfrank, C. and Greil, P. (2004). Microstructure and mechanical properties of WC-Co reinforced with NbC, *Materials Research,* **7,** 445-450.

Aoki, T., Matsushita, T., Suzuki, A., Tanabe, K. and Okuda, M. (2006). Write-once optical recording using WO_2 films prepared by pulsed laser deposition, *Thin Solid Films,* **509,** 107-112.

Arsdale, G.V. (1953). Hydrometallurgy of Base Metals, The Maple Press Com., Inc., New York, USA.

Avettand-Fenoel, M.N., Taillard, R., Dhers, J. and Foct, J. (2003). Effect of ball milling parameters on the microstructure of W-Y powders and sintered samples, *International Journal of Refractory Metals and Hard Materials,* **21,** 205-213.

Baek, Y., Song, Y. and Yong, K. (2006). A novel heteronanostructure system: hierarchical W nanothorn arrays on WO_3 nanowhiskers *Advanced Materials,* **18,** 3105.

Balazsi, C., Sedlackova, K., Llobet, E. and Ionescu, R. (2009). Novel hexagonal WO_3 nanopowder with metal decorated carbon nanotubes as NO_2 gas sensor, *Sensors and Actuators B,* **133,** 151-155.

Balazsi, C., Wang, L., Zayim, E. O., Szilagyi, I. M., Sedlackova, K., Pfeifer, J., Toth, A. L.,and Gouma, P. I. (2008). Nanosize hexagonal tungsten oxide for gas sensing applications *Journal of European Ceramic Society,* **28,** 913-917.

Barsoum, M.W. (2003). Fundamentals of Ceramics, IOP Publishing, Philadelphia, USA.

Bassetti, A., Bonetti, E., Pasquini, L., Montone, A., Grbovic, J. and Antisari, M.V. (2005). Hydrogen desorption from ball milled MgH_2 catalyzed with Fe, *The European Physical Journal,* **43,** 19-27.

Ben-Dora, L. and Shimony, Y. (1974). Crystal structure, magnetic susceptibility and electrical conductivity of pure and NiO-doped MoO_2 and WO_2, *Materials Research Bulletin,* **9,** 837-844.

Benjamin, J.S. (1992). Fundamentals of mechanical alloying. *Materials Science Forum,* **88-90,** 1-18.

Berger, O., Fisher, W.J. and Melev. V. (2004). Tungsten-oxide thin films as novel materials with high sensitivity and selectivity to NO_2, O_3 and H_2S. Part I: Preparation and microstructural characterization of the tungsten-oxide thin films, *Journal of Materials Science: Materials in Electronics,* **15,** 463-482.

Bilgi, E. (2007). Production of titanium diboride, *MSc Thesis*, Middle East Technical University, Ankara, Turkey.

Bose, A., Coque, H.R.A. and Langford, J.Jr. (1992). Development and properties of new tungsten-based composites for penetrators, *International Journal of Powder Metallurgy,* **28,** 383-394.

Bose, A., Yang, S.C. and German, R.M. (1991). Development of a new W-Ni-Mn heavy alloy, *Advances in Powder Metallurgy*, **6,** 425-439.

Boulova, M., Gaskov, A. and Lucazeau, G. (2001). Tungsten oxide reactivity versus CH_4, CO and NO_2 molecules studied by Raman spectroscopy, *Sensors and Actuators B,* **81,** 99-106.

Cai, K.F. and Nan, C.W. (2000). The influence of W_2B_5 addition on microstructure and thermoelectric properties of B_4C ceramic, *Ceramics International,* **26,** 523-527.

Capek, I. (2009). Dispersions, novel nanomaterial sensors and nanoconjugates based on carbon nanotubes, *Advances in Colloid and Interface Science,* **150**, 63-89.

Chambers, A., Park, C., Baker, R.T.K. and Rodriguez, N.M. (1998). Hydrogen storage in graphite nanofibers, *Journal of Physical Chemistry B*, **102**, 4253-4256.

Chan, T.Y. and Lin, S.T. (1998). Interfacial reaction-controlled reprecipitation of W atoms in liquid matrix phase during the sintering of W-8% Mo-7% Ni-3% Fe, *Metallurgical and Materials Transactions A,* **29,** 2885-2892.

Chattopadhyay, K. (2003). Microstructural characterization of sintered W-Ni-Cu alloys, *MSc Thesis,* Indian Institute of Technology, Delhi, India.

Chawla, N. and Shen, Y.L. (2001). Mechanical behavior of particle reinforced metal matrix composites, *Advanced Engineering Materials,* **3,** 357-370.

Chen, C.H. (2006). Self-synthesis and characterization of one-dimensional tungsten carbide and tungsten oxide nanowires, *PhD Thesis,* National Cheng Kung University, Taiwan, China.

Chen, C. L. and Mori, H. (2009). In situ TEM observation of the growth and decomposition of monoclinic $W_{18}O_{49}$ nanowires, *Nanotechnology*, **20,** 285604.

Chen, Y., Wu, Y.C., Yu, F.W. and Chen, J.L. (2008). Microstructure and mechanical properties of tungsten composites co-strengthened by dispersed TiC and La_2O_3 particles, *International Journal of Refractory Metals and Hard Materials,* **26**, 525-529.

Chen, Z., Zhou, M. and Zuo, T. (2000). Morphological evolution of second-phase particles during thermomechanical processing of W-La_2O_3 alloy, *Scripta Materialia,* **43,** 291-297.

Choi, H. G., Jung, Y. H. and Kim, D. K. (2005). Solvothermal synthesis of tungsten oxide nanorod/nanowire/nanosheet, *Journal of American Ceramic Society*, **88**, 1684-1686.

Choi, K., Hwang, N.R. and Kim, D.Y. (2000). Effect of VC addition on microstructural evolution of WC-Co alloy: mechanism of grain growth inhibition, *Powder Metallurgy*, **43,** 168-172.

Chretien, A. and Helgorsky, J. (1961). Borides of molybdenum and tungsten, MoB and WB; New compounds, *Comptes Rendus (Paris)*, **252,** 742-744.

Chung, D.D.L. (2001). Materials for thermal conduction, *Applied Thermal Engineering*, **21,** 1593-1605.

Chujo, Y. (2007). Organic-inorganic nano-hybrid materials, *The Micrometrics*, **50**, 11-15.

Clyne, T.W. (2001). Metal Matrix Composites: Matrices and Processing, in *Encyclopedia of Materials: Science and Technology*, Ed. Mortensen, A., Elsevier, The Netherlands.

Colin, S.B., Caer, G.L., Barraud, E. and Humbert, O. (2004). Mechanically activated synthesis of ultrafine rods of HfB_2 and milling induced phase transformation of monocrystalline anatase particles, *Journal of Materials Science*, **39,** 5081-5089.

Corti, C.W. (1986). The role of the platinum metals in the activated sintering of refractory metals, *Platinum Metals Reviews*, **30,** 184-195.

Coşkun, S. (2006)**.** Development and characterizatıon investigations of mechanically alloyed W-SiC and W-SiC-Y_2O_3 composites, *MSc Thesis*, Istanbul Technical University, Istanbul, Turkey.

Coşkun, S. and Öveçoğlu, M.L. (2011). Effects of Y_2O_3 additions on mechanically alloyed and sintered W-4wt.% SiC composites, *International Journal of Refractory Metals and Hard Materials*, **29,** 651-655.

Coşkun, S., Genç, A. and Öveçoğlu, M.L. (2009). Development and characterization investigations of mechanically alloyed W-Ni/TiC composites, The 138th TMS Annual Meeting, San Francisco, California, USA, February 15-19.

Coşkun, S., Meydanoglu, O., Tatar, D., Ozbek, T. and Corduk, E. (2004). Building a boot using polymeric-composite materials, *Graduation Project*, Istanbul Technical University, Istanbul, Turkey.

Coşkun, S., Öveçoğlu, M.L., Özkal, B. and Tanoğlu, M (2009). Characterization investigations during mechanical alloying and sintering of W-20vol% SiC composites, *Journal of Alloys and Compounds*, **492,** 576-584.

Cox, P.A. (1992)**.** Transition Metal Oxides: An Introduction to Their Electronic Structure and Properties, Clarendon Press, Oxford, United Kingdom.

Davico, G.E., Schwartz, R.L., Ramond, T.M. and Lineberger, W.C. (1999). An experimental study of the low-lying electronic states of WO_2, *Journal of Physical Chemistry A*, **103,** 6167-6172.

Davis, J.J., Coleman, K.S., Azamian, B.R., Bagshaw, C.B. and Green, M.L.H. (2003). Chemical and biochemical sensing with modified single walled carbon nanotubes, *Chemistry - A European Journal,* **9,** 3732-3739.

Dillon, A.C., Jones, K.M., Bekkedahl, T.A., Kiang, C.H., Bethune, D.S. and Heben, M.J. (1997). Storage of hydrogen in single-walled carbon nanotubes, *Nature,* **386,** 377-379.

Donachie, M.J. and Donachie, S.J. (2002). Superalloys: A Technical Guide, ASM International, Ohio, USA.

Dore, F., Martin, C.L. and Allibert, C.H. (2004). Apparent viscosity of W–Cu powder compacts during sintering, *Materials Science and Engineering A,* **383,** 390-398.

DPT: 2608 - ÖİK: 619. (2001). *Sekizinci Beş Yıllık Kalkinma Planı, Madencilik Özel İhtisas Komisyonu Raporu*, Devlet Planlama Teşkilatı (DPT), 1-179, Ankara.

DPT: 2629 - ÖİK: 640. (2001). *Sekizinci Beş Yıllık Kalkinma Planı, Madencilik Özel İhtisas Komisyonu Raporu*, Devlet Planlama Teşkilatı (DPT), 18-28, Ankara.

Dresselhaus, M.S., Dresselhaus, G. and Ekland, P.C. (1996). Science of Fullerenes and Carbon Nanotubes, Academic Press, San Diego, USA.

Duman, İ. (2011). Personal communication.

Duschanek, H. and Rogl, P. (1995). Critical assessment and thermodynamic calculation of the binary system boron-tungsten (B-W*), Journal of Phase Equilibria,* **16**, 150-161.

Dyke, C.A. and Tour, J.M. (2004). Overcoming the insolubility of carbon nanotubes through high degrees of sidewall functionalization, *Chemistry - A European Journal,* **10,** 813-817.

Eder, D. (2010). Carbon nanotube-inorganic hybrids, *Chemical Reviews,* **110,** 1348-1385.

Eder, D. and Windle, A. (2008). Carbon–inorganic hybrid materials: the carbon-nanotube/TiO_2 interface, *Advanced Materials,* **20,** 1787-1793.

El-Eskandarany, M.S., Mahday, A.A., Ahmed, H.A. and Amer, A.H. (2000). Synthesis and characterizations of ball-milled nanocrystalline WC and nanocomposite WC–Co powders and subsequent consolidations, *Journal of Alloys and Compounds,* **312,** 315-325.

Ellis, J.L. and Goetzel, C.G. (1990). Cermets, in *Metals Handbook vol.2,* ASM International, Ohio, USA.

Fecht, H.J. (2002). Nanostructured Materials and Composites Prepared by Solid State Processing, in *Nanostructured Materials: Processing, Properties and Potential Applications*, Ed. Koch, C.C., Noyes Publications, New York, USA.

Fukunga, A., Chu, S.Y. and McHenry, M.E. (1998). Synthesis, structure, and superconducting properties of tantalum carbide nanorods and nanoparticles, *Journal of Materials Research,* **13,** 2465-2471.

Genç, A., Coşkun, S. and Öveçoğlu, M.L. (2010). Fabrication and properties of mechanically alloyed and Ni activated sintered W matrix composites reinforced with Y_2O_3 and TiB_2 particles, *Materials Characterization,* **61,** 740-748.

Genç, A., Coşkun, S. and Öveçoğlu, M.L. (2010). Decarburization of TiC in Ni activated sintered W-xTiC (x = 0, 5, 10, 15 wt%) composites and the effects of heat treatment on the microstructural and physical properties, *International Journal of Refractory Metals and Hard Materials,* **28,** 451-458.

Genç, A., Coşkun, S. and Öveçoğlu, M.L. (2010). Microstructural characterizations of Ni activated sintered W–2wt% TiC composites produced via mechanical alloying, *Journal of Alloys and Compounds,* **497,** 80-89.

German, R.M. and Munir, Z.A. (1982). Activated sintering of refractory metals by transition metal additions, *Reviews on Powder Metallurgy and Physical Ceramics,* **2,** 9-43.

German, R.M. and Munir, Z.A. (1976). Enhanced low-temperature sintering of tungsten, *Metallurgical Transactions A,* **7,** 1873-1877.

German, R.M., Suri, P. and Park, S.J. (2009). Review: liquid phase sintering, *Journal Material Science,* **44,** 1-39.

Goff, A. (2003). Modeling and synthesis of a piezoelectric ceramic-reinforced metal matrix composites. *MS Thesis,* Virginia Polytechnic Institute and State University, Blacksburg, VA, USA.

Gu, Z. J., Zhai, T. Y., Gao, B. F., Sheng, X. H., Wang, Y. B., Fu, H. B., Ma, Y. and Yao, J. N. (2006). Controllable assembly of WO_3 nanorods/nanowires into hierarchical nanostructures, *Journal of Physical Chemistry B,* **110,** 23829-23836.

Gu, G., Zheng, B., Han, W.Q., Roth, S. and Liu, J. (2002). Tungsten oxide nanowires on tungsten substrates. *Nano Letters,* **2,** 849- 851.

Gorbunov, E.A. and Bryksin-Lyamin, M.P. (1971). Refractory Borides as the main constituents of hard-facing powder mixtures, *Poroshkovaya Metallurgiya,* **4**, 91-97.

Gostishchev, V.V., Boiko, V.F. and Pinegina, N.D. (2009). Magnesiothermal synthesis of W–WB powders in ionic melts, *Theoretical Foundations of Chemical Engineering,* **43,** 468-472.

Ha, J.H., Muralidharan, P. and Kim, D.K. (2009). Hydrothermal synthesis and characterization of self-assembled h-WO_3 nanowires/nanorods using EDTA salts, *Journal of Alloys Compounds,* **475,** 446-451.

Hab, A.I. (2007). High-temperature electrochemical synthesis of coatings of carbides, borides, and silicides of metals of the IV – VI B groups from ionic melts, *Materials Science,* **43,** 383-397.

Habashi, F. (1970). Principles of Extractive Metallurgy Volume 2: Hydrometallurgy, Gordon and Breach Science Publishers Ltd., New York, USA.

Hardy, G.F. and Hulm, J.K. (1954). The superconductivity of some transition metal compounds, *Physical Review*, **93,** 1004-1016.

Hashishin, T. and Tamaki, J. (2008). Conductivity-type sensor based on CNT-WO_3 composite for NO_2 detection, *Journal of Nanomaterials,* **2008,** 352854.

Hata, K., Futaba, D.N., Mizuno, K., Namai, T., Yumura, M. and Iijima, S. (2004). Water-assisted highly efficient synthesis of impurity-free single-walled carbon nanotubes, *Science,* **306,** 1362-1364.

Hayden, H.W. and Brophy, J.H. (1963). The activated sintering of tungsten with group VIII elements, *Journal of Electrochemical Society,* **110,** 805-10.

He, Y. and Zhao, Y. (2008). Near-infrared laser-induced photothermal coloration in $WO_3 \cdot H_2O$ nanoflakes, *Journal of Physical Chemistry C,* **112,** 61-68.

Hirsh, A. (2002). Functionalization of single-walled carbon nanotubes, *Angewandte Chemie International Edition,* **41,** 1853-1859.

Hirsh, A. and Vostrowsky, O. (2005). Functionalization of carbon nanotubes, *Topics in Current Chemistry,* **245,** 193-237.

Hong, M.H., Noh, J.W., Baek, W.H., Kim, E.P., Song, H.S. and Lee, S. (1997)**.** A study on the improvement of the sintered density of W-Ni-Mn heavy alloy, *Metallurgical and Materials Transactions B,* **28,** 835-839.

Huirache-Acuna, R., Paraguay-Delgado, F., Albiter, M. A., Lara-Romero, J. and Martinez-Sanchez, R. (2009). Synthesis and characterization of WO_3 nanostructures prepared by an aged-hydrothermal method, *Materials Characterization,* **60,** 932-937.

Hwang, Y. and Lee, J.K. (2002). Preparation of TiB_2 powders by mechanical alloying, *Materials Letters,* **54,** 1-7.

Ibrahim, A., Abdallah, M., Mostafa, S.F. and Hegazy, A.A. (2009). An experimental investigation on the W–Cu composites, *Materials and Design,* **30**, 1398-1403.

Iijima, S. (1991). Helical microtubules of graphitic carbon, *Nature,* **354,** 56-58.

Iizumi, K., Sekiya, C., Okada, S., Kudou, K. and Shishido, T. (2006). Mechanochemically assisted preparation of NbB_2 powder, *Journal of European Ceramic Society,* **26**, 635-638.

Iller, R.K. (1979). The Chemistry of Silica, Wiley, New York, USA.

Ishijima, Y., Kurishita, H., Arakawa, H., Hasegawa, M., Hiraoka, Y., Takida, T. and Takabe, K. (2005). Microstructure and bend ductility of W-0.3mass%TiC alloys fabricated by advanced powder-metallurgical processing, *Materials Transactions,* **46,** 568-574.

Itoh, Y. and Ishiwata, Y. (1996). Strength properties of yttrium-oxide-dispersed tungsten alloy, *JSME International Journal Series A-Mechanics and Material*, **39,** 429-434.

Itoh, H., Matsudaıra, T., Naka, S., Hamamoto, H. and Obayashı, M. (1987). Formation process of tungsten borides by solid state reaction between tungsten and amorphous boron, *Journal of Materials Science,* **22,** 2811-2815.

Jiang, N. and Spence, J.C.H. (2004). Electron energy-loss spectroscopy of the O K edge of NbO_2, MoO_2, and WO_2, *Physical Review B: Condensed Matter,* **70,** 245117-245123.

Johnson, J.L. and German, R.M. (1994). Chemically activated liquid-phase sintering of tungsten-copper, *International Journal of Powder Metallurgy,* **30,** 91-102.

Jones, F.H., Egdell, R.G., Brown, A. and Wondre, F.R. (1997). Surface structure and spectroscopy of WO_2, *Surface Science,* **374,** 80-94.

Kang, S.J.L. (2005). Sintering: Densification, Grain Growth, and Microstructure, Elsevier, Oxford, United Kingdom.

Karasev, A.I. (1972). Manufacture of powders of technical titanium, zirconium, chromium and tungsten borides by the boron carbide method, *Proshkovaya Metallurgiya,***10,** 1-5.

Katrib, A., Hemminga, F., Wehrera, P., Hilairea, L. and Mairea, G. (1995). The multi-surface structure and catalytic properties of partially reduced WO_3, WO_2 and WC + O_2 or W + O_2 as characterized by XPS, *Journal of Electron Spectroscopy and Related Phenomena,* **76,** 195-200.

Kayhan, M., Dzivenko, D., Riedel, R., Hildebrandt, E., Alff, L. and Albert, B. (2011). Hardness and superconductivity of transition metal borides, The 17th International Symposium on Boron, Borides and Related Materials, İstanbul, Türkiye, September 11-17.

Kemp, P.B. and German, R.M. (1991). Grain-growth in liquid-phase-sintered W-Mo-Ni-Fe alloys, *Journal of Less Common Metals,* **175,** 353-368.

Khor, K.A., Yu, L.G. and Sundararajan, G. (2005). Formation of hard tungsten boride layer by spark plasma sintering boriding, *Thin Solid Films,* **478,** 232-237.

Kickelbick, G. (2007). Hybrid Materials: Synthesis, Characterization and Applications, Wiley-VCH Verlag GmbH&Co. KGaA, Weinheim, Germany.

Kida, T., Nishiyama, A., Yuasa, M., Shimanoe, K. and Yamazoe, N. (2009). Highly sensitive NO_2 sensors using lamellar-structured WO_3 particles prepared by an acidification method, *Sensors and Actuators B,* **135,** 568-574.

Kim, D.K., Lee, S. and Baek, W.H. (1998). Microstructural study of adiabatic shear bands formed by high-speed impact in a tungsten heavy alloy penetrator, *Materials Science and Engineering A,* **249,** 197-205.

Kim, J.C., Ryu, S.S., Kim, Y.D. and Moon, I.H. (1998). Densification behavior of mechanically alloyed W-Cu composite powders by the double rearrangement process, *Scripta Materialia,* **39,** 669-676.

Kim, J.W., Shim, J.H., Ahn, J.P., Cho, Y.W., Kim, J.H. and Oh, K.H. (2008). Mechanochemical synthesis and characterization of TiB_2 and VB_2 nanopowders *Materials Letters,* **62,** 2461-2464.

Kim, Y., Hong, M.H., Lee, S.H., Kim, E.P., Lee, S. and Noh, J.W. (2006). The effect of yttrium oxide on the sintering behavior and hardness of tungsten, *Metals and Materials International,* **12,** 245-248.

Kis-Varga, M. and Beke, D.L. (1995). Phase transitions in Cu-Sb systems induced by ball milling, *Materials Science Forum (Switzerland),* **225**, 465-470.

Koltypin, Y., Nikitenko, S. I. and Gedanken, A. (2002). The sonochemical preparation of tungsten oxide nanoparticles, *Journal of Materials Chemistry,* **12,** 1107-1110.

Korneva, G. (2008). Functionalizing of carbon nanotubes, *PhD Thesis,* Drexel University, Philadelphia, USA.

Kroto, H.W., Heath, J.R., O`Brien, S.C., Curl, R.F. and Smalley R.E. (1985). C60: buckminsterfullerene, *Nature,* **318,** 162-163.

Kudaka, K., Iizumi, K., Sasaki, T. and Okada, S. (2001). Mechanochemical synthesis of MoB_2 and Mo_2B_5, *Journal of Alloys and Compounds,* **315,** 104-107.

Kurishita, H., Kobayashi, S., Nakai, K., Ogawa, T., Hasegawa, A., Abe, K., Arakawa, K., Matsuo, S., Takida, T., Takabe, K., Kawai, M. and Yoshida, N. (2008). Development of ultra-fine grained W–(0.25–0.8) wt % TiC and superior resistance to neutron and 3 MeV He-ion irradiations, *Journal of Nuclear Materials,* **377,** 34-40.

Kurishita, H., Matsuso, S., Arakawa, H., Hirai, T., Linke, J., Kawai, M. and Yoshida, N. (2009). Development of nanostructured W and Mo materials, *Advanced Materials Research,* **59,** 18-30.

Kushkhov, K.B., Malyshev, V.V., Tishchenko, A.A. and Shapoval, V.I. (1993). Electrochemical synthesis of tungsten and molybdenum borides in a dispersed condition, *Poroshkovaya Metallurgiya,* **1**, 8-11.

Kuz'ma, Y.B., Serebryakova, T.I. and Plakhina, A.M. (1967). The Polymorphic transformation of tungsten borides - a new phase in the W-B system, *Journal of Inorganic Chemistry,* **12,** 288-289.

Lassner, E. and Schubert, W.D. (1999). Tungsten: Properties, Chemistry, Technology of the Element, Alloys and Chemical Compounds, Kluwer Academic, New York, USA.

Lee, H.R., Kim, D.J., Hwang, N.M. and Kim, D.Y. (2003). Role of vanadium carbide additive during sintering of WC-Co: Mechanism of grain growth inhibition, *Journal of American Ceramic Society,* **86,**152-154.

Lei, Z., Zeda, M. and Chun, O.W. (2011). Fabrication and characterization of tailored TiO_2 and WO_3/MWCNT composites for methylene blue decomposition, *Chinese Journal of Catalysis,* **32,** 926-932.

Li, C. and German, R.M. (1983). The properties of tungsten processed by chemically activated sintering, *Metallurgical and Materials Transactions A,* **14,** 2031-2041.

Li, Y., Kim, W., Zhang, Y., Rolandi, M., Wang, D. and Dai, H. (2001). Growth of single-walled carbon nanotubes from discrete catalytic nanoparticles of various sizes, *Journal of Physical Chemistry B,* **105,** 11424-11431.

Lillard, R.S., Kanner, G.S. and Butt, D.P. (1998). The nature of oxides on tungsten in acidic and alkaline solutions, *Journal of Electrochemical Society,* **145**, 2718-2725.

Lin, C.G., Kny, E., Yuan, G.S. and Djuricic, B. (2004). Microstructure and properties of ultrafine WC-0.6VC-10Co hardmetals densified by pressure-assisted critical liquid phase sintering, *Journal of Alloys and Compounds,* **383,** 98-102.

Lin, T., Bajpai, V., Ji, T. and Dai, L. (2003)**.** Chemistry of carbon nanotubes, *Australian Journal of Chemistry,* **56,** 635-651.

Liu, J., Zhang, Z., Zhao, Y., Su, X., Liu, S. and Wang, E. (2005). Tuning the field-emission properties of tungsten oxide nanorods, *Small,* **1,** 310-313.

Liu, Z.J, Yuan, Z.Y., Zhao, W., Peng, L.M. and Xu, Z., (2001). Co/carbon-nanotube monometallic system: the effects of oxidation by nitric acid, *Physical Chemistry Chemical Physics,* **3,** 2518-2522.

Luo, J., Gupta, V.K., Yoon, D.H. and Meyer, H.M. (2005). Segregation-induced grain boundary premelting in nickel-doped tungsten, *Applied Physics Letters,* **87,** 231902-231904.

Luo, J., Wang, H. and Chiang, Y.M. (1999). Origin of solid-state activated sintering in Bi_2O_3-doped ZnO, *Journal of American Ceramic Society,* **82,** 916-920.

Luyckx, S., Osborne, C., Cornish, L.A. and Whitefield, D. (1996). Fine grained WC-VC-Co hardmetal, *Powder Metallurgy,* **39,** 210-212.

Lv, Y., Wen, G. and Lei, T.Q. (2006). Friction and wear behavior of C-based composites in situ reinforced with W_2B_5, *Journal of the European Ceramic Society,* **26**, 3477-3486.

Lv, Y., Wen, G., Song, L. and Lei, T.Q. (2007). Wear performance of C-W_2B_5 composite sliding against bearing steel, *Wear,* **262,** 592-599.

Ma, Y.R., Tsai C.C., Lee, S.F., Cheng, K.W., Liou, Y., and Yao, Y.D. (2006). Magnetic properties of large-area one-dimensional WO_2 and MoO_2 nanorods, *Journal of Magnetism and Magnetic Materials,* **304,** e13-e15.

Mabuchi, M., Okamoto, K., Saito, N., Asahina, T. and Igarashi, T. (1997). Deformation behavior and strengthening mechanisms at intermediate temperatures in W-La_2O_3, *Materials Science & Engineering A,* **237,** 241-249.

Mackay, A. L. and Terrones, H. (1991). Diamond from graphite, *Nature,* **352**, 762-762.

Malyshev, V.V. (2002). Theoretical foundations and implementation of the high-temperature electrosynthesis of chromium, molybdenum, and tungsten silicides and borides in ionic melts, *Theoretical Foundations of Chemical Engineering,* **36,** 67-79.

Malyshev, V.V., Kushkhov, H.B. and Shaoval, V.I. (2002). High-temperature electrochemical synthesis of carbides, silicides and borides of VI-group metals in ionic melts, *Journal of Applied Electrochemistry,* **32,** 573-579.

Mamalis, A.G., Vogtlaender, L.O.G. and Markopoulos, A. (2004). Nanotechnology and nanostructured materials: trends in carbon nanotubes, *Precision Engineering,* **28,** 16-30.

Maskara, A. and Smith, D.M. (1997). Agglomeration during the drying of fine silica powders, part II: the role of particle solubility, *Journal of American Ceramic Society,* **80,** 1715-1722.

Matkovich, V.I., Samsonov, G.V., Hagenmuller, P. and Lundstrom, T. (1977). Boron and Refractory Borides, Springer-Verlag, Berlin, Germany.

Matsudaira, T., Itoh, H., Naka, S., Hamamoto, H. and Obayashi, M. (1987). Synthesis and reaction sintering of WB, *Yogyo-Kyokai-Shi,* **95,** 248-252.

Miserez, A., Müller, R., Rossoll, A., Weber, L. and Mortensen, A. (2004). Particle reinforced metals of high ceramic content, *Materials Science and Engineering A,* **387-389**, 822-831.

Mouzon, J. and Oden, M. (2007). Alternative method to precipitation techniques for synthesizing yttrium oxide nanopowder, *Powder Technology,* **177,** 77-82.

Mwakikunga, B.W., Forbes, A., Sideras-Haddad, E. and Arendse, C. (2008). Optimization, yield studies and morphology of WO_3 nano-wires synthesized by laser pyrolysis in C_2H_2 and O_2 ambients - validation of a new growth mechanism *Nanoscale Research Letters,* **3,** 372-380.

Nagender, S.V.N. and Rama, P.R. (1991). B-W (Boron-Tungsten), in *Phase diagrams of binary tungsten alloys,* Eds. Nagender, S.V.N. and Rama, P.R., Indian Institute of Metals, Calcutta, India.

Nanba, T., Nishiyama, Y. and Yasui, I.. (1991). Structural study of amorphous WO_3 thin films prepared by the ion exchange method, *Journal of Materials Research,* **6,** 1324-1333.

Niederberger, M., Bartl, M. H. and Stucky, G. D. (2002). Benzyl alcohol and transition metal chlorides as a versatile reaction system for the nonaqueous and low-temperature synthesis of crystalline nano-objects with controlled dimensionality, *Journal of American Chemical Society*, **124,** 13642-13643.

Nikolenko, S.V. and Gostischev, V.V. (1997). Tungsten boride synthesis in burning, The 126th TMS Annual Meeting, Orlando, Florida, USA, February 9-13.

Nimittrakoolchai, O. and Supothina, S. (2008). High-yield precipitation synthesis of tungsten oxide platelet particle and its ethylene gas-sensing characteristic, *Materials Chemistry and Physics*, **112,** 270-274.

Niyogi, S., Hamon, M.A.M, Hu, H., Zhao, B., Bhowmik, P., Sen, R., Itkis, M.E. and Haddon, R.C. (2002). Chemistry of single-walled carbon nanotubes, *Accounts of Chemical Research*, **35,** 1105-1113.

Öveçoglu, M.L. (1987). Development of a dispersion-strengthened Al-Fe-Ce alloy by mechanical alloying and related theoretical modeling of dislocations in composite materials. *PhD Thesis*, Stanford University, Palo Alto, CA, USA.

Öveçoğlu, M.L. (2010). Personal communication.

Öveçoğlu, M.L., Özkal, B. and Suryanarayana, C. (1996). A comparison of the sintering characteristics of ball-milled and attritor-milled W–Ni–Fe heavy alloy, *Journal of Materials Research*, **11,** 1673-1682.

Panichkina, V.V. (1967). Activated sintering of tungsten with small additions of nickel, *Poroshkovaya Metallurgiya (In Russian)*, **2,** 1-5.

Park, J.J. (1993). The high-temperature creep-rupture behavior of W-4Re-0,32HfC, *PhD Thesis*, Arizona State University, Arizona, USA.

Peshev, P., Bliznakov, G. and Leyarovska, L. (1967). On the preparation of some chromium, molybdenum and tungsten borides, *Journal of the Less-Common Metals*, **13,** 241-247.

Pfeifer, J., Badaljan, E., Buxbaum, P.T., Kovacs, T., Geszti, O., Toth, A.L. and Lunk, H.J. (1996). Growth and morphology of $W_{18}0_{49}$ crystals produced by microwave decomposition of ammonium paratungstate, *Journal of Crystal Growth*, **169,** 727-733.

Pierson, H.O. (1996). Handbook of Refractory Carbides and Nitrides Properties, Characteristics, Processing and Applications, Noyes Publications, Park Ridge, NJ, USA.

Pinna, N. and Niederberger, M. (2008). Surfactant-free nonaqueous synthesis of metal oxide nanostructures, *Angewandte Chemie Internatonal Edition*, **47,** 5292-5304.

Polleux, J., Gurlo, A., Barsan, N., Weimar, U., Antonietti, M. and Niederberger, M. (2006). Template free synthesis and assembly of single crystalline tungsten oxide nanowires and their gas sensing properties, *Angewandte Chemie International Edition*, **45,** 261- 265.

Portnoi, K.I., Romashov, V.M., Levinskii, Yu.V. and Romanovich, I.V. (1967). Phase diagram of the system tungsten-boron, *Poroshkovaya Metallurgiya,* **5,** 75-80.

Post, B. and Glaser, F.W. (1952). Borides of some transition metals, *Journal of Chemical Physics,* **20,** 1050-1051.

Predel, B. (1992). Phase Equilibria, Crystallographic and Thermodynamic Data of Binary Alloys: B-Ba ... C-Zr, in *Landolt-Börnstein, New Series IV/5b,* Ed. Madelung, O., Springer-Verlag Berlin, Heidelberg, Germany.

Quinta da Fonseca, J., Cochrane, R.F., Daymond, M.R., Mummery, P.M. and Young, R.M.K. (2001). Microyielding effects in high-volume-fraction MMCs, *Advanced Engineering Materials*, **3**, 913-916.

Quyang, M., Huang, J.L. and Lieber, C.M. (2002). Fundamental electronic properties and applications of single-walled carbon nanotubes, *Accounts of Chemical Research,* **35,** 1018-1025.

Rao, C.N.R. and Nath, M. (2003). Inorganic nanotubes, *Dalton Transactions,* **1,** 1-24.

Rao, C.N.R., Satishkumar, B.C., Govindaraj, A. and Nath, M. (2001). Nanotubes, *Chemical Physics and Physical Chemistry,* **2,** 78-105.

Ricceri, R. and Matteazzi, P. (2003). A study of formation of nanometric W by room temperature mechanosynthesis, *Journal of Alloys and Compounds,* **358,** 71-75.

Ricceri, R. and Matteazzi, P. (2003). Mechanochemical synthesis of elemental boron, *International Journal of Powder Metallurgy,* **39,** 48-52.

Ricceri, R. and Matteazzi, P. (2004). A fast and low-cost room temperature process for TiB_2 formation by mechanosynthesis, *Materials Science and Engineering A,* **379,** 341–346.

Roosta, M., Baharvandi, H. and Abdizade, H. (in press). An experimental investigation on the fabrication of W-Cu composite through hot-press, *International Jornal of Industrial Chemistry.*

Rudy, E., Benesovsky, F. and Toth, L. (1963). The Investigation of the ternary systems of the group V and VI metals with boron and carbon, *Zeitschrift Für Metallkunde,* **54,** 345-353.

Ryu, H.J. and Hong, S.H. (2003). Fabrication and properties of mechanically alloyed oxide-dispersed tungsten heavy alloys, *Materials Science and Engineering A,* **363,** 179-184.

Ryu, H.J., Hong, S.H. and Baek, W.H. (2000). Microstructure and mechanical properties of mechanically alloyed and solid-state sintered tungsten heavy alloys, *Materials Science and Engineering A,* **291,** 91-96.

Ryu, H.J., Hong, S.H. and Baek, W.H. (1997). Milling process of 93W-5.6Ni-1.4Fe tungsten heavy alloys, *Journal of Materials Processing Technology,* **63,** 292-297.

Saito, Y. (2003). Nanotubes and nanowires, *Journal of Nanoscience Nanotechnology,* **3,** 39-50.

Samsonov, G.V. and Yakovlev, V.I. (1967). Activated sintering of tungsten with nickel additions, *Poroshkovaya Metallurgiya (In Russian),* **8,** 10-16.

Samsonov, G.V. and Yakovlev, V.I. (1969). Activation of the sintering of tungsten by the iron-group metals, *Poroshkovaya Metallurgiya (In Russian),* **10,** 32-38.

Sarin, V.K. (1975). Morphological changes occurring during the reduction of WO_3, *Journal of Materials Science,* **10,** 593-598.

Satishkumar, B. C., Govindaraj, A., Nath, M. and Rao, C. N. R. (2000). Synthesis of metal oxide nanorods using carbon nanotubes as templates, *Journal of Materials Chemistry*, **10,** 2115-2119.

Schwartz, M.M. (1984). Composite Materials Handbook, McGraw-Hill, New York, USA

Schwartz, M.M. (1997). Composite Materials-Vol.1., Prentice Hall, Portland, USA.

Seitzer, W.H. (1975). Manufacture of Hydrogen, *United States Patent,* No: 3859373 dated 7.1.1975.

Setoudeh, N. and Welham, N.J. (2006). Formation of zirconium diboride (ZrB_2) by room temperature mechanochemical reaction between ZrO_2, B_2O_3 and Mg, *Journal of Alloys and Compounds*, **420**, 225-228.

Shackelford, J.F. and Alexander, W. (2001). Materials Science and Engineering Handbook 3rd Edition, CRC Press LLC, Florida, USA.

Shah, M.A. (2009). Tungsten trioxide nanoplates prepared without organics at low temperature, *African Physical Review,* **3**, 57-60.

Shankar, N., Yu, M.F., Vanka, S.P. and Glumac, N.G. (2006). Synthesis of tungsten oxide (WO_3) nanorods using carbon nanotubes as templates by hot filament chemical vapor deposition, *Materials Letters*, **60,** 771-774.

Shaposhnikov, V.L., Migas, D.B., Rodin, V.N. and Borisenko, V.E. (2011). Ab initio investigation of structural and electronic properties of tungsten dioxide, *Physica Status Solidi B,* **248,** 1471-1476.

Shi, X. and Luo, J. (2009). Grain boundary wetting and prewetting in Ni-doped Mo, *Applied Physics Letters,* **94,** 251908-251910.

Shingaya, Y. and Nakayama, T. (2008). Epitaxial Growth of WO_x Nanorods on Single-Crystal Tungsten Substrate, *Electronics and Communications in Japan,* **91,** 20-24.

Song, G.M., Wang, Y.J. and Zhou, Y. (2002). The mechanical and thermophysical properties of ZrC/W composites at elevated temperature, *Materials Science and Engineering*. **334,** 223-232.

Song, G.M., Wang, Y.J. and Zhou, Y. (2003). Thermomechanical properties of TiC particle-reinforced tungsten composites for high temperature applications, *International Journal of Refractory Metals & Hard Materials,* **21,** 1-12.

Song, G.M., Zhou, Y. and Wang, Y.J. (2002). The microstructure and elevated temperature strength of tungsten-titanium carbide composite, *Journal of Material Science,* **37,** 3541-3548.

Song, G.M., Zhou, Y. and Wang, Y.J. (2003). Effect of carbide articles on the ablation properties of tungsten composites, *Materials Characterization,* **50,** 293-303.

Song, X. C., Zheng, Y. F., Yang, E. and Wang, Y. (2007). Large-scale hydrothermal synthesis of WO_3 nanowires in the presence of K_2SO_4, *Materials Letters,* **61,** 3904-3908.

Stadler, S., Winarski, R.P., MacLaren, J.M., Ederer, D.L., vanEk, J., Moewes, A., Grush, M.M., Callcott, T.A. and Perera R.C.C. (2000). Electronic structures of the tungsten borides WB, W_2B and W_2B_5, *Journal of Electron Spectroscopy and Related Phenomena,* **110-111,** 75-86.

Stjernstoft, T. (2004). Machining of some difficult-to-cut materials with rotary cutting tools, *PhD Thesis,* K.T.H., Stockholm, Sweden.

Stubicar, M., Tonejc, A. and Stubicar, N. (1995). X–Ray diffraction study of W–B elemental powder mixtures after high–energy ball–milling, *Fizika A,* **4,** 65-72.

Su, C. Y. and Lin, H. C. (2009). Direct route to tungsten oxide nanorod bundles: microstructures and electro-optical properties, *Journal of Physical Chemistry C,* **113,** 4042-4046.

Supothina, S., Seeharaj, P., Yoriya, S. and Sriyudthsak, M. (2007). Synthesis of tungsten oxide nanoparticles by acid precipitation method, *Ceramics International,* **33,** 931-936.

Suryanarayana, C. (2001). Mechanical alloying and milling, *Progress in Materials and Science,* **46,** 1-184.

Suryanarayana, C. and Norton, M.G. (1998). X-Ray Diffraction: A Practical Approach, Plenum Press, New York, USA.

Suryanarayana, C., Ivanov, E. and Boldyrev, V.V. (2001). The science and technology of mechanical alloying, *Materials Science and Engineering A,* **304-306,** 151-158.

Tang, H.G., Ma, X.F., Zhao, W., Yan, X.W., Yan, J.M. and Zhu, C.J. (2004). Crystallization of mechanically alloyed amorphous W–Mg alloy under high pressure, *Solid State Communications,* **129,** 147-150.

Tang, W.M., Zheng, Z.X., Wu, W.C., Lü, J., Liu, J.W. and Wang, J.M. (2006). Structural evolutions of mechanically alloyed and heat treated $Ti_{50}C_{50}$ and $Ti_{33}B_{67}$ powders, *Materials Chemistry and Physics,* **99,** 144-149.

Tasis, D., Tagmatarchis, N., Bianco, A. and Prato, M. (2006). Chemistry of carbon nanotubes, *Chemical Reviews,* **106,** 1105-1136.

Taylor, R.E., Kimbrough, W.D. and Powell, R.W. (1971). Thermophysical properties of tantalum, tungsten, and tantalum-10 wt. % tungsten at high temperatures, *Journal of the Less Common Metals,* **24,** 369-382.

Telle, R., Sigl, L.S., and Takagi, K. (2000). Boride-Based Hard Materials, in *Handbook of Ceramic Hard Materials*, Ed. Riedel, R., Wiley-VCH Verlag GmbH&Co. KGaA, Weinheim, Germany.

Therese, H. A., Li, J., Kolb, U. and Tremel, W. (2005). Facile large scale synthesis of WS_2 nanotubes from WO_3 nanorods prepared by a hydrothermal route, *Solid State Sciences,* **7,** 67-72.

Tjong, S.C. and Ma, Z.Y. (2000). Microstructural and mechanical characteristics of in situ metal matrix composites, *Materials Science and Engineering*, **29,** 49-113.

Toth, I.J. and Lockington, N.A. (1967). The kinetics of metallic activation sintering of tungsten, *Journal of Less Common Metals,* **12,** 353-65.

Upadhaya, A., Tiwari, S.K. and Mishra, P. (2007). Microwave sintering of W-Ni-Fe alloy, *Scripta Materialia,* **56,** 5-8.

Usta, M., Ozbek, I., Ipek, M., Bindal, C. and Ucisik, A.H. (2005). The characterization of borided pure tungsten, *Surface & Coatings Technology,* **194,** 330-334.

Vacek, J. (1959). On influencing the sintering behavior of tungsten, *Planseeberichte fur Pulvermetallurgie,* **7,** 6-17.

Walker, P. and Tarn, W.H. (1991). Handbook of Metal Etchants, CRC Press LLC, Florida, USA.

Wang, J., Lee, P. S. and Ma, J. (2009). Synthesis, growth mechanism and room-temperature blue luminescence emission of uniform WO_3 nanosheets with W as starting material, *Journal of Crystal Growth*, **311,** 316-319.

Wang, S.J., Chen, C.H., Ko, R.M., Kuo, Y.C., Wong, C.H., Wu, C.H., Uang, K.M., Chen, T.M. and Liou, B.W. (2005). Preparation of tungsten oxide nanowires from sputter-deposited WC_x films using an annealing/oxidation process, *Applied Physics Letters,* **86,** 263103.

Welham, N.J. (1999)**.** Formation of TiB_2 from rutile by room temperature ball milling, *Minerals Engineering,* **12,** 1213-1224.

Wen, G., Lv, Y. and Lei, T.Q. (2006). Friction and wear behavior of C-based composites in situ reinforced with W_2B_5, *Journal of the European Ceramic Society,* **26,** 3477-3486.

Wen, G., Lv, Y. and Lei, T.Q. (2006). Reaction-formed W_2B_5/C composites with high performance, *Carbon,* **44,** 1005-1012.

Whitby, R.L.D., Hsu, W.K., Lee, T.H., Boothroyd, C.B., Kroto, H.W. and Walton, D.R.M. (2002). Complex WS_2 nanostructures, *Chemical Physics Letters,* **359**, 68-76.

Wriedt, H.A. (1989). W-O System, *Bulletin of Alloy phase diagrams,* **10,** 368-384.

Xie, S., Li, W., Pan, Z., Chang, B. and Sun, L., 2000. Carbon nanotube arrays, *Materials Science and. Engineering A,* **286,** 11-15.

Xu, Z., Vetelino, J.F., Lec, R. and Parker, D.C. (1990). Electrical properties of tungsten trioxide films, *Journal of Vacuum Science & Technology A,* **8,** 3634-3638.

Venkateswaran, T., Basu, B., Raju, G.B. and Kim, D.Y. (2006). Densification and properties of transition metal borides-based cermets via spark plasma sintering, *Journal of the European Ceramic Society,* **26,** 2431-2440.

Yazıcı, S. (2009). Kendiliğinden ilerleyen yüksek sıcaklık sentezi yöntemi ile tungsten borür tozu üretimi. *M.Sc. Thesis,* Istanbul Technical University, Istanbul, Turkey.

Yoon, E.S., Lee, J.S., Oh, S.T. and Kim, B.K. (2002). Microstructure and sintering behavior of W-Cu nanocomposite powder produced by thermo-chemical process, *International Journal of Refractory Metals and Hard Materials,* **20,** 201-206.

York, A.P.E., Sloan, J. and Green, M.L.H. (1999). Epitaxial growth of WO_{3-x} needles on $(10\bar{1}0)$ and $(01\bar{1}0)$ WC surfaces produced by controlled oxidation with CO_2, *Chemical Communications,* **8,** 269-270.

Zaharee, S.M., Arabi, H., Salehi, M.T. and Tamizifar, M. (2008). Effect of Mn/Ni ratio variation on microstructure of W–Ni–Mn alloy, *Powder Metallurgy,* **51,** 303-309.

Zhang, F.L., Wang, C.Y. and Zhu, M. (2003). Nanostructured WC/Co composite powder prepared by high energy ball milling, *Scripta Materialia,* **49,** 1123-1128.

Zhang, H., Feng, M., Liu, F., Liu, L., Chen, H., Gao, H. and Li J. (2004). Structures and defects of WO_{3-x} nanorods grown by in-situ heating tungsten filament, *Chemical Physics Letters,* **389,** 337-341.

Zhao, W., Song, C. and Pehrsson, P.E. (2002). Water-soluble and optically ph-sensitive single-walled carbon nanotubes from surface modification, *Journal of American Chemical Society,* **124,** 12418-12419.

Zerr, A. and Riedel, R. (2000). Introduction: Novel Ultrahard Materials, in *Handbook of Ceramics vol.1,* Ed. Riedel, R., Wiley-VCH Verlag GmbH&Co. KGaA, Weinheim, Germany.

Url-1 *<http://www.itia.info/Default.asp?page=34>, accessed at 18.08.2011*

Url-2 *<http://www.itia.info/Default.asp?page=53>, accessed at 18.08.2011*

Url-3 *<http://www.itia.info/Default.asp?Page=59>, accessed at 18.08.2011*

Url-4 *<http://www.etimaden.gov.tr/en/0_sayfa_ortakSayfa.asp?hangisayfa =4_sayfa_a_1 >, accessed at 09.09.2011*

Url-5 *< http://www.alfa.com/en/gp140w.pgm>, accessed at 09.09.2011*

Url-6 *< http://www.retimetal.com/product-50-Tungsten-alloy.html>, accessed at 11.10.2011*

CURRICULUM VITAE

Name Surname: Selim COŞKUN

Place and Date of Birth: Istanbul, 20.05.1980

Address: Serencebey Yokuşu, Hasırcıveli Sokak No:12 Anadolu Apartmanı Daire.8, 34353, Beşiktaş, İstanbul.

E-Mail: selim_coskun@yahoo.com

B.Sc.: Istanbul Technical University, Department of Metallurgical and Materials Engineering, 2004.

M.Sc.: Istanbul Technical University, Department of Materials Science and Engineering, 2006.

Professional Experience and Rewards:

- September 2009 - June 2010: *Visiting Scientist*, Department of Materials Science and Metallurgy, The University of Cambridge, Cambridge.
- May 2007 - Present: *Research Assistant*, Department of Metallurgical and Materials Engineering, Istanbul Technical University.
- 2214 – TUBITAK – International Research Scholarship (December 2009 - June 2010)
- 2211 – TUBITAK - Ph.D. Scholarship (2007 - 2011)
- 2210 – TUBITAK - M.Sc. Scholarship (2004 - 2006)
- ITU, Chemical and Metallurgical Engineering Faculty's First Prize (2004)
- ITU, Metallurgical and Materials Engineering Department's First Prize (2004)

List of Publications and Patents:

- **Coşkun. S.,** Öveçoğlu. M.L. (2011). Effects of Y_2O_3 additions on mechanically alloyed and sintered W - 4 wt.% SiC composites, *International Journal of Refractory Metals and Hard Materials,* **29,** 651-655.
- Genç. A., **Coşkun. S.,** Öveçoğlu. M.L. (2010). Decarburization of TiC in Ni activated sintered W - xTiC (x= 0, 5, 10, 15 wt%) composites and the effects of heat treatment on the microstructural and physical properties, *International Journal of Refractory Metals and Hard Materials,* **28,** 451-458.

- Genç. A., **Coşkun. S.,** Öveçoğlu. M.L. (2010). Fabrication and properties of mechanically alloyed and Ni activated sintered W matrix composites reinforced with Y_2O_3 and TiB_2 particles, *Materials Characterization,* **61,** 740-748.
- Genç. A., **Coşkun. S.,** Öveçoğlu. M.L. (2010). Microstructural characterizations of Ni activated sintered W - 2 wt.%TiC composites produced via mechanical alloying, *Journal of Alloys and Compounds,* **497,** 80-89.
- **Coşkun. S.,** Öveçoğlu. M.L., Ozkal. B., Tanoğlu. M. (2010). Characterization Investigations during Mechanical Alloying and Sintering of W - 20 vol.%SiC Composites, *Journal of Alloys and Compounds,* **492,** 576-584.
- Genç. A., **Coşkun. S.,** Öveçoğlu. M.L. (2009). Production of TiC/VC Dispersed W - Ni Nano Composites, International Conference on Nanomaterials and Nano Systems NanoMats2009, Istanbul, Turkey, August 10-13.
- Genç. A., **Coşkun. S.**, Öveçoğlu. M.L. (2009). Development and characterization investigations of mechanically alloyed and sintered W - 2wt%VC - 1wt%Ni composites, The 2009 International Conference on Powder Metallurgy & Particulate Materials, Las Vegas, USA, June 28-July 01.
- Sönmez. T., Ozkaya. H.D., **Coşkun. S.,** Öveçoğlu. M.L. (2009). Development and characterization of yttria partially stabilized zirconia (P-YSZ) via high energy milling, The 2009 International Conference on Powder Metallurgy & Particulate Materials, Las Vegas, USA, June 28-July 01.
- **Coşkun. S.,**Genç. A., Öveçoğlu. M.L. (2009). Development and characterization investigations of mechanically alloyed W-Ni/TiC composites, The 138th TMS Annual Meeting, San Francisco, USA, February 15-19.

PUBLICATIONS/PRESENTATIONS ON THE THESIS

- **Coşkun. S.,** Koziol. K.K. (2011). Water-assisted synthesis of tungsten oxide nanoparticles at room temperature, *Chemical Communications,* submitted.
- **Coşkun.** S., Öveçoğlu. M.L. (2011). Synthesis of W - 3 wt.% Mn - 2 wt.% VC composites by high energy milling, *Metals and Materials International,* submitted.
- **Coşkun.** S.,Genç. A., Öveçoğlu. M.L. (2009). Development and characterization investigations of mechanically alloyed W-Mn-VC composites, The 2009 International Conference on Powder Metallurgy & Particulate Materials, Las Vegas, USA, June 28-July 01.